DAHLGREN DIVISION
NAVAL SURFACE WARFARE CENTER
Dahlgren, Virginia 22448-5100

NSWCDD/TR-97/20

AN IMPROVED SEMIEMPIRICAL METHOD FOR CALCULATING AERODYNAMICS OF MISSILES WITH NONCIRCULAR BODIES

BY FRANK G. MOORE ROY M. MCINVILLE TOM HYMER

WEAPONS SYSTEMS DEPARTMENT

SEPTEMBER 1997

REPORT DOCUMENTATION PAGE

Form Approved
OMB No. 0704-0188

1. AGENCY USE ONLY (Leave blank)	2. REPORT DATE	3. REPORT TYPE AND DATES COVERED
	September 1997	Final

4. TITLE AND SUBTITLE

An Improved Semiempirical Method for Calculating Aerodynamics of Missiles with Noncircular Bodies

5. FUNDING NUMBERS

6. AUTHOR(s)

Frank G. Moore, Roy M. McInville, Tom Hymer

7. PERFORMING ORGANIZATION NAME(S) AND ADDRESS(ES)

Commander
Naval Surface Warfare Center
Dahlgren Division (Code G03)
17320 Dahlgren Road
Dahlgren, VA 22448-5100

8. PERFORMING ORGANIZATION REPORT NUMBER

NSWCDD/TR-97/20

9. SPONSORING/MONITORING AGENCY NAME(S) AND ADDRESS(ES)

10. SPONSORING/MONITORING AGENCY REPORT NUMBER

11. SUPPLEMENTARY NOTES

12a. DISTRIBUTION/AVAILABILITY STATEMENT

Approved for public release; distribution is unlimited.

12b. DISTRIBUTION CODE

13. ABSTRACT (Maximum 200 words)

An improved method has been developed to compute aerodynamics of noncircular cross section shapes. The improved method is based on extending current state-of-the-art methods for computing aerodynamics of noncircular wing-body shapes based on circular wing-body methods.

Specific additions to the state-of-the-art methods presently in use include extensions to a broader class of cross section bodies and to a higher angle of attack (AOA); extensions to allow improved accuracy at low cross-flow Mach number and to allow body cross-section shape to impact the critical cross-flow Reynolds number; and a method to treat wing-body interference factor corrections as a function of body geometry, Mach number, and AOA.

The new methods were applied to a broad class of noncircular body alone and wing-body configurations for which wind tunnel data were available. In general, results for normal force, axial force and center of pressure were quite good over the Mach number and AOA range where data was available. This included Mach numbers as low as 0.3 and as high as 14 and AOAs to 60 degrees.

14. SUBJECT TERMS

aerodynamics, semiempirical method, Aeroprediction Code, Newtonian Impact Theory, freestream Mach number, SHABP, Missile DATCOM

15. NUMBER OF PAGES

140

16. PRICE CODE

17. SECURITY CLASSIFICATION OF REPORTS	18. SECURITY CLASSIFICATION OF THIS PAGE	19. SECURITY CLASSIFICATION OF ABSTRACT	20. LIMITATION OF ABSTRACT
UNCLASSIFIED	UNCLASSIFIED	UNCLASSIFIED	UL

FOREWORD

The latest version of the NSWCDD Aeroprediction Code (AP95) calculates aerodynamics of weapons that have axisymmetric (circular) body cross-sectional shapes over a wide range of flight conditions. While this covers most of the world's weapons, there are occasions where noncircular body cross-sectional shapes are of interest in preliminary design tradeoffs. Two of these include blended weapon and aircraft design for overall aircraft/store drag reduction or weapon range improvement and more efficient utilization of a vertical launcher cell on a ship (this is primarily associated with short range missile applications). As a result of these needs, new technology was developed and integrated into the AP95 for calculating aerodynamics of weapons with noncircular cross-sectional shapes.

The work described in this report was supported through the Office of Naval Research (Mr. Dave Siegel) by the following programs: the Air Launched Weapons Program managed at the Naval Air Warfare Center, China Lake, CA, by Mr. Tom Loftus and Dr. Craig Porter, and the Surface Weapons Systems Technology Program managed at the Naval Surface Warfare Center, Dahlgren Division (NSWCDD) by Mr. Robin Staton and Mr. Gill Graff. Also, some support was provided by the Marine Corps Weaponry Technology Program managed at NSWCDD by Mr. Bob Stiegler. The authors express appreciation for support received in this work.

Approved by:

David Malyevac

DAVID S. MALYEVAC, Deputy Head
Weapons Systems Department

CONTENTS

ILLUSTRATIONS

ILLUSTRATIONS (Continued)

ILLUSTRATIONS (Continued)

ILLUSTRATIONS (Continued)

ILLUSTRATIONS (Continued)

TABLES

1.0 INTRODUCTION

The desire to increase weapon range and maneuverability, to design weapons which are more optimum from an aircraft total drag and radar signature standpoint, or to provide optimum loadout of multiple missiles in a ship's vertical launcher has driven weapons designers to consider nonaxisymmetric body shapes. Some typical shapes are shown in Figure 1. While most missiles in the United States and foreign countries in existence today have axisymmetric body configurations, these conceptual design tradeoffs of various configurations other than axisymmetric require engineering estimates of aerodynamics. Current state-of-the-art methods for predicting aerodynamics of nonaxisymmetric body shapes with engineering accuracy are much more limited than for axisymmetric bodies. This is primarily driven by the fact that to get reasonable accuracy of the aerodynamics requires an accurate description of the body geometry. To describe the geometry of a complex body shape accurately can take days or weeks depending on the requirements of the aerodynamics code being used.

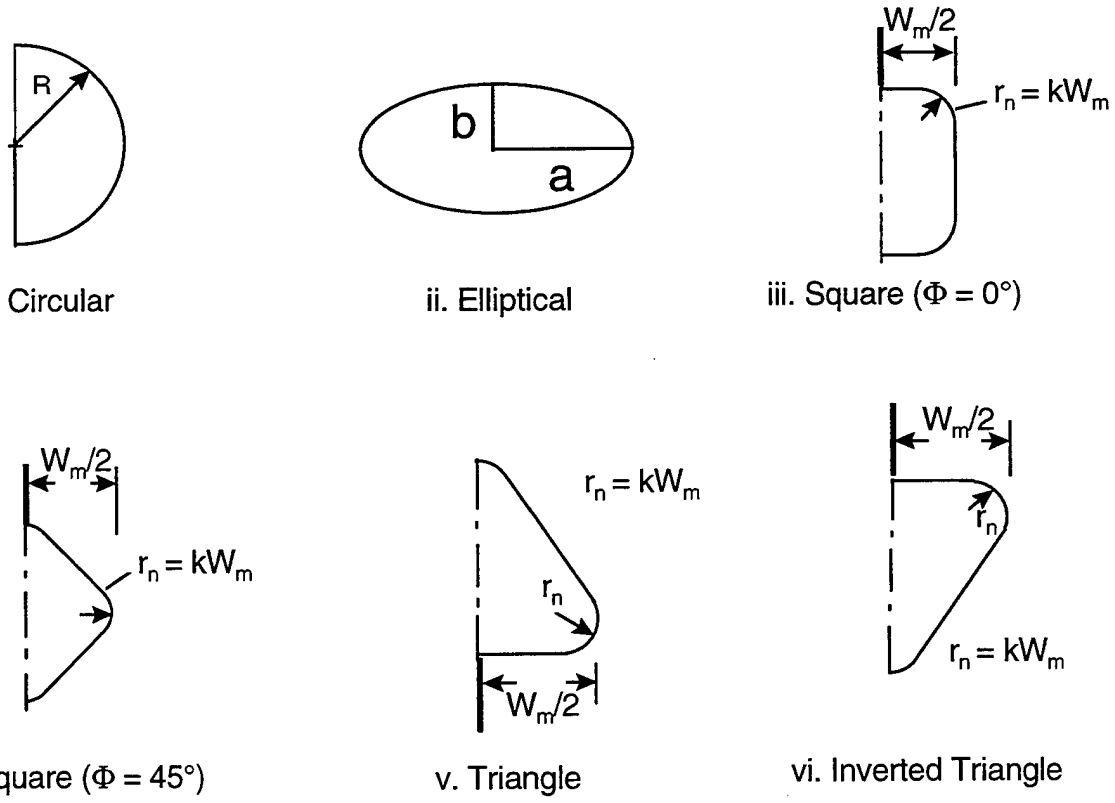

FIGURE 1. BODY CROSS-SECTIONAL SHAPES OF INTEREST

The present approaches to computing aerodynamics fall into two basic classes. The first class requires the description of the body geometry in some detail for aerodynamic computations. Methods that fall into this class may use local slope approaches (tangent-wedge, tangent-cone, Newtonian Impact Theory, etc) to estimate the surface pressure. These techniques basically need a freestream Mach number and the angle between the freestream velocity vector and the tangent to a local point on the body to compute a local pressure coefficient (and other thermodynamic properties if desired). No influence of surrounding elements is felt by the particular body element of interest. A typical computer program in use today that uses this approach is the Supersonic-Hypersonic-Arbitrary Body-Program (SHABP).[1]

Another approach that requires detailed geometry input is the so-called paneling method. Here the configuration is described by a distribution of sources, sinks and doublets so that the body boundary condition of flow tangency is met. The configuration is once again described by panels, but here the flow from one panel can affect another panel, as opposed to the local slope approaches. A state-of-the-art program that uses this approach is the PANAIR code.[2]

A third approach which falls into the class of aerodynamic codes requiring detailed geometry inputs are so-called numerical codes. These codes typically solve the full inviscid[3] set of equations or various versions of the viscous Navier Stokes equations.[4] Geometry must be input even more accurately here due to the requirement of accurate second-order, partial derivatives in the fluid dynamics equations. Manweeks or manmonths can easily be required to describe a complex configuration for these types of codes.

The second class of codes calculating the aerodynamics of a nonaxisymmetric body is based on an equivalent axisymmetric body. The beauty of this approach is the fact that an existing axisymmetric body code can be used to calculate nonaxisymmetric body aerodynamics if the area distribution of the body is known. The area distribution requires a lot less time to define than a detailed configuration geometry. On the other hand, one should anticipate possibly larger errors in predicting the aerodynamics than an approach where the detailed geometry is required. The ease of use, fast turnaround and lower cost may be worth the reduced accuracy however. This type of approach was pioneered by the methods of Whitcomb[5] and Jorgensen.[6-10]

The Missile DATCOM[11] code uses the method of Jorgensen to estimate aerodynamics of elliptic cross-sectional shapes to any angle of attack (AOA) and other cross-sectional shapes at small AOA. However, no such code is available for other than elliptical cross-sectional shapes at high AOA. There are several areas where the Jorgensen approach needs improvement. First, the method was derived on the basis of slender body theory (SBT) for low AOA and modified Newtonian theory (MNT) at higher AOA. The MNT, strictly speaking, is accurate only for higher Mach numbers and therefore needs to be corrected for lower Mach numbers. Secondly, most of the data available for making these empirical corrections to MNT is at low speed and thus additional data or computational fluid dynamics efforts are needed for higher Mach number. Third, the Jorgensen correlation factors based on SBT and MNT work reasonably well in predicting normal forces for elliptical configurations but not so well for triangular and square cross-sectional bodies. Fourth, the Jorgensen approach uses SBT for interference between the wings and bodies with no nonlinear corrections for AOA, Mach number or wing shape. The Missile Datcom[11] improves upon this problem by the use of the equivalent AOA method.[12] This allows the nonlinear corrections of wing-body lift to be included and

extends the AOA boundary to 20-25 deg for interference effects. Finally, no corrections are included in the Jorgensen method for the axial force wave component of drag for the noncircular bodies compared to the circular bodies.

While the Jorgensen method has its shortcomings, it is still the method most compatible with the NSWC aeroprediction code (APC).[13] This is because the APC is currently developed for axisymmetric bodies. The goal of the present work is therefore to modify the work of Jorgensen to improve upon the shortcomings stated previously. If successful, a more robust, more accurate, yet simple code for computing aerodynamics of nonaxisymmetric body missile configurations will be available.

2.0 ANALYSIS

The goal of the present work is to extend the APC[13] to include simple nonaxisymmetric body configurations. As discussed in the introduction, the approach most compatible with the axisymmetric body techniques of Reference 13 is one which computes the aerodynamics of a nonaxisymmetric body on the basis of an equivalent axisymmetric body. The most developed of these approaches is that of Jorgensen.[6-10] As such, it is believed instructive to briefly review the Jorgensen[6-10] method, point out the weak areas discussed in the introduction part of this report, and then address the present improved methodology to overcome these shortcomings.

2.1 REVIEW OF JORGENSEN'S[6-10] METHOD

Jorgensen's method for the static aerodynamics of a body alone are given by

$$C_A = (C_A)_{\alpha=0} \cos^2\alpha \tag{1}$$

$$C_N = \frac{\sin(2\alpha)\cos(\alpha/2)}{A_{ref}} \int_0^{\ell} \left(\frac{C_n}{C_{n_O}}\right)_{SB} \left(\frac{dA}{dx}\right) dx$$

$$+ \frac{2\eta\, C_{d_C} \sin^2\alpha}{A_{ref}} \int_0^{\ell} \left(\frac{C_n}{C_{n_O}}\right)_N r\,dx \tag{2}$$

$$C_M = \frac{\sin(2\alpha)\,\cos(\alpha/2)}{A_{ref}\ell_{ref}} \int_0^{\ell} \left(\frac{C_n}{C_{n_O}}\right)_{SB} \frac{dA}{dx}\,(x_m - x)\,dx$$

$$+ \frac{2\eta\, C_{d_C}\, \sin^2\alpha}{A_{ref}\ell_{ref}} \int_0^{\ell} \left(\frac{C_n}{C_{n_O}}\right)_{N} r(x_m - x)\,dx \qquad (3)$$

$$\frac{x_{CP}}{\ell_{ref}} = -\frac{C_M}{C_N} + \frac{x_m}{\ell_{ref}} \qquad (4)$$

Equations (2) and (3) allow for continually varying cross sections along the body. Equation (1) is an assumed approximation for correlating axial force with AOA. It also requires a calculation of, or that experimental data be available for, axial force coefficient at zero AOA. Equations (2) and (3) both include the factors $(C_n/C_{n_O})_{SB}$ and $(C_n/C_{n_O})_N$. These factors represent the slender body and Newtonian approximations to the local normal force coefficient per unit length of the desired cross-sectional shape (C_n) to the similar coefficient for the equivalent circular cross-sectional shape (C_{n_O}). The radius of the equivalent cross-sectional shape is determined by

$$r_{eq} = \sqrt{\frac{A(x)}{\pi}} \qquad (5)$$

where A(x) represents the area of the nonaxisymmetric body as it varies along the body x-axis. The first terms of both Equations (2) and (3) are the terms due to potential flow and the second terms are those due to the viscous crossflow. Since SBT is only applicable for small AOAs, the coefficient $(C_n/C_{n_O})_{SB}$ can only be used for the first term of Equations (2) and (3). On the other hand, Newtonian Impact Theory is applicable at any AOA and can therefore be used for the second term of Equations (2) and (3). C_{d_C} is the crossflow drag coefficient for the equivalent body of revolution. Finally, both Equations (3) and (4) are defined about some reference point x_m. $(C_n/C_{n_O})_{SB}$ and $(C_n/C_{n_O})_N$ are given in Reference 6 for several ellipses. $(C_n/C_{n_O})_N$ is also given for some squares. Reference 11 gives the SB theory values of $(C_n/C_{n_O})_{SB}$ for several configurations.

To apply the methodology of Equations (1) through (4) to wing-body-tail configurations, Jorgensen[6] suggests replacing the first term of Equations (2) and (3) with that computed by Reference 14. Using this approach, Equations (2) and (3) become

$$C_N = C_{N_L} \frac{\sin 2\alpha}{2\alpha} + \frac{2\eta C_{d_C} \sin^2\alpha}{A_{ref}} \int_0^{\ell} \left(\frac{C_n}{C_{n_O}} \right)_N r \, dx \tag{6}$$

$$C_M = C_{M_L} \frac{\sin 2\alpha}{2\alpha} + \frac{2\eta C_{d_C} \sin^2\alpha}{A_{ref} \ell_{ref}} \int_0^{\ell} \left(\frac{C_n}{C_{n_O}} \right)_N r(x_m - x) dx \tag{7}$$

C_{N_L} and C_{M_L} are the potential normal force and pitching moments computed by linearized and SBT as defined by Reference 14.

Reviewing Equations (1) through (7), it is appropriate to specifically point out the weak points suggested in the introduction. First of all, Equation (1) assumes $(C_A)_{\alpha=0}$ of the equivalent axisymmetric body is the same as that for the noncircular body and that C_A varies as $\cos^2\alpha$ with AOA. These assumptions need further investigation. Secondly, $(C_n/C_{n_O})_N$ is accurate primarily at high Mach number. A correction for lower crossflow Mach numbers is probably required ($M_N < 2.0$) for accurate prediction of static aerodynamics at all AOAs and M_∞'s. Thirdly, additional analytical equations need to be derived for $(C_n/C_{n_O})_N$ for other than elliptical cross-sectional shapes. This is required in order to expand the approach of Reference 6 to a broader range of cross sections. Fourth, while Jorgensen discusses the impact of crossflow drag coefficient as a function of Reynolds number, he does not offer any methodology to correct for the sudden decrease in the crossflow drag coefficient for Reynolds numbers above the critical value as a function of body cross-sectional shape. Finally, configuration aerodynamics need to be defined in such a way as to allow the interference terms between the wing and body to include nonlinearities. Reference 13 already has these nonlinearities included for circular bodies. This methodology has been validated to high AOA and for a large range of Mach numbers and configurations. However, this methodology also needs to be adjusted for the noncircular bodies being considered.

The remainder of the analysis section will take each of the problems discussed and define the modifications or new methods necessary to attempt to achieve a more accurate and robust way of treating noncircular bodies than is available in either Reference 6 or 11.

2.2 BODY ALONE AXIAL FORCE APPROACH

The axial force coefficient is composed of three components which arise from the wave drag generated by the flow as it is compressed on the body surface, the friction of the air as it passes over the body, and the pressure on the afterbody or base caused by the separation of the flow from the body surface. Mathematically, this is represented by

$$C_A = C_{A_W} + C_{A_f} + C_{A_B} \tag{8}$$

Reference 6 alludes to the use of the equivalent axisymmetric axial force for use in the noncircular body. It is reasonable to assume that the base drag methodology of Reference 13 could be extended to a noncircular body by use of the equivalent diameter. That is

$$C_{A_B} = -\left(C_{P_B}\right)_{3\text{-}D} \left(\frac{d_B}{d_{ref}}\right)^3_{eq} ; \begin{pmatrix} \text{squares, triangles} \\ \text{ellipse, } a/b \le 1.5 \end{pmatrix} \tag{9A}$$

Here, $(d_B)_{eq}$ and $(d_{ref})_{eq}$ of Equation (9A) are the base and reference diameters of the equivalent body of revolution computed from Equation (5) and C_{P_B} is the negative base pressure coefficient that occurs on a circular cylinder with no boattail as a function of Mach number and AOA.

Equation (9A) applies to configurations which, while noncircular in shape, are not very flat. For elliptical cross-section bodies with large values of semimajor to semiminor axis, the Equation (9A) relation does not hold. That is because the base pressure coefficient is more like a 2-dimensional (2-D) versus a 3-D value and the boattail effect should be squared rather than cubed. Hence, for ellipses with $a/b \ge 5$,

$$C_{A_B} = -\left(C_{P_B}\right)_{2\text{-}D} \left(\frac{d_B}{d_{ref}}\right)^2_{eq} ; \begin{pmatrix} \text{ellipses with} \\ a/b \ge 5.0 \end{pmatrix} \tag{9B}$$

For ellipses, where $1.5 \le a/b < 5$, a linear interpolation between Equations (9A) and (9B) is assumed. That is

$$C_{A_B} = -\left(C_{P_B}\right)_{3\text{-}D} \left(\frac{d_B}{d_{ref}}\right)^3_{eq}$$

$$- \left(\frac{d_B}{d_{ref}}\right)^2_{eq} \left[\left(C_{P_B}\right)_{2\text{-}D} - \left(C_{P_B}\right)_{3\text{-}D} \left(\frac{d_B}{d_{ref}}\right)_{eq}\right] \left(\frac{a/b - 1.5}{3.5}\right) ; \begin{pmatrix} \text{ellipse with} \\ 1.5 < a/b < 5.0 \end{pmatrix} \tag{9C}$$

Intuitively, the skin-friction axial force of a noncircular body should be directly proportional to the wetted area of the air on the body surface. As a first approximation, this can be estimated by the ratio of the circumference on the noncircular body to that of the circular body. Then

$$(C_{A_f})_{NC} = \left(\frac{(Cir)_{NC}}{2\pi r_{eq}} \right) (C_{A_f})_{eq} \qquad (10A)$$

$(C_{A_f})_{eq}$ is the skin-friction drag of the equivalent circular body of radius r_{eq}.

The wave drag term of Equation (8) is more complicated than the other two components due to the fact it is a function of the slope along the body surface as well as the area distribution. Hence, to compute the wave drag on an equivalent axisymmetric body would require the product $(r\ dr/dx)_{eq}$ to be the same as for the noncircular body. The best way to analyze this term would be through numerical computations using codes such as full Euler[3] or Navier Stokes.[4] However, since time or funding does not permit this alternative at present, it will be assumed the wave drag term of the noncircular cross-section body is the same as that of the equivalent axisymmetric cross-section body.

To validate or modify the present approach to determine the ratio of $(C_A)_{NC}/(C_A)_{eq}$, ballistic range tests are being conducted at Eglin Air Force Base in Florida. Tests will be conducted using 10-caliber long, fin stabilized, ballistic rockets of various cross-sectional shapes including circles, ellipses, triangles and squares over a Mach range of 0.75 to 3.5. The axial force of the fins will be subtracted from the total axial force to give the body alone values. Of course, the experimental results will not break down the components of drag as in Equation (8). Since the Eglin Ballistic Range tests will not be available for some time, the approach used during the interim period for body alone axial force at zero AOA will be Equations (9), (10) plus the assumption that

$$(C_{A_w})_{eq} = (C_{A_w})_{NC} \qquad (10B)$$

The method of Reference 15 will be assumed for AOA changes in C_A and Reference 13 will be used for fin values of C_A. Hence, to compute C_A, we first of all determine the equivalent axisymmetric body. The axial force is computed as currently done in the AP95[13] code for this equivalent axisymmetric body with or without fins. The body alone value of C_A is then adjusted using Equations (9) and (10) for the appropriate noncircular shape and the fin values of C_A are held constant. C_A at AOA is then adjusted according to Reference 15.

2.3 VALUES OF $(C_n/C_{n_O})_{SB}$ AND $(C_n/C_{n_O})_N$

When applying Equations (3), (4), (6) and (7) to noncircular bodies, values of the parameters $(C_n/C_{n_O})_{SB}$ and $(C_n/C_{n_O})_N$ are required for the particular noncircular shape of interest. C_{d_C} of these equations remains the crossflow drag coefficient of a circular cylinder with the radius defined by Equation (5). Values of these parameters for ellipses using both SB and MNT are given in Reference 6 and shown here in Figure 2 for convenience.

Values of $(C_n/C_{n_O})_N$ were not available for many other cases of interest. As a result, Appendix A derives this parameter for several cases of interest including squares and triangles with

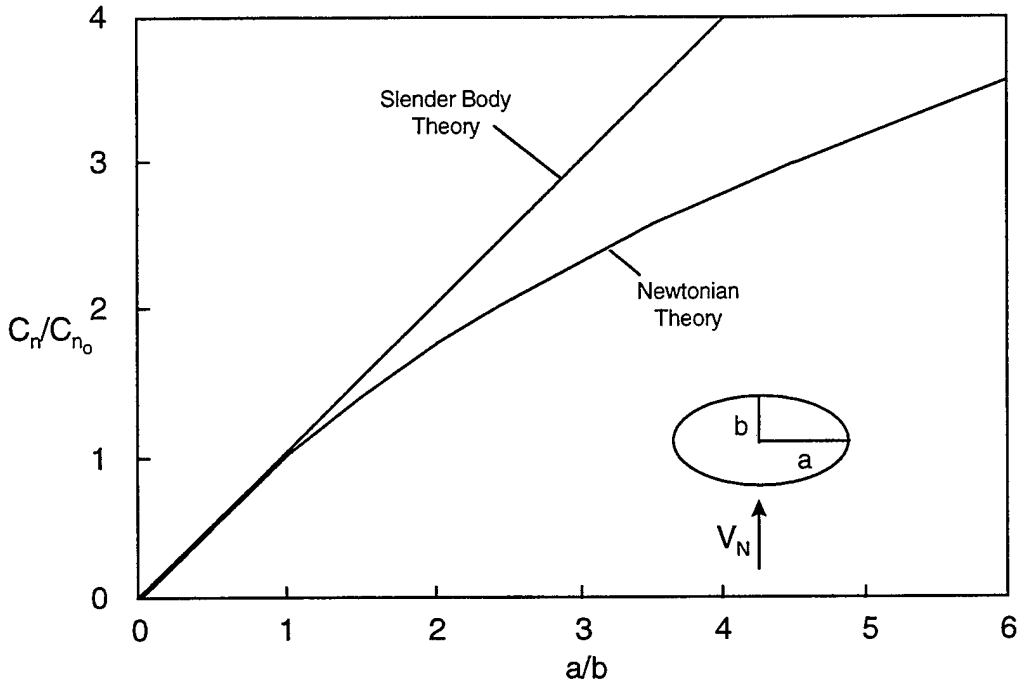

FIGURE 2. RATIO OF LOCAL NORMAL-FORCE COEFFICIENT FOR AN ELLIPTIC CROSS SECTION TO THAT FOR THE EQUIVALENT CIRCULAR CROSS SECTION

various corner radii. Reference 16 contained approximate values of the slender body apparent mass parameters which allowed computation of $(C_n/C_{n_o})_{SB}$ for the configurations in the appendix with no corner radius. These values were than allowed to go to one in a linear fashion when k goes to 0.5. Values of $(C_n/C_{n_o})_N$ and $(C_n/C_{n_o})_{SB}$ are given in Figures 3 and 4 for the square and triangular cross-sections, respectively, as a function of the corner radius parameter k. Values of $(C_n/C_{n_o})_{SB}$ at $k = 0$ were computed by

$$\left(\frac{C_n}{C_{n_o}}\right)_{SB} = \frac{A_i}{A_{eq}} \tag{11}$$

where A_i is the apparent mass values given by Reference 16 and A_{eq} is the equivalent circular cross-section area for each of the noncircular shapes of interest. Values of d_{eq} for these shapes are defined in Appendix A.

It is interesting to note from Figures 3 and 4, that SBT gives constant values of $(C_n/C_{n_o})_{SB}$ for both the triangle and square[16] independent of their orientation. On the other hand, Newtonian theory values of $(C_n/C_{n_o})_N$ vary depending on the orientation of the triangle or square. Newtonian impact theory is a function of the sine of the angle between the velocity vector and a tangent to the body surface to the second power. As a result, the configuration which has the base of the triangle

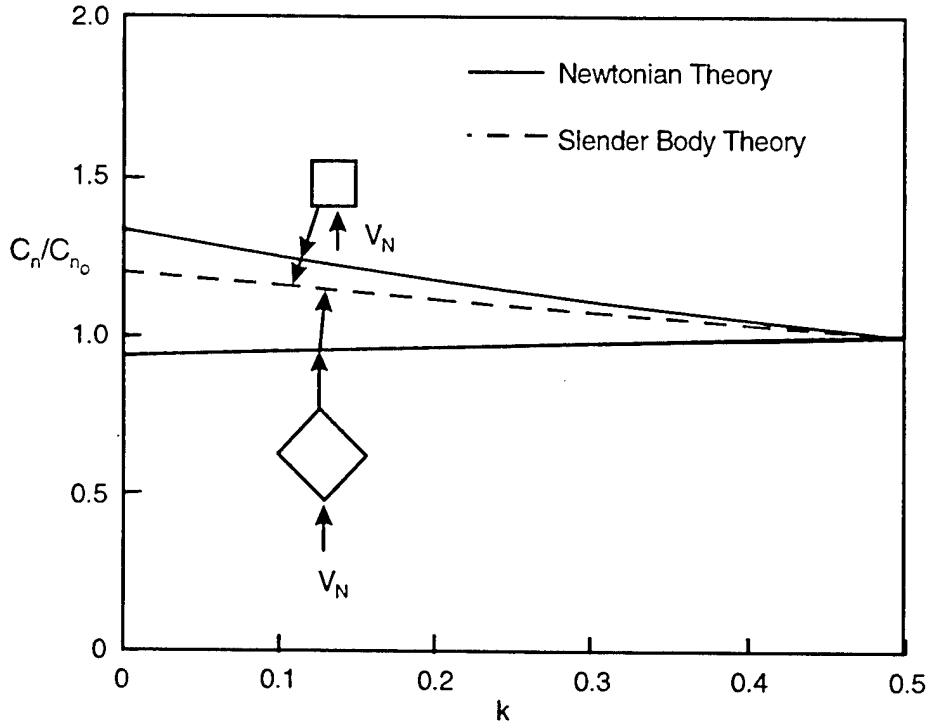

FIGURE 3. RATIO OF LOCAL NORMAL-FORCE COEFFICIENT FOR A SQUARE CROSS SECTION TO THAT FOR THE EQUIVALENT CIRCULAR CROSS SECTION

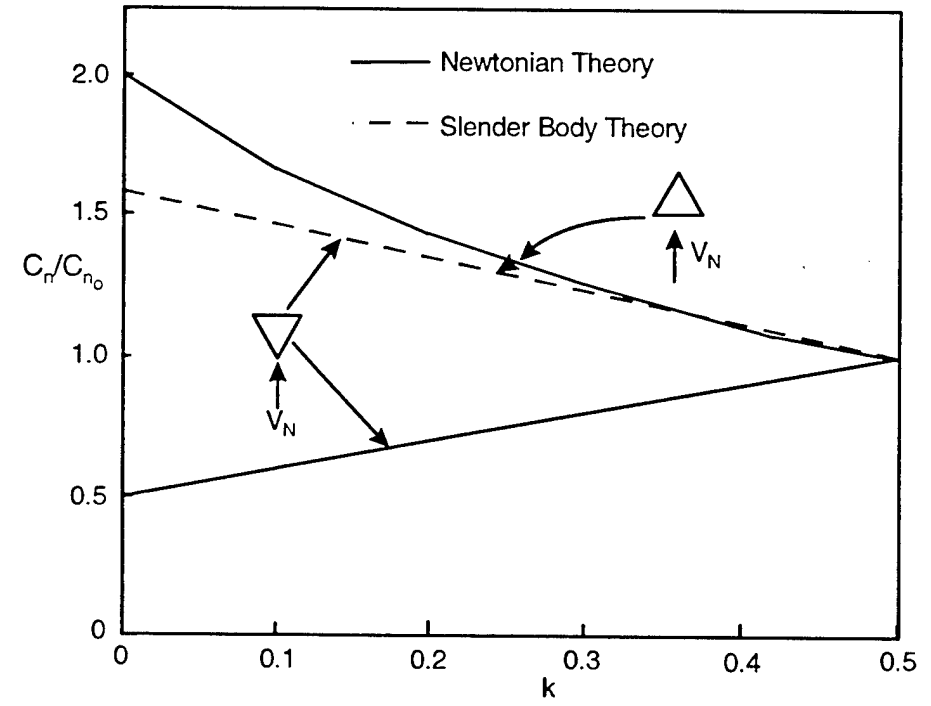

FIGURE 4. RATIO OF LOCAL NORMAL FORCE COEFFICIENT FOR A TRIANGULAR CROSS SECTION TO THAT FOR THE EQUIVALENT CIRCULAR CROSS SECTION

normal to the flow has a fairly high value of the parameter $(C_n/C_{n_o})_N$, whereas the value when the triangle is inverted is about 1/4 of the larger value when the corner is sharp (k = 0). On the other hand, Reference 16 shows the apparent mass to be independent of orientation of the triangle and square so a value of SBT is obtained for the parameter $(C_n/C_{n_o})_{SB}$ that is independent of orientation and is between the two values computed by Newtonian theory for both the square and triangle.

2.4 NEWTONIAN CORRECTION FACTOR

Figures 3 and 4 address one of the weak areas in the References 6 and 11 methodology discussed previously. A second problem that needs to be addressed is to provide a correction as a function of Mach number for the Newtonian theory curves of Figures 2 through 4. Since the slender body curves are used at low AOA, and values of normal force are small, it is not as critical that these curves he corrected for nonslender bodies. On the other hand, the Newtonian theory curves are used at high AOA and could potentially be erroneous at lower Mach numbers.

Equations (6) and (7) for the body alone normal force and pitching moment will therefore be rewritten to include the factor NF which represents the correction in the modified Newtonian values of $(C_n/C_{n_o})_N$ due to the crossflow Mach number not being infinite. Thus

$$C_N = C_{N_L}\left(\frac{C_n}{C_{n_o}}\right)_{SB} + C_{N_{NL}}\left(\frac{C_n}{C_{n_o}}\right)_N NF \tag{12}$$

$$C_M = C_{M_L}\left(\frac{C_n}{C_{n_o}}\right)_{SB} + C_{M_{NL}}\left(\frac{C_n}{C_{n_o}}\right)_N NF \tag{13}$$

The subscript L and NL in Equations (12) and (13) represent the linear and nonlinear normal force and pitching moment components respectively. Both Equations (12) and (13) are based on body aerodynamics of a circle of equivalent cross sectional area to that of the noncircular body cross section.

To compute NF, use will be made of available experimental data to compare $(C_n/C_{n_o})_N$ of Figures 2 through 4. If values of these parameters are not available directly, then the parameter NF can be approximated by comparing total force and moment data from tests to that predicted by Reference 13 when NF is 1. NF can then be computed to bring the theory more in line with experimental data. References used for this phase of the work were 6, 7, and 17 through 24.

A brief explanation of why the factor NF is needed is in order. Basically, Newtonian impact theory assumes all the momentum of an air particle is lost upon direct impact on a body surface. The theory is derived based on very high Mach numbers and past comparisons with experiment have shown the simple theory does indeed give quite accurate pressure information on simple body shapes

as Mach number becomes large and the particle impact angle is near normal to the surface. As a consequence of the momentum of each air particle being deposited on a surface upon impact, the pressure coefficient on all areas that the flow does not see directly ("shadowed regions"), or leeward plane areas, is zero. This Newtonian assumption becomes increasingly erroneous as Mach number decreases. While the ratio $(C_n/C_{n_o})_N$ tends to mitigate the error somewhat, due to the fact the error occurs on both the circular and noncircular configurations, it is logical to assume that the error is configuration-dependent. If Equations (12) and (13) were applied only for crossflow Mach numbers greater than about 2 to 5, one could probably neglect the factor NF and still achieve reasonable accuracy for engineering codes. However, since most tactical weapons fly in the range of freestream Mach numbers less than 6, it is very important to have the factor NF defined.

The first noncircular configuration is the elliptical cross section of Figure 2. This configuration has the most experimental data available and therefore is the easiest to define the factor NF. Results for elliptical configurations with a/b = 0.5, 2.0 and 3.0 are given in Figure 5. Figure 5 was derived primarily from the data of Jorgensen[6,7] and Shereda, et al.[24] in conjunction with the AP95.[13] As a result of the combined usage of data and a code, some of the factor NF in Figure 5 could be from errors in the AP95 itself. However, as seen in Figure 5, if the errors are from the AP95 they are fairly consistent in terms of a general trend as a function of a/b.

Figure 5 was derived for AOAs greater than 20 deg since this is the region where one obtains the largest amount of separation in the leeward plane of the vehicle and therefore the region where Newtonian theory is least accurate. To blend in the factor $(NF)_1$ with AOA, a linear variation is assumed between AOA 0 and 20 deg. That is,

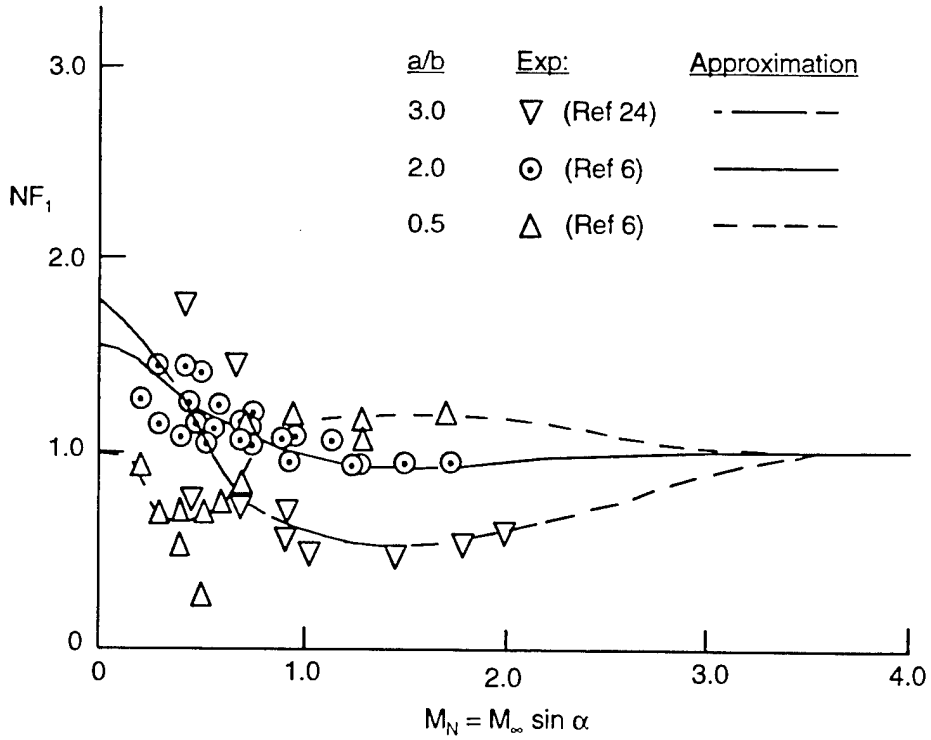

FIGURE 5. NEWTONIAN CORRECTION FACTOR FOR AN ELLIPTICAL CROSS SECTION ($\alpha \geq 20$ deg)

$$NF = 1 + [(NF)_1 - 1]\frac{\alpha}{20} \quad ; \quad \alpha \le 20$$
$$NF = (NF)_1 \quad ; \quad \alpha > 20 \qquad (14A)$$

Several points are worthy of note in Figure 5. First of all, for values of a/b < 2.0, NF_1 is close to 1 at crossflow Mach numbers of 2.0 and higher. Secondly, at low crossflow Mach numbers, the a/b = 2.0 and 3.0 configurations generate a large amount of nonlinear normal force compared to a circle. This is partly explained by Reference 25. Reference 25 shows that the drag coefficient of various flat shapes coalesce at high Mach number but vary widely at low Mach number. The ellipse approaches a flat surface as a/b gets large. Thirdly, the configuration for a/b = 0.5 appears to indicate a region of supercritical crossflow Reynolds number around $M_N = 0.5$ where the factor NF_1 decreases below 1. However, for a/b = 0.5, the value of (NF) more closely resembles Newtonian theory (NF is closer to 1) than the larger values of a/b when M_N is less than about 0.8. Finally, to estimate the effects of elliptical shapes other than a/b = 0.5, 2.0, or 3.0, a linear assumption is made that the factor varies between 1.0 for a/b = 1.0 to its value in the Figure 5 for a/b other than 1. Mathematically this is expressed as:

$$\begin{aligned}
NF &= (NF)_{a/b=3} && ; \quad a/b > 3.0 \\
NF &= \left\{(NF)_{a/b=3} - (NF)_{a/b=2}\right\}(a/b - 2) + (NF)_{a/b=2} && ; \quad 2 \le a/b \le 3.0 \\
NF &= \left\{(NF)_{a/b=2} - 1\right\}(a/b - 1) + 1 && ; \quad 1 \le a/b < 2.0 \\
NF &= \left\{(NF)_{a/b=.5} - 1\right\} 2(1 - a/b) + 1 && ; \quad 0.5 \le a/b < 1.0 \\
NF &= (NF)_{a/b=0.5} && ; \quad a/b \le 0.5
\end{aligned} \qquad (14B)$$

The second configuration of interest is the square cross section (see Figures 1 and 3). Unfortunately, there are not as much data available for the square and triangular cross sections as needed, particularly at Mach numbers between about 1 and 5. However, lower Mach number data is available for crossflow drag coefficient (see References 17, 18, 20, 21, 22, 25 through 31) and some higher Mach number data in Reference 7. The data of References 20 and 31 in particular were useful in defining the Newtonian correction factor at low crossflow Mach numbers. Both these tests had the model mounted in a 2-D flow sense and normal to the walls of the wind tunnel. Thus

$$M_N = M_\infty \sin 90 = M_\infty$$

The data from both References 20 and 31 were at a subcritical Reynolds number up to supercritical. The values of crossflow drag coefficient were taken at subcritical Reynolds numbers for application here and at a $M_N \approx 0.4$.

To compute a Newtonian correction factor from the data of References 20 and 31 basically involves computing the value of $(C_n/C_{n_O})_N$ experimentally and comparing it with the analytical curve of Figure 3. That is

$$NF = \frac{(C_d/C_{d_C})\ (W_m/d_{eq})}{(C_n/C_{n_O})_N} \tag{15}$$

The values of C_d and C_{d_C} come from the References 20 and 31, the values of W_m and d_{eq} from Appendix A for both the square in the $\Phi = 0$ and 45 deg roll orientations, and $(C_n/C_{n_O})_N$ from Figure 3. It should be pointed out that C_{d_C} measured in Reference 20 was the traditional value of 1.2 whereas that measured in Reference 31 was 1.0. It was noted in Reference 31 that flow velocity was lost through holes in the mount of the wind tunnel wall at each end of the model which accounted for this loss. Hence, some of the data of Reference 31 could have been affected by this loss, but in comparing it to Reference 20 data, they appeared to be consistent for configurations other than the circular cylinder values.

Results of the Equation (15) calculations at $M_N \cong 0.40$, based on the Reference 31 and 20 data respectively, are shown in Figure 6A. Figure 6A shows the factor is much higher for the square rotated in the $\Phi = 45$ deg roll position than in the $\Phi = 0$ roll. This makes sense from the standpoint that it is well known that Newtonian theory gives a reasonable approximation to the pressure near the region of a blunt tip, even though the Mach number is low. On the other hand, when one gets away from the blunt tip, the pressures deviate substantially from experiment. Also, for both the squares in the $\Phi = 0$ and $\Phi = 45$ deg roll orientations, Newtonian theory gives $C_P = 0$ in the rear of the configuration, whereas experimental data shows a fairly large negative pressure coefficient. The combination of these two factors is why the correction factor is needed.

Figure 6A gives values of NF near $M_N = 0.4$. To correct for Mach number, Reference 7 data was used in conjunction with the aeroprediction code to back out the Newtonian correction factor for crossflow Mach numbers other than 0.4. Reference 7 had data for Mach numbers of 1.98 and 3.88 for AOAs to 20° and 14° respectively on squares, diamonds, triangles and inverted triangles with sharp corner radius. Hence, crossflow Mach numbers of 0 to about 1.0 can be obtained for $k = 0$. Figure 6B shows the results from the Reference 7 data for crossflow Mach numbers less than about 0.95 for squares at both the 0 and 45° roll orientations. This data is then extrapolated to a value of NF = 1.0. For squares at $\Phi = 0°$, a value of 1.0 for NF is obtained at $M_N = 0.4$, whereas for diamonds, NF = 1.0 at $M_N = 2.6$. Note that the Reference 7 data is in agreement with the Reference 21 and 30 data at $M_N = 0.4$. That is, the value of NF from Figure 6A is identical to that in 6B at $M_N = 0.4$.

Now to derive a value of NF_0 (NF at $M_N = 0$) as a function of corner radius, Figures 6A and 6B have been combined. The value of NF in Figure 6A at $k = 0$ has been adjusted upward to correspond to the value at $M_N = 0$ in Figure 6B. Then the value of NF_0 follows the trends in Figure 6A except for the initial point at $k = 0$ being adjusted upward. The adjusted values of NF_0 for the squares and diamonds are given in Figure 6C.

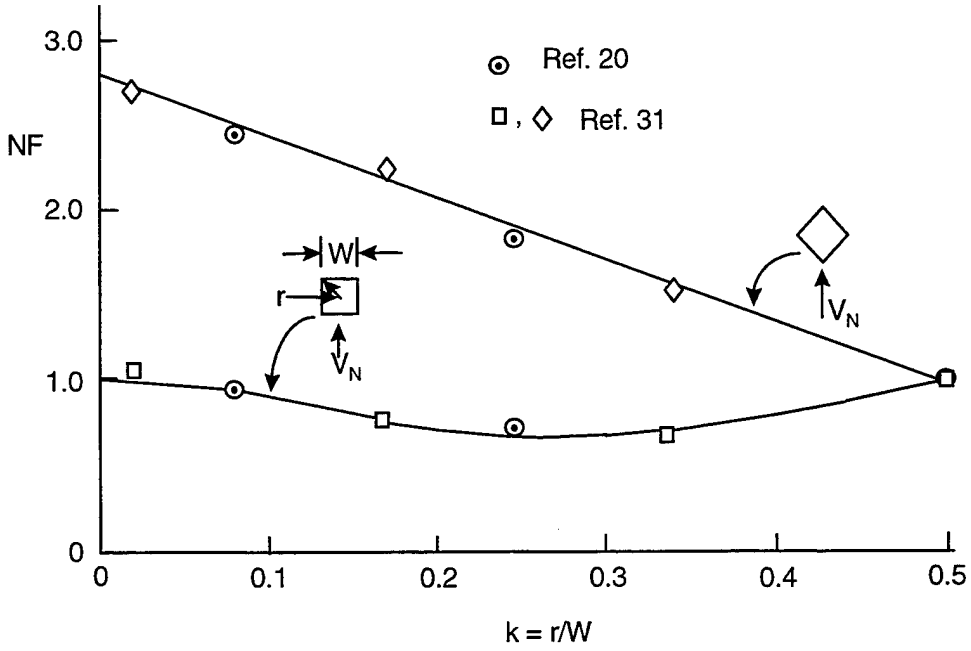

FIGURE 6A. NEWTONIAN CORRECTION FACTOR FOR SQUARES AS A FUNCTION OF CORNER RADIUS AT $M_N \cong 0.4$

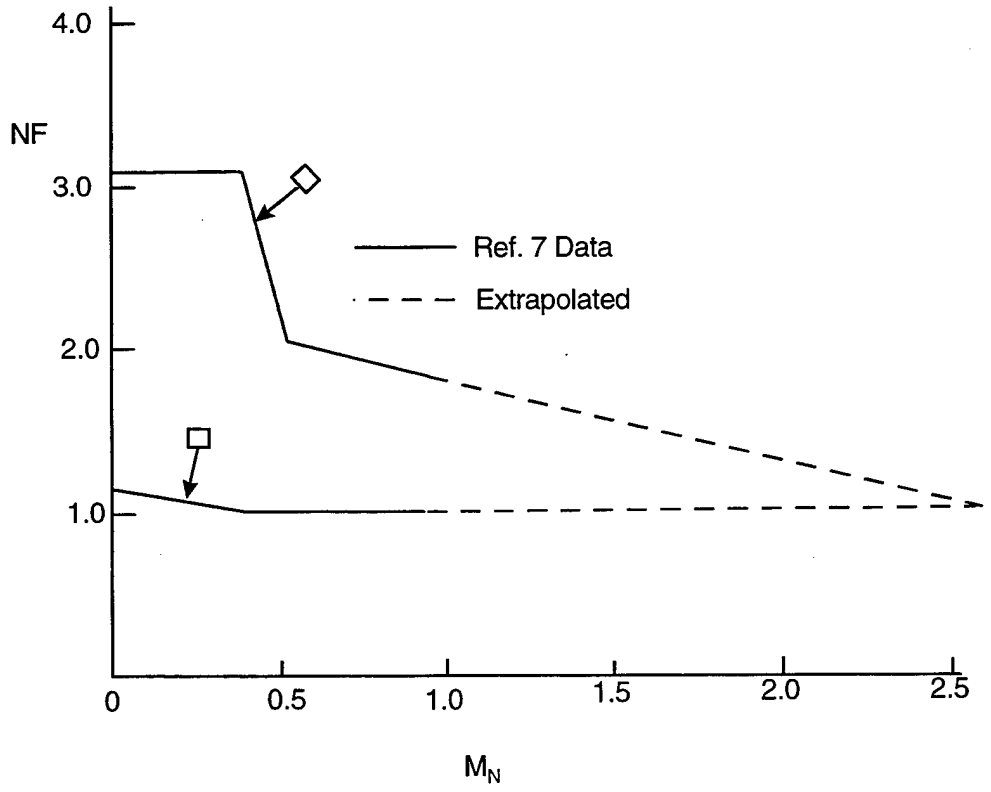

FIGURE 6B. NEWTONIAN CORRECTION FACTOR FOR SQUARES AS A FUNCTION OF CROSSFLOW MACH NUMBER (k = 0)

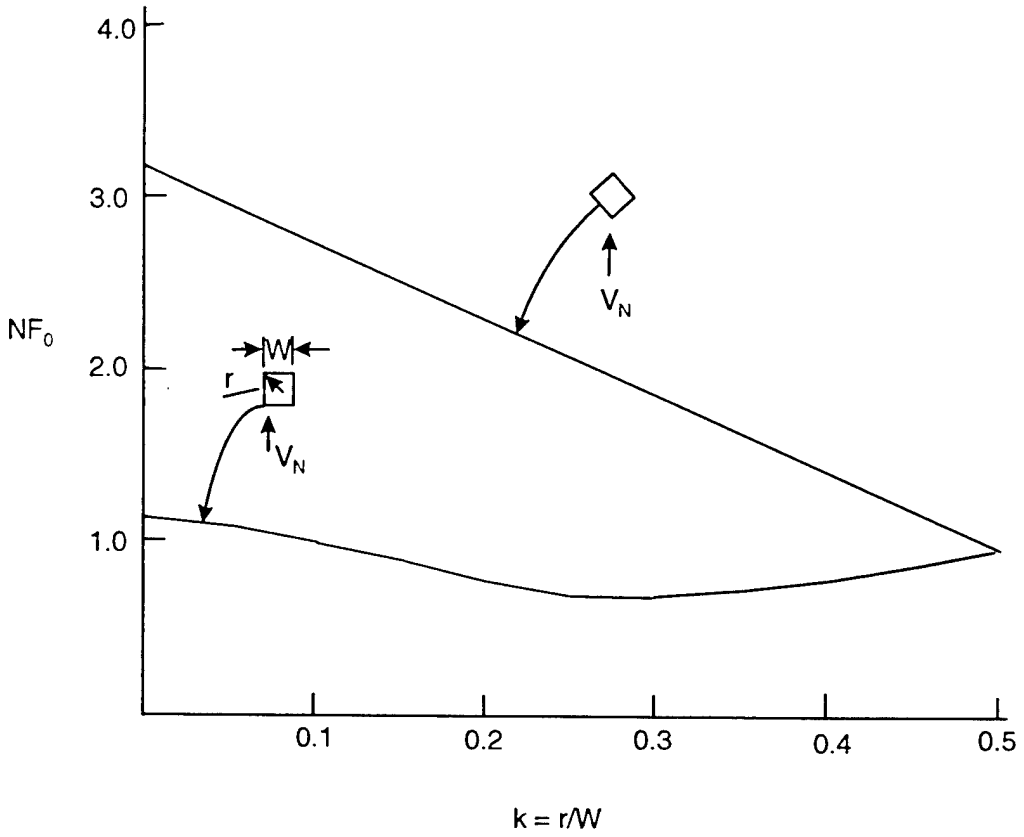

FIGURE 6C. NEWTONIAN CORRECTION FACTOR FOR SQUARES AS A FUNCTION OF CORNER RADIUS AT $M_N = 0$

To compute the Newtonian correction factor for squares, one first of all picks off the value of NF_0 from Figure 6C as a function of k and roll orientation. Then Figure 6B is used to correct the value of NF_0 as a function of crossflow Mach number. The mathematics of this process are as follows:

Square:

$$
\begin{aligned}
NF &= NF_0 && ; \quad M_N \le M_{N_0} \\
NF &= NF_0 - \left(\frac{M_N - M_{N_0}}{1 - M_{N_0}} \right) (NF_0 - 1) && ; \quad M_{N_0} < M_N \le 1.0 \\
NF &= 1.0 && ; \quad M_N > 1.0
\end{aligned}
\tag{16A}
$$

Diamond:

$$
\begin{aligned}
NF &= NF_0 && ; \quad M_N \le M_{N_0} \\
NF &= NF_0 - \left(\frac{M_N - M_{N_0}}{0.55 - M_{N_0}} \right) \left[0.55 \, (NF_0 - 1) \right] && ; \quad M_{N_0} < M_N \le 0.55 \\
NF &= (NF)_{M_N=0.55} - \frac{M_N - 0.55}{2.05} \left[(NF)_{M_N=0.55} - 1 \right] && ; \quad 0.55 < M_N \le 2.6 \\
NF &= 1.0 && ; \quad M_N > 2.6
\end{aligned}
\tag{16B}
$$

where

$$
\begin{aligned}
M_{N_0} &= 0.4 - 2.67k \; ; \; k \le 0.15 \\
M_{N_0} &= 0 \; ; \; k > 0.15
\end{aligned}
\tag{16C}
$$

Equation (16C) tends to delay the decrease in NF with increasing values of M_N somewhat if the square has fairly sharp or sharp corners (similar to the large a/b elliptic case). However, both the sharp and rounded results of NF computed by Equation (16) approach 1.0 as M_N approaches 1.

Data for triangular cross sections is more meager than for squares. Reference 31 has the best data, with some data available in References 19 and 20. Using the data from these references, all of which are for low Mach number, a process similar to that for the square cross-section can be used to derive a Newtonian correction factor for triangular shapes. This factor is shown in Figure 7A. The only data that was available was for k = 0.02, 0.1 and 0.4. Hence, between these points a straight line was drawn. Once again it is interesting to note that when the flow is to the flat side of the triangle, the Newtonian correction factor is close to 1. However, when the flow hits the angled side of the triangle, the correction factor is much higher. Once again, the process used for the squares to correct for crossflow Mach numbers other than 0.4 will be used for the triangles.

Figure 7B thus gives the value of NF as a function of crossflow Mach number using a combination of Reference 7 and the APC as done for the squares. Then Figure 7C combines Figures 7A and 7B to correct for corner radius based on a crossflow Mach number of 0. The mathematics that defines the calculation of NF is given by Equation (16D) for the triangle and Equation (16E) for the inverted triangle.

Triangle:

$$
\begin{aligned}
NF &= NF_0 && ; \quad M_N \le M_{N_0} \\
NF &= NF_0 - \left(\frac{M_N - M_{N_0}}{0.80 - M_{N_0}} \right) (NF_0 - 1) && ; \quad M_{N_0} < M_N \le 0.80 \\
NF &= 1.0 && ; \quad M_N > 0.80
\end{aligned}
\tag{16D}
$$

Inverted Triangle:

$$
\begin{aligned}
NF &= NF_O - \left(\frac{M_N - M_{N_O}}{2.4 - M_{N_O}} \right) (NF_O - 1) && ; \quad M_N \le 2.4 \\
NF &= 1.0 && ; \quad M_N > 2.4
\end{aligned}
\tag{16E}
$$

M_{N_O} of Equations (16D) and (16E) is defined by Equation (16C), just as for the square cross section cases.

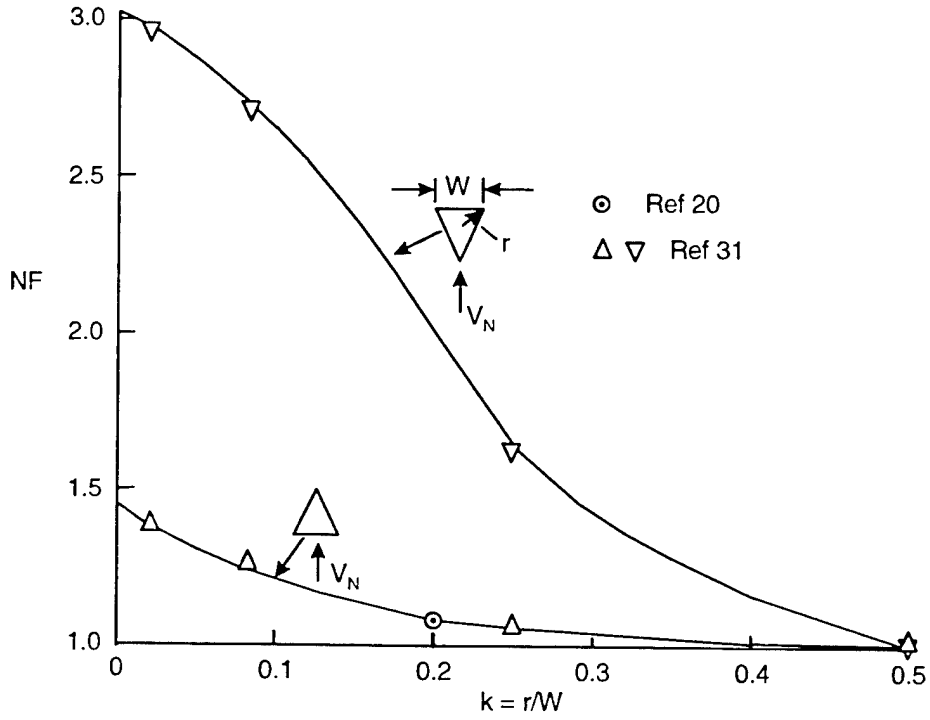

FIGURE 7A. NEWTONIAN CORRECTION FACTOR FOR TRIANGLES AS A FUNCTION OF CORNER RADIUS ($M_N = 0.4$)

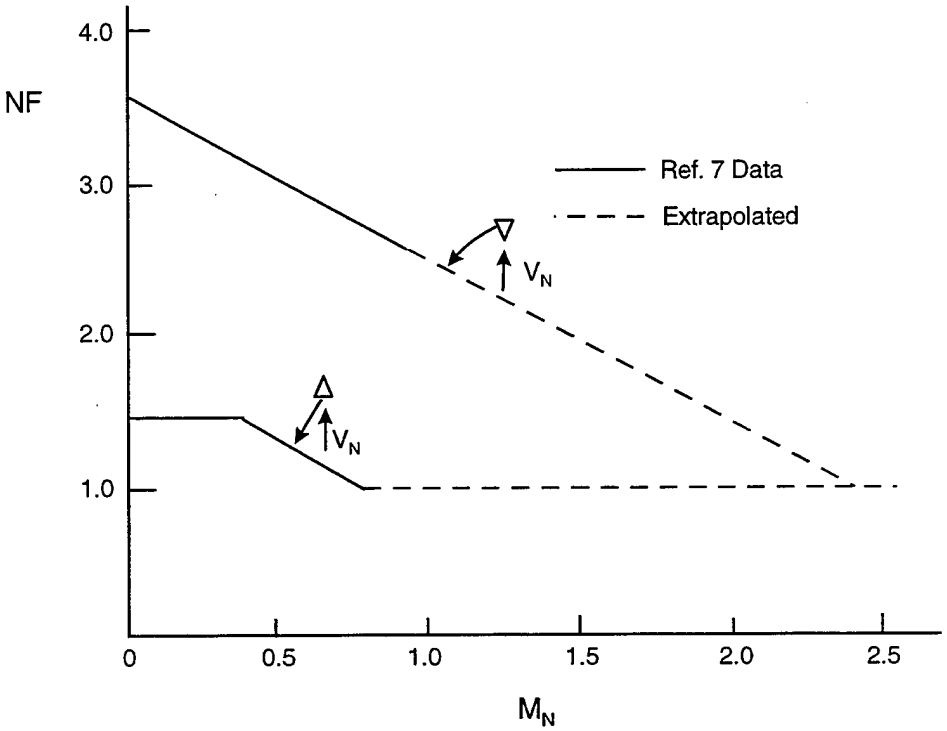

FIGURE 7B. NEWTONIAN CORRECTION FACTOR FOR TRIANGLES AS A FUNCTION OF CROSSFLOW MACH NUMBER (k = 0).

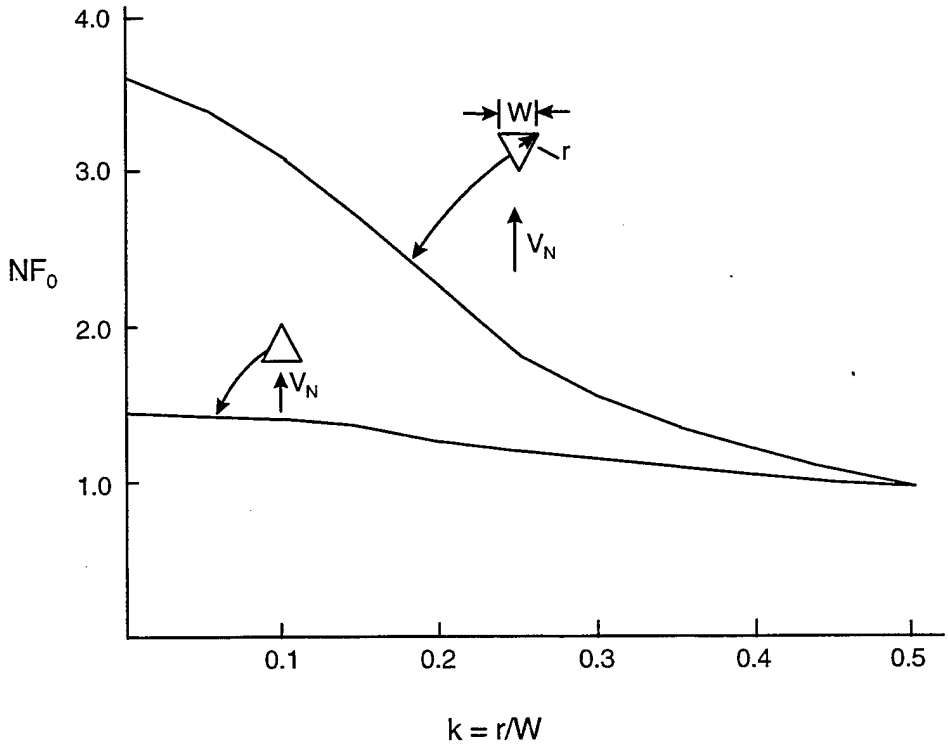

FIGURE 7C. NEWTONIAN CORRECTION FACTOR FOR TRIANGLES AS A FUNCTION OF CORNER RADIUS (M_N = 0)

2.5 REYNOLDS NUMBER EFFECT ON CROSSFLOW DRAG COEFFICIENT

Reference 13 allows for the crossflow drag coefficient to be impacted by crossflow Reynolds number. Numerous references have shown that C_{d_C} decreases rapidly above a critical crossflow Reynolds number. This value, unfortunately, varies from about 100,000 to 400,000 for circular cylinders with most data showing a critical value of 100,000 to 200,000. The variation is dependent on a lot of factors including model roughness, wind tunnel turbulence, and configuration shape just to name a few. When Reynolds numbers and crossflow Mach number go above critical values, the crossflow drag coefficient decreases rapidly and substantially until at a crossflow Mach number of about 0.6, it attains its subcritical value. The impact of this sudden drop on predicting normal force on a body alone or body-tail configuration can be quite large for lower Mach numbers where the effect is the largest.

The mechanism which causes this sudden drop in the value of C_{d_C}, when Reynolds number and crossflow Mach number exceed some critical value, is the reattachment of a separated boundary layer on the rear of the circular cylinder. This reattachment lowers the pressure drag somewhat on the rear of the cylinder, which lowers the overall crossflow drag coefficient over a range of Reynolds and Mach numbers. The present AP95[13] methodology assumes values of R_{N_C} of 330,000 and $M_{N_C} = 0$ based on the large NASA wind tunnel data set, upon which much of the methodology was derived. However, the user of the AP95 is allowed to input different values of R_{N_C} and M_{N_C} for the given configuration or wind tunnel of interest if these values are known.

The AP98 methodology will have several changes from AP95 as far as critical Reynolds number is concerned. First of all, the default values of R_{N_C} and M_{N_C} will be changed more in line with other data sets that appear to be more prevalent. These new values are therefore $R_{N_C} = 180{,}000$ and $M_{N_C} = 0.10$. The user of the AP98 still retains the option to change the default values. The next change is to allow a gradual, rather than an abrupt, change in C_{d_C} when the critical conditions are passed. At present, an effective Reynolds number is used, which is defined in Reference 13, to determine whether the R_{N_C} value has been exceeded. This value is defined by:

$$(R_N)_{eff} = \frac{R_{N_D}}{2}\left\{\frac{\cos\alpha\cot\alpha}{2} + 2\sin\alpha\right\}\left\{\frac{1 + [1 + (\tfrac{1}{2}\cot\alpha)^2]^{1/2}}{[1 + (\tfrac{1}{2}\cot\alpha)^2]^{1/2}}\right\} \tag{17}$$

Likewise the normal Mach number to a body is

$$M_N = M_\infty \sin\alpha \tag{18}$$

Thus for supercritical flow,

$$\left.\begin{array}{c}(R_N)_{eff} > R_{N_C} \\ \text{and} \\ M_N > M_{N_C}\end{array}\right\} \qquad (19)$$

For convenience, Equation (17) is given in Figure 8A as a function of AOA. As seen in Figure 8A, it is much easier to have supercritical flow at low AOAs than at higher AOA. The change being added to the AP98 is to allow the minimum value of C_{d_c} to occur at R_{N_C} + 25,000 versus when Equation (19) is satisfied. In other words, when Equation (19) is satisfied, C_{d_c} starts decreasing from its value at $R_{N_{eff}} = R_{N_C}$. When

$$R_{N_{eff}} = R_{N_C} + 25{,}000$$

the minimum value of C_{d_c} is allowed to occur.

The final change to the AP95 methodology is to take into account the fact that bodies with fins present have different physical flow characteristics than bodies alone. Most of the wind tunnel data upon which the characteristics of R_{N_C} and M_{N_C} are determined is based on body alone data. Since in the vicinity where wings or tails are present, the mechanism of boundary layer reattachment

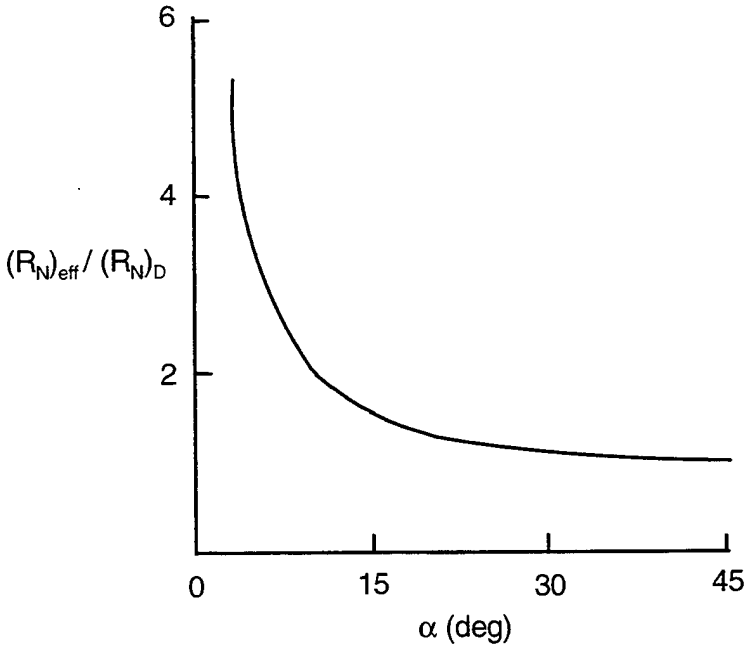

FIGURE 8A. EFFECTIVE REYNOLDS NUMBER AS A FUNCTION OF AOA

in the leeward plane will be harder to establish, the length of the body where the lifting surfaces are present will be taken out of the area for the minimum value of C_{d_c}. This length is assumed to be two root chord lengths. Thus, if $(C_{d_c})_1$ and $(C_{d_c})_2$ are the sub- and supercritical values of C_{d_c} respectively, then a modified nonlinear normal force of the body alone for supercritical flow (where wings are present) is:

$$\frac{(C_{N_{NL}})_{MOD}}{C_{N_{NL}}} = 1 - \frac{2C_r}{\ell_{ref}} + \frac{(C_{d_c})_1}{(C_{d_c})_2}\left(\frac{2C_r}{\ell_{ref}}\right) \tag{20}$$

Before discussing the impact of noncircular bodies on critical Reynolds and Mach number values, it is important to discuss how the determination of these values for a circular cylinder are arrived at. As already discussed, these values are highly dependent on the wind tunnel and model. Most wind tunnel tests give freestream Mach number and Reynolds number per foot as the two variables for a given model. Unfortunately, values of R_{N_c} and M_{N_c} are generally determined by trial and error through the use of Equations (17) through (20) in conjunction with data for a given test and theoretical predictions. Once R_{N_c} and M_{N_c} are determined for a given wind tunnel test, they appear to be reasonably constant for that test. However, they vary considerably from tunnel to tunnel and vary less significantly from test to test within a given tunnel.

One saving grace of many high Mach number calculations is that one goes through the "drag bucket" rather rapidly before AOA is large enough to give meaningful values of $C_{N_{NL}}$, which is a function of AOA squared. However, for subsonic freestream Mach numbers, it is quite important to have good values of R_{N_c} and M_{N_c} to get good comparisons of normal force on many missile configurations.

If wind tunnel data are not available for a given tunnel, the user of the AP98 can use the default values of R_{N_c} and M_{N_c}. It is also good to pick values of R_{N_c} high enough and low enough, respectively, to show the difference in aerodynamics with sub- and supercritical flow conditions. Through this process, one obtains boundaries for the aerodynamics, as well as a reasonable estimate of the aerodynamics based on default values of M_{N_c} and R_{N_c}.

Since the methodology for computing aerodynamics of nonaxisymmetric bodies is based on computing the aerodynamics of an equivalent axisymmetric body, the question arises as to whether a relationship can be derived for critical crossflow Reynolds numbers as a function of body cross-sectional shape. References 20 and 26 both give values of C_{d_c} as a function of crossflow Reynolds number and body cross-section shape for M_N values near zero.

Reference 20 correlated crossflow drag coefficient to a parameter $(R_N\, k^{1.3})$. For squares at $\Phi = 0$, it appears the critical value of this parameter based on Reference 20 can be defined as a function of k. Thus for squares at $\Phi = 0$ deg,

$$\frac{R_{N_C}}{(R_{N_C})_{k=0.5}} = \frac{.083 + 1.36k - 1.44k^2}{k^{1.31}} \; ; \; 0.02 \le k \le 0.5 \tag{21}$$

For the value of $k \le 0.02$, a value of 0.02 could be used in Equation (21). If the square is rotated to $\Phi = 45$ deg (diamond), then a better approximation to the data of Reference 20 is

$$\frac{R_{N_C}}{(R_{N_C})_{k=0.5}} = \frac{6.33k - 24.1k^2 + 26.1k^3}{k^{1.31}} \; ; \; 0.02 \le k \le 0.5 \tag{22}$$

For ellipses, an approximation to the data of Reference 18 is

$$\frac{R_{N_C}}{(R_{N_C})_{a/b=1.0}} = (a/b)^{1.5} \tag{23}$$

Finally, for triangular shapes with the base normal to the flow, the correlation equation for the square at $\Phi = 0$ deg, Equation (21) appears to correlate the data of Reference 31 reasonably well. Likewise, when the flow is in the direction of the triangular tip or inverted triangle where the base is to the rear, the equation for the square rotated 45 deg (Equation (18)) appears acceptable. Figure 8B gives the values of the functions for the squares and triangles defined by Equations (21) and (22), whereas Figure 8C gives the values of the function for ellipses defined by Equation (23).

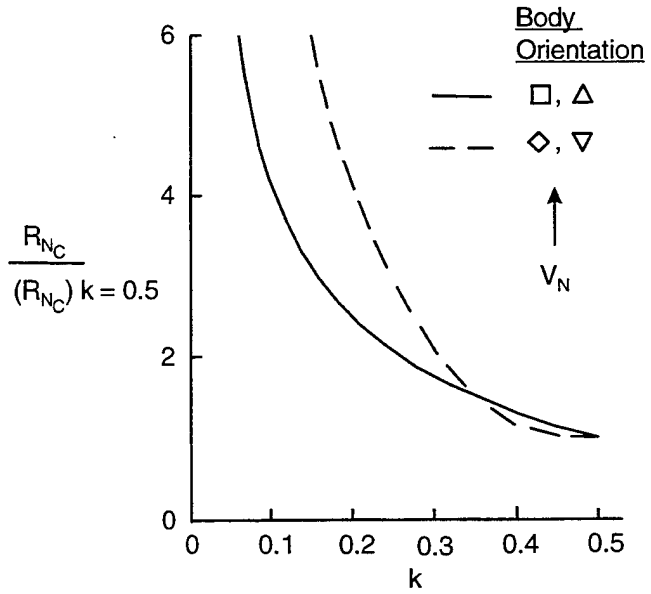

FIGURE 8B. CRITICAL REYNOLDS NUMBER FOR SQUARES AND TRIANGLES

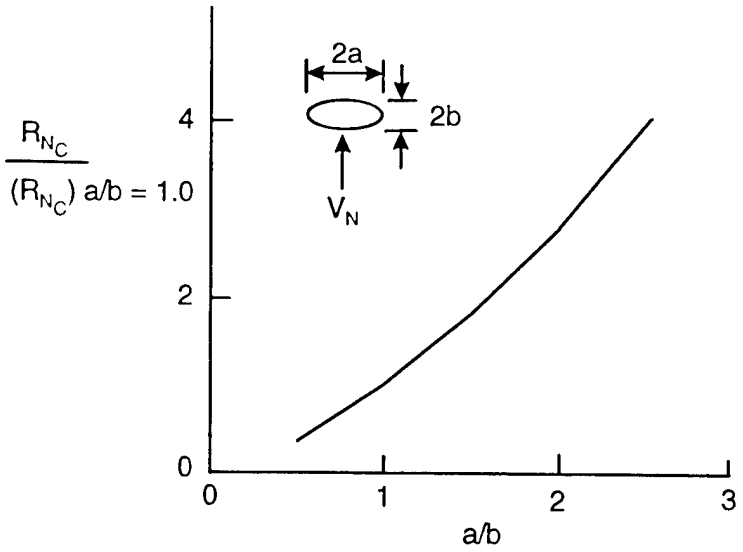

FIGURE 8C. CRITICAL REYNOLDS NUMBER FOR ELLIPSES

Physically, what Equations (21) through (23) are saying is that when the configuration has corners or approaches a flat plate in the direction normal to the velocity vector, the critical value of crossflow Reynolds number increases. The amount of this increase is proportional to the sharpness of the corners or to the elongation of the body (ellipse). This means that the mechanism which causes the "drag bucket" for circular cylinders is harder to establish itself for most noncircular cross sections.

2.6 WING-BODY CONFIGURATIONS

Jorgensen[6] used a combination of two approaches for the wing-body aerodynamics. The first approach was to simply use Newtonian theory to approximate $(C_n/C_{n_0})_N$ of Equations (1) and (2) for wing-body configurations where the body was noncircular and the wing was a simple extension of this. He then used a modified version of Reference 14 to compute the slender body or linear theory term of Equations (1) and (2). As shown in Reference 6, this approach significantly overpredicted the normal force while giving reasonable results for center of pressure. The primary reason for this overprediction of normal force was failure to account for the nonlinearities that occur in the wing-body interference factor as AOA increases.

Missile DATCOM[16] improved upon the Jorgensen[6] approach by using the equivalent AOA method[12] to incorporate nonlinearities in the wing-body interference factor. This increased the AOA capability to 20-30 deg. On the other hand, Reference 16 did not include triangles and squares for high AOA due to the fact Newtonian theory was not developed for those shapes. Also, the Newtonian correction factor for lower Mach number was not available. Reference 16 also did not include the Newtonian correction factor for all Mach numbers for ellipses.

References 13 and 32 developed a new approach for incorporating nonlinearities in the wing-body and body-wing interference factors. In this approach, each interference term was divided into a linear and a nonlinear component. The linear term was estimated by linear theory or SBT and the

nonlinear term was estimated directly through use of large missile component wind tunnel data bases. For regions where data were not available, the method was extrapolated based on engineering judgement and comparison with aerodynamics on various other missile aerodynamic data bases. The net result of this approach was average accuracy levels at roll positions of 0 and 45 deg of ±10 percent on normal and axial force and ±4 percent of body length on center of pressure to AOAs of 90 deg. Exceptions to this accuracy were at low Mach number and high AOA where wind tunnel data was in question, and at high Mach number and AOA for a configuration with two sets of lifting surfaces where internal shock interactions became important.

As a result, the improved approach for incorporating nonlinearities into the wing-body interference factors of References 13 and 32 will be the methods used here for noncircular bodies. The overall normal force coefficient equation for any wing-body-tail configuration can be written as:

$$C_N = C_{N_B} + \left[\left(K_{W(B)} + K_{B(W)}\right) \propto + \left(k_{W(B)} + k_{B(W)}\right) \delta_W\right] \left(C_{N\alpha}\right)_W$$

$$+ \left[\left(K_{T(B)} + K_{B(T)}\right) \propto + \left(k_{T(B)} + k_{B(T)}\right) \delta_T\right] \left(C_{N_\alpha}\right)_T + C_{N_{T(V)}} \qquad (24)$$

The first term in Equation (24) is the normal force of the body alone including the linear and nonlinear components; the second term is the contribution of the wing (or canard) including interference effects and control deflection; the third term is the contribution of the tail including interference effects and control deflection; and the last term is the negative downwash effect on the tail resulting from wing-shed or body-shed vortices. The uppercase K represents the interference of the configuration with respect to AOA, and the lowercase k represents the interference with respect to control deflection. The subscripts W(B) and T(B) represent the change (or interference effect) of the wing and tail in the presence of the body, whereas the subscripts B(W) and B(T) indicate the additional lift (or interference effect) on the body because of the presence of wings or tails. When Equation (1) was originally defined, it was associated with the linear aerodynamics only.[14] References 13 and 32 defined a linear and a nonlinear component of each of the terms in Equation (20). The body alone term for noncircular bodies is defined by Equation (12). The interference terms are all defined in the general form:

$$K = \underset{SBT}{K_{LT}} + \Delta K\ (M,\ AR,\ \lambda,\ \Phi,\ \alpha) \qquad (25)$$

The first term $\underset{SBT}{K_{LT}}$ is known from linear theory or SBT for circular cylinder configurations. The second term is computed empirically based on data bases and is defined in terms of tables as a function of the variables M, AR, λ, Φ and α in References 13 and 32. These tables are all based on circular bodies however. The wing alone term is estimated by a fourth order equation in angle of attack that is a function of Mach number and wing planform parameters. Finally, the last

term in Equation (24) is estimated based on slender body theory and nonlinearities incorporated through comparison to data. Once again, References (13) and (32) summarize all the nonlinear methods used in computing normal force, pitching moment, and center of pressure for axisymmetric body missile configurations.

Figure 9 gives a qualitative pictorial view of the configurations for which aerodynamics are desired. It is believed this set of configurations can be made broad enough to encompass most tactical weapons of interest to the community at large. It includes the circles of various diameter, ellipses of various eccentricity, and triangles and squares of various orientation as well as corner radius. To complement the body geometry, wings have been included at both the $\Phi = 0$ and 45 deg roll orientations on all configurations except the triangular shape (where wings were limited to the $\Phi = 0$ deg roll orientation only). The question that now must be addressed is how the Equation (25) will vary for the noncircular wing-body configurations of Figure 9.

Fortunately, Nelson,[33] Est and Nelson,[34] and Sigal[35] have performed work on $K_{W(B)}$, $K_{B(W)}$ and $k_{W(B)}$ for low AOAs for noncircular configurations. Nelson[33] and Est[34] defined the low AOA values of $K_{W(B)}$ for elliptical, square and triangular cross-section shapes at moderate supersonic Mach numbers using an Euler code in conjunction with low Mach number experimental data. Since the equivalent AOA method used SBT for $K_{B(W)}$, no equivalent data for noncircular cross sections were given in References 33 and 34 for this parameter. Figure 10A gives the wing-body interference term for elliptical cross-section shapes after being divided by that of the circular cross section near $\alpha = 0$ deg. This figure was derived from the data of Reference 33 in conjunction with the circular body results of Reference 14. The Reference 33 results were given as a function of a'/s_1, so they had to be translated to equivalent circular values through the relationship

$$\frac{r_{eq}}{s} = \frac{a'}{s_1}\left[\frac{1}{a'/s_1\left(1 - \sqrt{C_1}\right) + \sqrt{C_1}}\right] \tag{26}$$

where $C_1 = a'/b'$.

It is interesting to note from Figure 10A that for most practical missile configurations where r_{eq}/s typically varies from about 0.1 to 0.7, and a/b is generally greater than 0.5 but less than 2.0, the noncircular $K_{W(B)}$ deviates from the circular value by, at most, 18 percent and for most cases is less than that.

Reference 34 also showed that for the conditions investigated, $k_{W(B)}$ varied only slightly from SBT for any of the cross-section shapes. As a result, the current nonlinear models in References 13 and 32 will be used directly for this term.

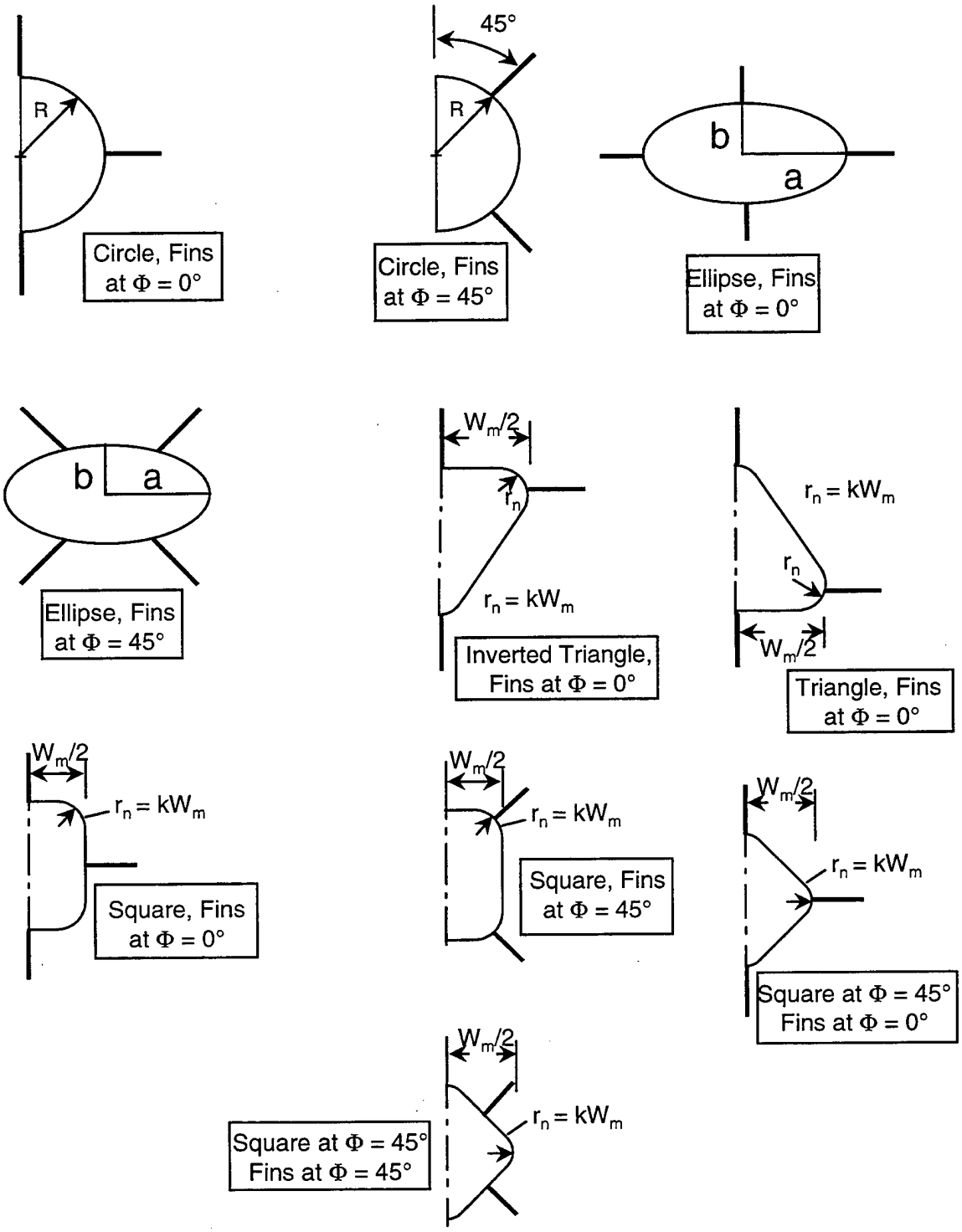

FIGURE 9. NONCIRCULAR CROSS-SECTION, WING-BODY CONFIGURATIONS FOR THE AEROPREDICTION CODE

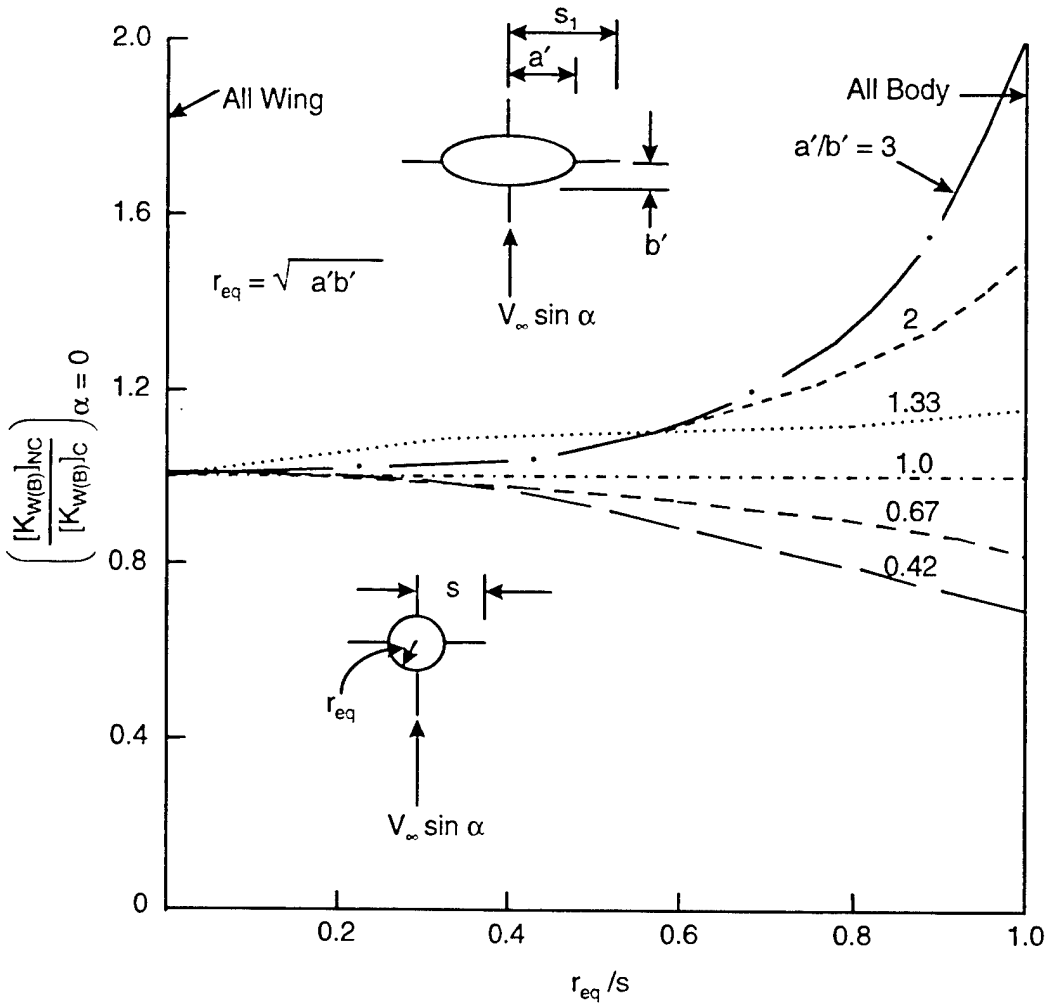

FIGURE 10A. RATIO OF WING-BODY INTERFERENCE OF ELLIPTICAL BODY TO THAT OF EQUIVALENT CIRCULAR BODY (REFERENCE 33)

As a first approximation the body-wing interference term will be assumed to vary from their circular cylinder values in a proportional manner to the wing-body carryover. That is, if one defines

$$F = \frac{\left[K_{W(B)}\right]_{NC,\,\alpha}}{\left[K_{W(B)}\right]_{C,\,\alpha}} \tag{27}$$

then

$$\left[K_{B(W)}\right]_{NC,\,\alpha} = F\left[K_{B(W)}\right]_{C,\,\alpha} \tag{28}$$

$$\left[k_{B(W)}\right]_{NC,\,\alpha} = F\left[k_{B(W)}\right]_{C,\,\alpha} \tag{29}$$

Also, as already mentioned,

$$\left[k_{W(B)}\right]_{NC,\,\alpha} = \left[k_{W(B)}\right]_{C,\,\alpha} \tag{30}$$

Sigal[35] presented a summary of methods of analysis and data bases for noncircular fuselages up through about 1990. He defined a method for calculating $K_{W(B)}$ and $K_{B(W)}$ in combination (K_{WB}) using SBT for elliptical, square and rectangular shapes. The values of K_{WB} given in Reference 35 are for the ellipse with the fins at $\Phi = 0$ (see Figure 9), and the square at $\Phi = 0$ with the fins at $\Phi = 45$ deg. The results of Reference 35 cannot be compared directly to those of Reference 34 as presented in Figure 10A, except in a qualitative sense, due to the fact Reference 35 presents $K_{W(B)} + K_{B(W)} = K_{WB}$ and Reference 34 presents only $K_{W(B)}$. However, if one assumes Equations (27) and (28) can be used in conjunction with Figure 10A, a value of K_{WB} can be computed and compared directly to that of Reference 35. This is done in Figure 10B for ellipses with values of a/b = 2.0 and 0.5 respectively. Note that the two methods tend to merge near $r_{eq}/s = 0$ and deviate substantially near $r_{eq}/s = 1.0$. The Reference 35 technique relies solely on SBT whereas the Reference 34 method is a combination of numerical calculations for $r/s \leq 0.8$ and experimental data at low Mach number for r/s = 1.0. Since Reference 33 was based on numerical calculations, it will be used as the basis for low angle of attack corrections to the circular value of $K_{W(B)}$ for elliptical cross-section shapes.

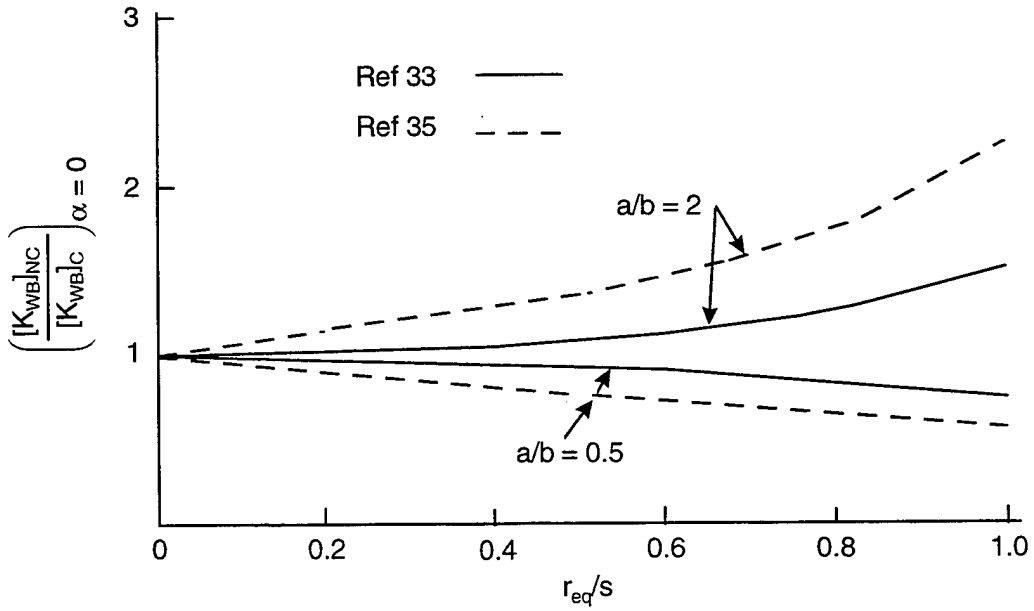

FIGURE 10B. RATIO OF TOTAL INTERFERENCE OF ELLIPTICAL BODY TO THAT OF AN EQUIVALENT CIRCULAR BODY USING TWO METHODS

It should be emphasized that Figures 10A and 10B are the low AOA values of $K_{W(B)}$ and $K_{B(W)}$, and say nothing about how $K_{W(B)}$ and $K_{B(W)}$ will vary with AOA. As a result, some assumptions will be made. References 13 and 32 defined $K_{W(B)}$ and $K_{B(W)}$ as shown in Figures 11 and 12. As seen in Figure 11, $K_{W(B)}$ has five parameters which are defined in tables as functions of wing aspect and taper ratio for various values of r/s, AOAs and M_∞'s. It will be assumed here that the Figure 10 results will be applied to the SBT value of $K_{W(B)}$ and $K_{B(W)}$ (that is, the first term of Equation (9)). Then if α_C is held constant, $dK_{W(B)}/d\alpha$ will change. However, α_D and α_M will be assumed to be the same as the circular body shape. In other words, at low to moderate AOA, the body cross section is allowed to change the interference factors from their circular-body values, whereas at high AOA, it is not. Also, as a first approximation, the values of $\Delta K_{W(B)}$ and $\Delta K_{B(W)}$ available in the AP95 will be assumed to be independent of cross-section shape at AOA.

Figure 10 was based on fins located at roll position of zero. References 13 and 32 have nonlinear treatment of fin carryover interference for both roll positions of 0 and 45 deg. As a result, the SBT results of Figure 10 will be applied to the body with the fins in both the $\Phi = 0$ and 45 deg orientation. Of course, the nonlinearities with Mach number, AOA and fin shape are different for these roll orientations and will be used as presently done in References 13 and 32. As already stated, Equations (27) through (30) are used to compute $K_{B(W)}$, $k_{W(B)}$ and $k_{B(W)}$ for noncircular cross sections when the method of References 33 and 34 are used to compute $K_{W(B)}$ for the ellipse.

Reference 34 also presented results for $[K_{W(B)}]_{\alpha=0}$ for the triangular and square shapes. Two methods were used in that reference. For k values between 0.125 and 0.5 and r/s between 0.167 and 0.667, a numerical code was used. To obtain the value of $K_{W(B)}$ for r/s = 1.0, the incompressible data of Reference 18 was used in conjunction with the incompressible form of the Bernoulli equation.[34] That is,

$$P + \frac{\rho V^2}{2} = \text{¢} = P_\infty + \frac{\rho_\infty V_\infty^2}{2} \tag{31}$$

Since, $C_P = \dfrac{P - P_\infty}{\frac{1}{2}\rho_\infty V_\infty^2}$, Equation (31) can be written as

$$C_P = 1 - \left(\frac{V}{V_\infty}\right)^2 \tag{32}$$

Values of C_p are available from Reference 18 at low Mach number and for the squares with k = 0.2 and the triangles with k = 0.175. Following Reference 34,

$$K_{W(B)} = \frac{V_{NW}}{V_\infty} = \frac{V}{V_\infty}\cos\theta \tag{33}$$

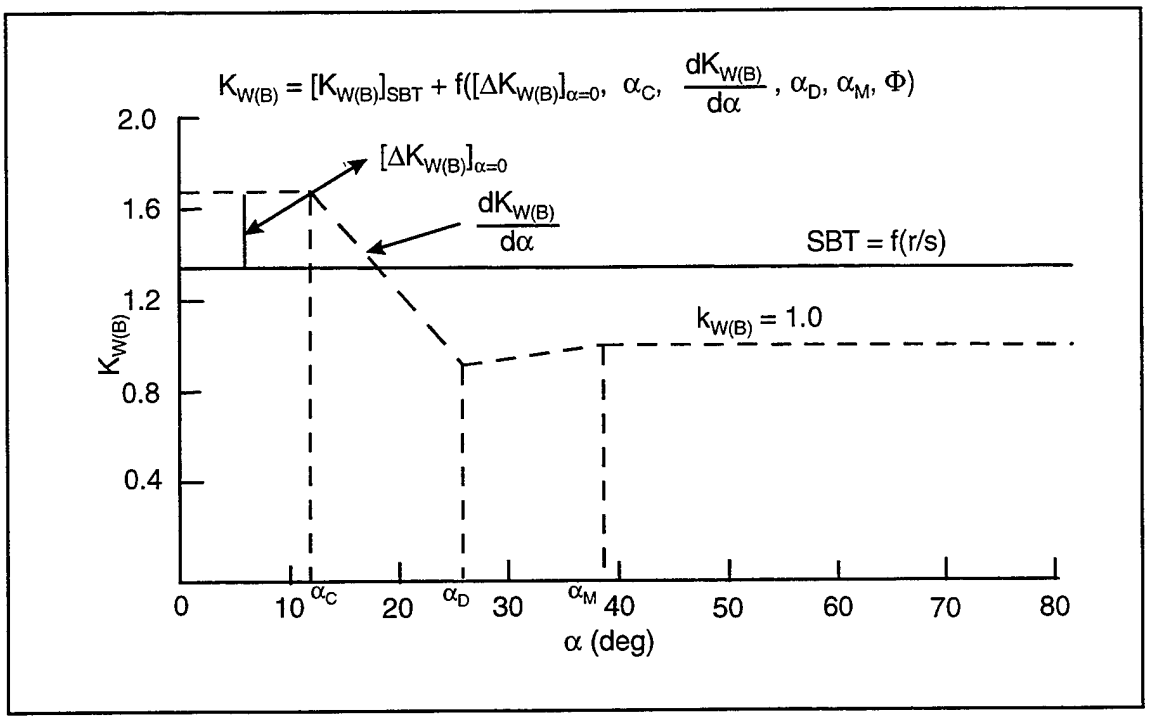

FIGURE 11. GENERIC REPRESENTATION OF $K_{W(B)}$ WITH AOA

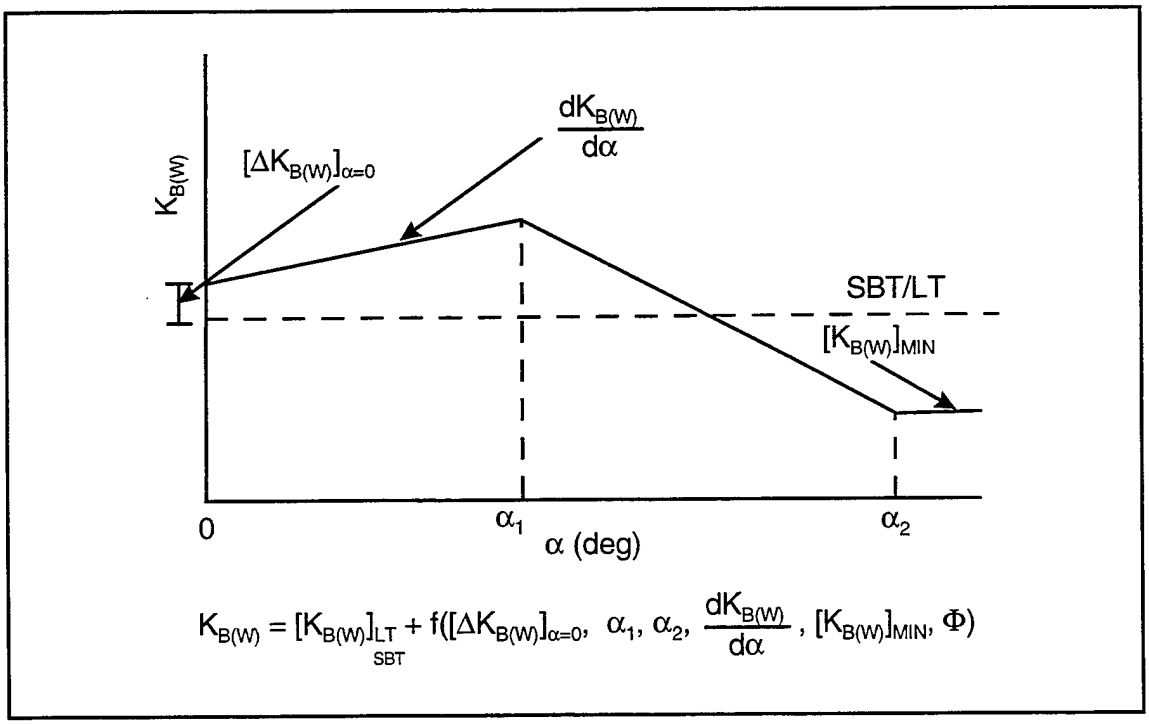

FIGURE 12. GENERIC REPRESENTATION OF $K_{B(W)}$ WITH AOA

then, using Equations (32) in (33) one obtains

$$K_{W(B)} = \cos\theta \sqrt{1 - C_P} \tag{34}$$

V_{NW} of Equation (33) is the velocity normal to the wing and θ is the angle between the normal to the wing and a tangent to the body surface. If the wing is perpendicular to the body surface then $\theta = 0$ deg and Equation (34) becomes

$$K_{W(B)} = \sqrt{1 - C_P} \tag{35}$$

Results from Reference 18 were used for C_P at the various locations of the wings in Figure 9. Several values of C_P were available in Reference 18 as a function of Reynolds number. Table 1 gives the pressure tap where values of C_P were taken from Reference 18 as a function of the body/wing orientations of Figure 9. Also given in the table are the values of $K_{W(B)}$ computed from Equation (35) where the C_P values of Reference 18 were averaged for both subcritical and supercritical Reynolds numbers. While there was significant variation in C_P for the various Reynolds numbers, as seen in Table 1, when the values were averaged, there was not a great deal of difference in $K_{W(B)}$ between the subcritical and supercritical case.

The values from Table 1 are nondimensionalized by the SBT value of $K_{W(B)}$ for a circle at r/s = 1 (which is 2.0) and plotted in Figure 13. A straight line interpolation is assumed between the value of k = 0.175 or 0.2 to 0.5. For values of $[K_{W(B)}]_{NC}$ at k = 0 and 0.1, Reference 29 data was referred to. This data, taken at M = 0.31, is also at a low enough Mach number to be considered incompressible, so it complements the data of Reference 18 quite nicely. However, only two cases

TABLE 1. ESTIMATED VALUES OF $K_{W(B)}$* FOR r/s = 1.0 AT LOW MACH NUMBER FOR VARIOUS BODY CROSS SECTIONS AND FIN LOCATIONS (DATA FROM REFERENCE 18)

Configuration Shape and Fin Location	 k = 0.2	 k = 0.2	 k = 0.2	 k = 0.2	 k = 0.175	 k = 0.175
Pressure Tap Orifices From Reference 18	11, 23	5, 20	5, 29	1, 11, 17, 23	8, 24	8, 24
$K_{W(B)}$ Subcritical R_N Supercritical R_N	1.52 1.40	1.6 1.56	1.59 1.76	1.34 1.32	1.48 1.70	N/A 1.54

* $K_{W(B)} = \sqrt{1 - \sum_{i=1}^{N} C_{P_i}/N}$

of Figure 9 were available in Reference 29. These were the cases for the square body at roll = 0 and fins at roll = 45 deg and the square body at roll = 45 deg and fins with roll = 0 deg. The other cases shown in Figure 13 were then extrapolated from their values at k = 0.2 to k = 0 based on the data for the two cases from Reference 29 as a guide. Also, note that Figure 13 was derived based on calculations of a wing-body with body circular cross-section diameter of W.

In analyzing Figure 13, it is seen that all cross sections are less efficient than the circle in producing wing-body carryover normal force near M = 0 and at r/s = 1.0. For k = 0, the value of $K_{W(B)}$ for the square varies between 1.14 and 1.5 depending on its orientation and the location of the fins, whereas the triangle and inverted triangle are approximately 1.5. These values compare to the circular cylinder value of $[K_{W(B)}]_{r/s=1} = 2.0$. Compare these values to those of Figure 10A, which are greater than one for values of $a/b \geq 1.0$. Also note that Figure 10A is based on a reference area of $\pi d_{eq}^2/4$ versus $\pi W^2/4$. This brings us to a dilemma as to why the interference factors appear so different. The answer lies in the scaling. The following several paragraphs, in addition to Appendix B, attempt to explain this. When Figure 13 is multiplied by the slender body theory scaling parameter derived in Appendix B, the results are based on $\pi d_{eq}^2/4$ and are then consistent with those of Figure 10A.

In trying to develop a simple way to calculate aerodynamics of noncircular wing-body configurations, there is an apparent scaling dilemma. The body aerodynamic calculations would appear to be more appropriately done based on a circle of equivalent cross section area to the noncircular cross section. However, the wings would like to see a body of size equal to that of a circle of diameter W (see Figure 13). This problem does not arise for bodies alone, but only when wings are placed on the body. One could therefore calculate the aerodynamics of the wing body based on a circle of diameter W and then multiply the body aerodynamics by $A_{eq}/\frac{\pi W^2}{4}$ or calculate the aerodynamics based on a circular cylinder of diameter d_{eq} and multiply the wing aerodynamics by another scaling parameter defined in Appendix B. The latter approach is chosen for the squares and triangles so a consistent approach for body alone aerodynamics is obtained with the ellipses.

In trying to understand this scaling factor, resort is made to slender-body-theory (SBT). Using SBT, one can rigorously show that there is a factor of $A_{eq}/\frac{\pi W^2}{4}$ between the equivalent circular case and a square or triangle if the square or triangle is represented by a circular cylinder of diameter W versus d_{eq}. Likewise if the diameter d_{eq} is used for the triangle or square as opposed to W, one can rigorously show there is a factor that multiplies the wing-body and body-wing contributions for low AOA. This factor is a function of r/s and wing area. Appendix B gives a thorough discussion of scaling using SBT and its implications on calculating aerodynamics of configurations with noncircular cross section bodies. The slender body scaling factors derived in Appendix B are required for use in computing aerodynamics of a nonaxisymmetric body with an axisymmetric body code.

Figure 13 gives values of $K_{W(B)}$ for squares and triangles at the limiting value of r/s = 1. Thus, to relate the value of $K_{W(B)}$ at some value of r/s other than 1 to Figure 13, a linear assumption is used, similar to what occurs in SBT.[14] Hence,

$$[K_{W(B)}]_{NC} = \left([K_{W(B)}]_{\substack{NC \\ r/s=1}} - 1\right) r/s + 1 \qquad (36)$$

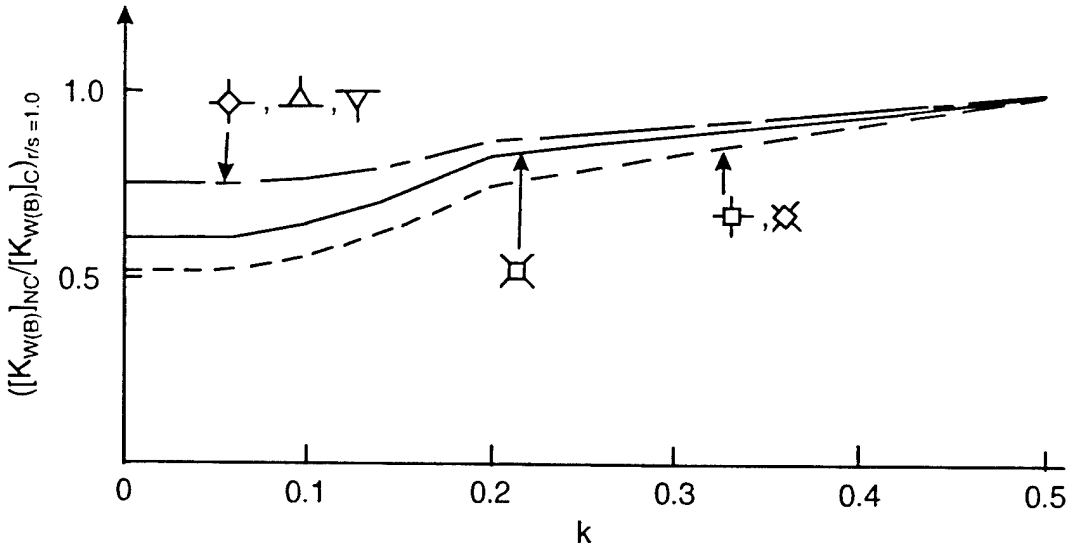

FIGURE 13. IMPACT OF SQUARE AND TRIANGLE BODY CROSS SECTIONS ON LOW MACH NUMBER VALUES OF $K_{W(B)}$ (DATA FROM REFERENCES 18 AND 29 AND BASED ON $A_{ref} = \pi W^2/4$)

Using the value of $[K_{W(B)}]_{NC}$ computed from Equation (36) for a given r/s, the nonlinear models of References 13 and 32 are once again used to relate the wing-body aerodynamics as a function of AOA and Mach number. Equations (27) through (30) are used for the other interference terms, in analogy to the elliptical cross-section case.

2.7 WING-BODY-TAIL CONFIGURATIONS

Wings and tails will be assumed to be in line at either roll positions of $\Phi = 0$ or 45 deg. This will allow the new wing-tail interference model developed and discussed in Reference 32 to be used. While this model will probably be impacted by noncircular shapes, it is believed that it is probably less of an impact than on either $K_{W(B)}$ or $K_{B(W)}$. As a result of this assumption, the tail can be analyzed just as the wing, for the body cross section of interest at the tail. The only difference will be the addition of the downwash effect on the tail produced by the wing.

2.8 VARIABLE BODY CROSS-SECTIONAL SHAPES

The discussion in the analysis section to this point has assumed a constant noncircular body cross-sectional shape. That is, the nose, afterbody and boattail or flare all have the same cross-sectional shape. These shapes could be circular, elliptical, square or triangular and oriented as shown in Figure 9. In principal, the methodology for noncircular shaped missile configurations discussed

in sections 2.2 through 2.7 for constant cross-sectional shape can be applied to configurations which have a variable cross section. To do this will require different values of the parameters $(C_n/C_{n_O})_{SB}$, $(C_n/C_{n_O})_N$, NF and interference factors for each of the different cross-sectional shapes. From a practical standpoint, only two different cross-sectional shapes will be allowed with a transition region between. For example, if the front of the missile were circular and the back elliptical, a transition region between circular and elliptical shape is necessary from a practical standpoint. Figure 14 illustrates a variable cross-section elliptical shape which was taken from Jorgensen.[6] The front or nose of the missile consists of an ellipse of a/b = 0.5 and the rear, an ellipse of a/b = 2.0, when viewed from the top or planform view. It is necessary, therefore, to have a region that smoothly contours the nose ellipse to that of the afterbody. The cross-section area of this configuration remains constant from the end of the nose to the end of the body. This also means the equivalent diameter of a circular cross section also remains constant. However, the noncircular slender body and Newtonian factors are significantly different, which means the normal force, pitching moment and center of pressure will change substantially.

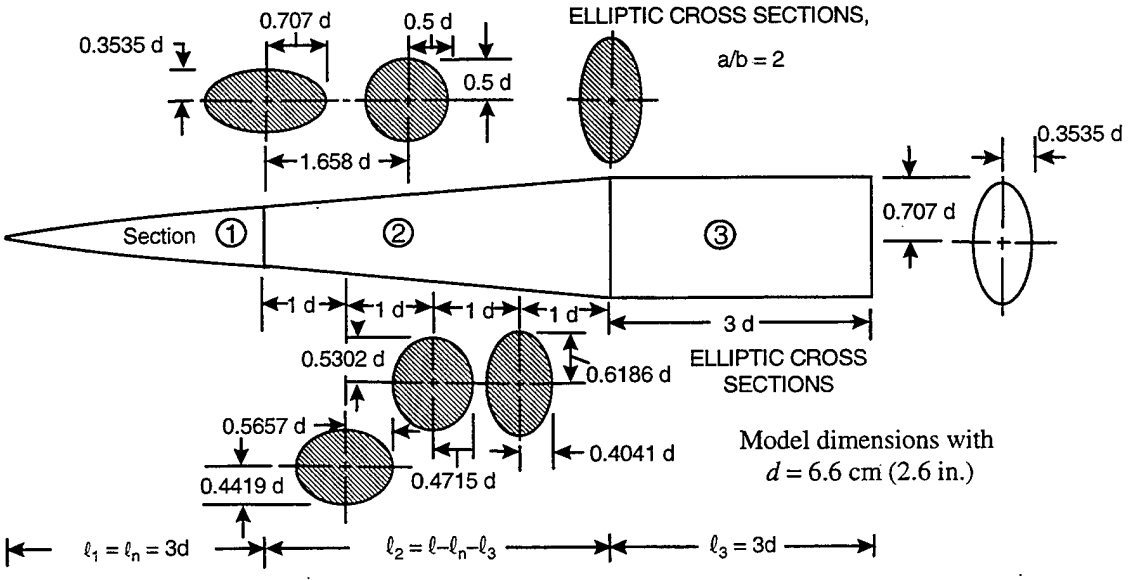

FIGURE 14. ILLUSTRATION OF A CONFIGURATION WITH A VARIABLE, NONCIRCULAR, CROSS-SECTIONAL SHAPE: TOP OR PLANFORM VIEW (FROM REFERENCE 6)

Assuming the nose of the Figure 14 has a constant cross-sectional shape, the afterbody has a length of constant cross-sectional shape of length ℓ_3 (which is equal to the boattail or flare length if a boattail or flare is present), then the normal force, pitching moment and center of pressure for the representative body alone configuration of Figure 14 can be written as

$$C_N = \sum_{i=1}^{3} \left\{ \left[\left(\frac{C_n}{C_{n_O}} \right)_{SB} C_{N_L} \right]_i + \left[\left(\frac{C_n}{C_{n_O}} \right)_N (NF)\, C_{N_{NL}} \right]_i \right\} \tag{37}$$

$$C_M = \sum_{i=1}^{3} \left\{ \left[\left(\frac{C_n}{C_{n_O}} \right)_{SB} C_{N_L} (x_m - x_{CP}) \right]_i \right.$$

$$\left. + \left[\left(\frac{C_n}{C_{n_O}} \right)_N (NF)\, C_{N_{NL}} (x_m - x_{CP}) \right]_i \right\} \tag{38}$$

$$x_{CP} = - \frac{C_M}{C_N} \tag{39}$$

In Equations (37) and (38), each section of the body is assumed to have its individual linear and nonlinear component of normal force and likewise to have its individual center of pressure relative to some desired reference location, x_m. x_{CP} and x_M of Equation (39) are in dimensions of body diameters or calibers. The local values of $(C_n/C_{n_O})_{SB}$ and $(C_n/C_{n_O})_N$ for sections 1 and 3 are known from Figures 2 through 4, and NF, from Figures 5 through 7. The values of these parameters for Section 2 are assumed to be the average of those for Sections 1 and 3 for this case. Equations (37) through (39) thus allow some approximate accounting for the variation of body cross-sectional shape along its length.

2.9 SUMMARY OF COMPUTATIONAL PROCEDURE

The method chosen to compute aerodynamics on configurations of noncircular cross-sectional shapes extends the method of Jorgensen[6] for the body alone, uses the approach of Nelson[33] and Est et al.,[34] to correct $K_{W(B)}$ at low AOA, and uses the methods of References 13 and 32 to include nonlinearities in all the interference terms. No changes in the parameters $k_{W(B)}$ and $C_{N_{T(V)}}$ computed by References 13 and 32 for circular shapes have been made for noncircular shapes. $K_{B(W)}$ and $k_{B(W)}$ are assumed to vary in a similar fashion to $K_{W(B)}$ with respect to body cross-sectional shape.

To compute the aerodynamics on a noncircular shape, the procedure outlined below is recommended.

1. Obtain the cross-sectional area distribution as a function of length. This may be available from a drawing if not given directly.

2. Approximate the body by one which is consistent with the logic of the aeroprediction code. This code requires a nose, afterbody and boattail/flare. The afterbody and boattail/flare length can be close to zero if the configuration is only a nose shape. If the configuration is a nose-afterbody with no boattail/flare, then the boattail/flare length can be zero.

3. Determine if the noncircular cross-sectional shape is the same or approximately the same. If it is, then pick an option from Figure 9 that most closely represents the cross section and roll position of interest.

4. Based on this cross-sectional shape and the cross-sectional area distribution from 1, a circular body of diameter d_{eq} is formed of given nose, afterbody and boattail/flare length. Factors $(C_n/C_{n_Q})_{SB}$, $(C_n/C_{n_Q})_N$ and NF are computed for the shape of interest. R_{N_C} and M_{N_C} are also defined for a given circular shape.

5. If fins are present, interference factors are computed for the cross section and fin orientation of interest at $\alpha = 0$, based on a body of diameter d_{eq}. These aerodynamics are combined with the equivalent body aerodynamics by multiplying the wing-body contributions by a slender body theory scaling factor.

6. Total nonlinear aerodynamics for the equivalent axisymmetric body are computed based on Reference 13 for fins at $\Phi = 0$ and Reference 32 for $\Phi = 45$ deg roll.

7. Total configuration aerodynamics are then computed using the circular body computations from 6 in conjunction with the noncircular body information from 4 and 5.

8. If the configuration has a variable noncircular cross-section shape, then the length ℓ_3 must be defined since it is assumed $\ell_1 = \ell_n$. Also if a boattail/flare is present, ℓ_3 is assumed to be the boattail or flare length. Choose two cross-sectional shapes from Figure 9 to represent ℓ_1 and ℓ_3. Instructions 4 through 7 are then repeated for the variable cross-sectional shape.

3.0 RESULTS AND DISCUSSION

The performance of the new nonaxisymmetric methodology was evaluated by applying it to an extensive array of aerodynamic configurations, including two which were outside the range of the data base used in the development process. Before moving on to consider specific examples, some time may be saved by discussing up front how the question of subcritical versus supercritical flow, previously mentioned in Section 2.5, was handled. First, a word about the actual input parameters that are used in AP98. The critical Reynolds number input is basically treated as the value for a circular cylinder, which is then adjusted internally in the code to get the critical Reynolds number for a particular noncircular cross section. Thus, when it is mentioned that a particular value for R_{N_C} is used for a given computation, it means that this number is used in the actual input file, but it is then modified by the code depending on the body cross section being modeled. Only in the case of a circular cylinder will this be the actual value used to determine the status of the flow. For the critical crossflow Mach number, M_{N_C}, the value that will be specified as an input in the following discussions will actually be an increment to the default values of the "drag bucket" boundaries. For example, by default, the critical flow region starts at a crossflow Mach number of 0.1 and ends at a crossflow Mach number of 0.54. If a value of -0.1 is specified for the critical crossflow Mach number input (which will be identified as ΔM_{N_C}), then the range of the supercritical flow region is shifted to fall between crossflow Mach numbers of 0.0 and 0.44. Note that M_{N_C} is adjusted by shifting the location of the drag bucket to higher or lower crossflow Mach numbers and not by changing the width of the bucket. Thus, it is possible that a best fit to data may be obtained by actually having the initial dip in the curve occur at a negative crossflow Mach number in instances where supercritical flow occurs very near $M_{N_C} = 0$ and the drag bucket is relatively narrow.

If a particular experimental data set included results for a circular body, the two parameters, R_{N_C} and ΔM_{N_C}, were adjusted for a "best fit" to this case and then kept constant for all noncircular computations. If no circular body information was available for a given data set, these two parameters were adjusted to give optimum agreement with the noncircular data. In the latter case, it could certainly be argued that a portion of this adjustment could actually be a correction for nonaxisymmetric geometry effects and not strictly for supercritical-subcritical flow. While it is recognized that this could be true, it also seems legitimate and even necessary to adjust these parameters to account for wind tunnel and model variations. With a more extensive data base, it might be possible to make these corrections with a higher degree of confidence. Fortunately, as explained previously in Section 2.5, given a moderately high Mach number, the issue is no longer of such great importance. In addition, for body cross sections with sharp corners, the transition Reynolds number becomes high enough so that supercritical flow is very difficult to establish, and so the uncertainty is largely removed for configurations of this type.

If one is computing aerodynamics on a noncircular cross section shape for which no experimental data exist, it is recommended that one of two alternatives be exercised. The first

alternative is to use the default values of R_{N_C} and M_{N_C}, which are set in the code to 180000 and 0.1, respectively. The second alternative is to modify these values to more closely reflect the performance of a given wind tunnel if previous experience allows this to be done. At low Mach numbers, correct selection of these parameters is quite important, whereas at higher Mach numbers, it is not so critical. This point is illustrated in Figures 15A and 15B. Figure 15A gives values of normal force coefficient for a circular cylinder from Reference 36 at M = 0.6. Both subcritical and supercritical results are shown from AP98 along with the values resulting from an optimized selection of the crossflow Reynolds number parameters. Experimental values are shown for comparison purposes. As can be seen, there is a substantial difference at this Mach number between subcritical and supercritical values. In contrast, Figure 15B shows the same information for this cylinder at M = 2.0. In this instance, there is very little effect from crossflow transition.

3.1 BODY ALONE CONFIGURATIONS

The first set of validation runs was performed on the large experimental data set of Reference 7. The geometric configurations contained within this set are shown in Figure 16. Included are two circular bodies, 1.4 inches in diameter, with 3.0-caliber tangent ogive noses, and either a 7.0-caliber or 3.0-caliber cylindrical afterbody, giving l/d (length/diameter) ratios of 10 and 6. The critical Reynolds number parameters were adjusted using these bodies, and optimal settings were found to be R_{N_C} = 330000 and ΔM_{N_C} = −0.2. The noncircular bodies in the data set are squares, diamonds (squares at a 45 deg roll position), triangles, inverted triangles (triangles at a 60 deg roll position), and ellipses with axis ratios of 2:1, 1.5:1, 0.67:1 (1.5:1 at 90 deg roll), and 0.5:1 (2:1 at 90 deg roll). All bodies have the same cross sectional area as the circle, and the distribution of that area along the longitudinal axis is the same as for the circle. The squares, diamonds, triangles, and inverted triangles have very small corner radii and were assumed to have a value of k equal to 0. All noncircular bodies are identical in length to the l/d = 10 circular cylinder except for a 2:1 ellipse and a 0.5:1 ellipse, which have the same length as the l/d = 6 cylinder. Mach numbers were 1.98 and 3.88.

Figures 17A through 17C and 18A through 18C show the results of the AP98 computations for lift coefficient, lift to drag ratio, and center of pressure location (referenced to the nose tip in this and all future cases) compared to the experimental data for the l/d = 10 ellipses at M = 1.98. The circular body results are shown in each figure for reference. In most cases, the lift coefficient comparisons, found in Figures 17A and 18A, are quite good, with the computed values tending to be somewhat low at the higher angles of attack. This is especially true of the 0.67:1 and 0.5:1 axis ratio cases. Since the circular body values tend to be lower than the data in this region, this trend is not surprising. The noncircular computations rely on the circular results as a starting point and are thus influenced by their behavior. The lift to drag ratios and the center of pressure locations for the 2:1 ellipse, found in Figures 17B and 17C, respectively, are in very good agreement with experimental data. These comparisons for the 0.5:1 ellipse are found in Figures 18B and 18C. While not as good as for the 2:1 ellipse, the variations are within the accuracy limits of the code. Figures 19A through 19C show the same comparisons for the 2:1 and the 0.5:1 ellipse at M = 3.88. For the lift coefficients, found in Figure 19A, the 0.5:1 ellipse compares with data well, but the 2:1 ellipse tends to be high at α = 10 and above. As can be seen from the circular body results shown on the same plot, this is to some degree a carryover effect. The lift to drag ratios and the center of pressure

comparisons are shown in Figures 19B and 19C. The lift to drag ratios are in reasonable agreement with the wind tunnel results with the greatest discrepancies coming for the 0.5:1 ellipse. The center of pressure locations agree well with experiment in all instances. Finally, results for computations of the 2:1 and 0.5:1 elliptical bodies of l/d = 6 are shown in Figure 20. In this instance, the 2:1 results are very good with the 0.5:1 values tending to be low, along with the circular body numbers.

Figure 21A through 21C show the lift coefficient, lift to drag ratio, and center of pressure comparisons for the squares and diamonds at M = 1.98. Once again, the circular body values are shown for reference. For lift coefficient, found in Figure 21A, the square results are quite good, being just a little high at the higher angles of attack. The diamond values tend to follow the same pattern as the ellipses, being low above α = 12 deg. The lift to drag ratios are shown in Figure 21B and are in very good agreement with the wind tunnel results. The center of pressure locations are presented in Figure 21C and are well within the accuracy limits of the code. The results for these cross sections at M = 3.88 are presented in Figures 22A through 22C. In this case, the lift coefficient results in Figure 22A are seen to be high for both cross sections. A comparison to the circular body results, which are also shown, indicates that they are in large part following the established trend. A look at Figure 22B shows that the code does well predicting lift to drag ratio for these conditions with the exception of a few low α instances. It should be noted that with angles of attack of 2 or 4 deg, it can be difficult to measure drag accurately in the wind tunnel, so some disagreement in this region could be attributed to experimental uncertainty. The center of pressure results, shown in Figure 22C, agree well with the experimental data.

Results for the triangles and inverted triangles at M = 1.98 are shown in Figures 23A through 23C. Overall, the lift coefficient comparisons, presented in Figure 23A, are not as good as for the other body cross sections, with most values being too low. This is partially a reflection of the circular body results, but also indicates some uncertainty in the modeling of triangles and inverted triangles because of a scarcity of data. On the other hand, the lift-to-drag and center-of-pressure results shown in Figures 23B and 23C are in very good agreement with the wind tunnel results. The M = 3.88 comparisons for these cross sections are shown in Figures 24A through 24C. Here, the lift coefficient values, found in Figure 24A, tend to be somewhat high above α = 8 deg, but this is in agreement with the circular body results. The lift-to-drag ratio comparisons in Figure 24B are fairly good, with some discrepancies at lower α, especially for the circle. As mentioned before, this situation could be attributed to the difficulty of measuring drag at low angles of attack. The center of pressure results in Figure 24C compare favorably with the wind tunnel measurements for triangles, but are slightly outside the accepted range for inverted triangles. If it is assumed that AP98 will be allowed slightly more leeway in modeling noncircular bodies, then these results are certainly acceptable.

The second set of experimental data that was used in the validation process came from Reference 36. The configurations tested were essentially identical to the circular body and the 2:1 and 0.5:1 ellipses in the first data set (see Figure 16), except for a larger circular body diameter of 2.6 inches. The length of the circular cylinder was 10 calibers, and both ellipses had this same total length. The wind tunnel tests were conducted at Mach numbers of 0.6, 0.9, 1.2, 1.5, and 2.0. The Reynolds number, based on the diameter of the circular body, was 650000 at the first two Mach numbers and 380000 at the others. R_{N_C} was held constant at 330000 for all computations. The best value of ΔM_{N_C} was found to be -0.1 at all Mach numbers except M = 0.9, where a value of 0.0 was used. The results of the AP98 computations are compared with the experimental results in Figures 25

through 29. Each figure shows the computed and experimental values of normal force coefficient for the two elliptical cross section configurations as well as for the circular body at a single Mach number. In addition, Figures 25, 27 and 29 have B and C sections which show comparisons for axial force and center of pressure location, respectively. The normal force 2:1 ellipse comparisons are, in general, quite good. Significant deviations from the experimental data, especially at the higher Mach numbers, tend to track the circular cylinder results. At the lower Mach numbers and lower angles of attack, there is some erratic behavior that is most likely related to the crossflow transition effects. The 0.5:1 ellipse comparisons are not as good. The M = 0.6 results are off the most, especially at higher angles of attack where the AP98 code significantly overpredicts the experimental values. It should be noted that the experimental results in this case behave in a rather erratic manner, actually leveling off and decreasing slightly at the highest α's. This could well be a transition effect under these conditions and the computed results could be brought into closer agreement by adjusting the transition parameters, but that would be outside the initial guidelines set forth earlier. As Mach number increases, the comparisons become better and are quite good at M = 2.0. The deviations tend to be in the direction of the circular cylinder results. The axial force results are quite good at M = 2.0, but do not match the experimental data as well at the lower Mach numbers. This is especially true for the 0.5:1 ellipse. The discrepancies could be due to difficulty in transition modeling at low Mach numbers or possibly to experimental uncertainties in measurement. The predicted center of pressure locations exhibit reasonably good agreement with wind tunnel results with some substantial deviation for the 0.5:1 ellipse. This problem is most evident at low angle of attack and low Mach number, indicating that it may be associated with transition modeling. Transition from supercritical to subcritical flow can produce significant shifts in center of pressure.

The next set of data considered was taken from Reference 29. The family of configurations tested in the wind tunnel is shown in Figure 30. There is a 12-inch-long body that can have four different cross sectional shapes. One is a circular cylinder and the other three are squares with different corner radii corresponding to k = 0.0, 0.1, and 0.2. In all cases, the body width is 2 inches. In addition, there are two different nose shapes. One is a 3-inch-long blunt nose and the other is a 4-inch-long sharp nose. These same body shapes were tested in the 45 deg roll position, which produces a diamond configuration. The Mach number for all tests was 0.31 and the Reynolds number was 1.3 million per foot. For the computations, the value of R_{N_c} was set to 285000 for all cases. ΔM_{N_c} was set to -0.1 for the blunt nose configurations and to 0.0 for the sharp nose runs. The computed and experimental normal force coefficients for the square orientation bodies with the blunt nose are shown in Figure 31A. The circular body values are also included for reference purposes. As can be seen, the AP98 results are very good at k values of 0.0 and 0.1, but tend to be somewhat high for k = 0.2 at the higher angles of attack. The same trend is observed for the diamond orientation in Figure 32A. The center of pressure predictions for the squares and diamonds are presented in Figures 31B and 32B. While most comparisons are of acceptable accuracy, there are substantial deviations from wind tunnel data for the shapes with sharper corners and for the circle at low angle of attack. Comparisons tend to improve as α increases, which indicates that transition modeling may once again be the problem. With such low Mach numbers, transition effects on center of pressure location can be quite dramatic and, unfortunately, very difficult to model. In Figure 33, the normal force coefficients for the k = 0.2 square and diamond body orientations with the sharp nose are presented. The computed square values tend to agree quite well with experiment at low α, but become somewhat high at the higher angles of attack. The diamond orientation results agree well

with the wind tunnel results at low and high α, but tend to be somewhat high in the middle of the angle of attack range. Once again, transition effects are a possible cause at these low Mach numbers.

The next data set[22] was taken on a family of configurations similar to the one above. The various components are shown in Figure 34. The diameter of the circular cross section and the width of each square cross section was assumed to be 3 inches from information given in the reference. The corner radii of squares correspond to k values of 0.0, 0.167, and 0.333. The power law nose section is 10 inches long and the body is 30 inches long. The wind tunnel tests were conducted at Mach numbers of 0.5, 0.75, 1.0, 1.25, 1.5, 1.75, and 2.0 at a constant angle of attack of 20 deg. Data was taken over an α range of 0 to 30 deg at M = 0.9. The average Reynolds number was 700000 based on the diameter. As in the previous case, wind tunnel runs were conducted for the square orientation and at 45 deg roll diamond orientation. For the computations, R_{N_C} was set to 180000 for the square roll position and to 222000 for the diamond position. ΔM_{N_C} was kept at 0.0 for all runs. The M = 0.9 normal force coefficient comparisons for the square roll orientation are shown in Figure 35. As usual, the circular body results are shown for reference. In general, the AP98 numbers compare favorably to the wind tunnel data with any significant differences tending to be on the high side. This tendency is consistent with the circular body results, which also tend to be high. Figure 36 shows the same behavior for the diamond roll configuration. Figures 37 and 38 show the α = 20 deg comparisons for the entire Mach number range for squares and diamonds, respectively. Again, in most instances, agreement between the AP98 results and the experimental values is quite good. Note in Figure 37 that the normal force for the k = 0.0 body is considerably higher than for the others. This is due to the fact that subcritical flow exists on this body while supercritical flow is present on the bodies with more rounded corners. Also note that the normal force coefficient for the circular body is slightly higher than that for the k = 0.333 body. This occurs because the equivalent area on which the coefficients are based is different for each configuration. It is smaller for the circle, which increases the coefficient enough to compensate for the fact that the actual normal force value is slightly higher for the k = 0.333 body.

The next experimental data set was taken from Reference 37. The wind tunnel models tested are shown in Figure 39. They consist of an ogive-cylinder body with a diameter of 56.2 cm and a square cross section body with a side length of 50 cm. The square was rounded to a k value of 0.1. The tests were carried out at a constant Mach number of 0.75. There was no Reynolds number given, so the input Reynolds number for the computations was selected to give supercritical flow conditions that seemed to match the experimental results fairly well. Both the square and diamond roll positions were considered. Figure 40 illustrates the normal force comparisons between AP98 and experiment for the body-alone case. The agreement is good across the board, with the exception of the diamond at higher α. Here, the data indicates that subcritical flow begins to establish itself around α = 12 deg, whereas the theory continues to show supercritical flow.

The 3:1 elliptical body of Reference 27, as illustrated in Figure 41, was considered next. It consists of a power law nose with a 3:1 elliptical cross section and no afterbody. The wind tunnel experiments were conducted at Mach numbers of 2.0, 2.5, 3.0, 4.0 and 5.0. At these Mach numbers, there are essentially no transition effects to be factored in, so the computations were performed by setting the input Reynolds number below transitional values. The resulting comparisons on normal force are shown in Figure 42 for the M = 2, 3 and 5 cases. Once again, reasonable agreement is achieved in most cases.

The final body-alone case is illustrated in Figure 14. In the roll orientation shown, it consists of a body that begins as a 0.5:1 ellipse on the nose and then transitions to a 2:1 ellipse on the afterbody. This will be referred to as the $\Phi = 90$ deg roll position. If the body is rolled 90 deg so that the nose portion is now a 2:1 ellipse and the afterbody is the 0.5:1 ellipse, then it is in the $\Phi = 0$ deg roll position. Both configurations were tested in the wind tunnel at Mach numbers of 0.6, 0.9, 1.2, 1.5, and 2.0. The Reynolds numbers, based on the equivalent diameter of the body, were 650000 for M = 0.6 and 0.9 and 380000 for M = 1.2, 1.5, and 2.0. For the AP98 computations, R_{N_C} was set to 286000 for the $\Phi = 0$ deg roll position and to 330000 for the $\Phi = 90$ deg position. ΔM_{N_C} was set to -0.1 for all runs except for the $\Phi = 90$ deg roll position at M = 0.9, where it was set to 0.0. The normal force comparisons for these two configurations are shown in Figures 43A, 44, 45A, 46 and 47A for M = 0.6, 0.9, 1.2, 1.5, and 2.0, respectively. Inspection of the figures will show that the overall agreement of AP98 with experiment is good. Predicted center of pressure locations for these two configurations are shown in Figures 43B, 45B and 47B for Mach numbers of 0.6, 1.2, and 2.0. Above 8-deg angles of attack, agreement with wind tunnel data is good except for the $\Phi = 0$ deg roll position at M = 0.6. Transition modeling effects are the most likely cause of these deviations. For an example of the center of pressure shifts that can be caused by transition from supercritical to subcritical flow, observe the shift of just over one caliber that occurs between $\alpha = 20$ deg and $\alpha = 24$ deg for the $\Phi = 0$ deg configuration in Figure 43B.

3.2 BODY-WING AND BODY-WING-TAIL CONFIGURATIONS

The first wing-body configuration to be investigated was from Reference 29 and is illustrated in Figure 30. Only the blunt-nose body was used in the fin analysis. Wind tunnel tests were conducted for bodies of all cross sections fitted with the F1 fin. Fins F2 and F3 were tested only on the square body with k = 0.2. All runs were repeated with the bodies rolled 45 deg into the diamond configuration. The fins were mounted on the corners of the body in all cases so that in the square roll position, the fins are in an "x" or cross-position; and in the diamond cases, the fins are in a "+" or plus roll position. The Mach number was a constant 0.31, and the Reynolds number was 1.3 million per foot. For the AP98 runs, R_{N_C} was set to 285000 and ΔM_{N_C} to -0.1 in all cases. The comparisons of AP98 computations for normal force coefficient with experimental data are shown in Figures 48A and 49A for square and diamond cross section bodies, respectively. The circular body results are included for reference. The F1 fin configuration was used in all instances. Agreement of AP98 with the wind tunnel data is, in general, very good. The greatest deviation for both squares and diamonds seems to occur for the k = 0.2 cases at $\alpha = 30$ deg and may be a transition effect that is not being modeled adequately. Figures 48B and 49B show the center of pressure results for squares and diamonds, respectively. Agreement with wind tunnel data is very good in all instances. Figure 50 shows the normal force comparisons for the k = 0.2 square cross section body fitted with the F2 and F3 fins. The results for the diamond bodies with these fins may be found in Figure 51. For both cross sections, the agreement with wind tunnel data is somewhat better for the F2 fin than for the F3 fin, but is of acceptable accuracy overall.

The next wing-body configuration to be considered was the one from Reference 37 illustrated in Figure 39. Both the 56.2 cm diameter circular and the 50 cm square bodies were run with the AP98. The fins were located in an x-roll position. The Mach number of the wind tunnel tests was 0.75. No Reynolds number was given; therefore, as in the body-alone computations for this

configuration, the input Reynolds number was set sufficiently high to give supercritical flow. In this instance, however, as well as in all cases involving lifting surfaces, it is assumed that supercritical flow cannot be established in the vicinity of wings or fins. An override has been added to AP98 to force subcritical flow in a two-chordlength region in the vicinity of lifting surfaces. The length is adjusted in some cases, such as for fins mounted at the extreme aft end of the body. Figure 52 shows the normal force comparisons for this configuration. As can be seen, the agreement with wind tunnel data is acceptable.

The next lifting surface cases to be run were taken from Reference 6 and are illustrated in Figure 53. Each configuration has a 2:1 elliptical body. One has a large wing mounted near mid-body and the other has the same wing but, in addition, a vertical-horizontal tail assembly mounted at the rear of the body. The wind tunnel tests were conducted at Mach numbers of 0.6 and 2.0 with corresponding Reynolds numbers, based on equivalent body diameter, of 430000 and 380000. For the AP98 computations, R_{N_C} was set to 330000 and ΔM_{N_C} to -0.1. The comparisons for the normal force coefficients for the wing-body configuration are shown for both Mach numbers in Figure 54A and for the wing-body-tail configuration in Figure 55A. In both cases, the agreement is very good. Center of pressure predictions for these two configurations are shown in Figures 54B and 55B. As for the normal force coefficients, agreement with experimental data is very good.

3.3 COMPLEX CONFIGURATIONS

Two examples of more complex shapes were selected for validation purposes to see how well their aerodynamic characteristics could be approximated by the simple shapes included within the data base used to calibrate the methodology. The first of these is shown in Figure 56. It is a waverider designed to operate at Mach 14 and consists of a near-triangular shaped lifting body.[38] Its overall length is 39 inches and its span is 16.2 inches. The base height is 6.84 inches. The Reynolds number for the wind tunnel tests was 2 million per foot. At this high Mach number, there is no issue of subcritical versus supercritical flow, since by $\alpha = 2.5$ deg, the crossflow Mach number is already beyond the region of the drag bucket. The computed and experimental values of lift coefficients are shown in Figure 57A. Note that these lift coefficient values are based on the planform area of the body (375 in.^{2}). The agreement is very good, indicating that the new methodology may indeed be applied to configurations that are reasonable approximations to the basic geometric shapes included within AP98. Comparisons for axial force coefficients and pitching moment coefficients are presented in Figures 57B and 57C. Agreement with wind tunnel data is quite good considering the approximations made in modeling the geometry.

The final configuration considered is shown in Figure 58. It consists of a lifting body with variable sweep wing panels. In this case, we have a body that appears at first glance to be an inverted triangle, but the lower angle is only 45 deg and not 60 deg. In this sense, it resembles the lower half of a diamond. For comparison purposes, it was decided to run this example as both an inverted triangle and a diamond, both with sharp corners since the top corners were thought to be more influential on the flow field. The wing panels were modeled at a 40 deg leading edge sweep. Computations were performed for Mach numbers of 0.4, 0.6, and 0.8 with corresponding Reynolds numbers, based on the maximum body chord of 5.04 million, 7.2 million, and 9.36 million, respectively. R_{N_C} was a constant 330000 for all runs. ΔM_{N_C} was adjusted as follows. For the

diamond it was 0.08 at M = 0.4 and 0.17 for M = 0.6 and M = 0.8. For the inverted triangle, it was 0.11 at M = 0.4, 0.21 at M = 0.6, and 0.26 at M = 0.8. The lift coefficients for the wind tunnel tests and the AP98 computations for both body shapes are shown for the three Mach numbers in Figures 59 through 61. The coefficient values shown are based on the planform area of the body (96.2 $in.^{-2}$). On balance, both approaches give acceptable results, with the diamond being somewhat better in most cases. The diamond may give these good results because it more closely represents the true angle on the body's lower surface, and it is the windward side aerodynamics that dominate the flow field.

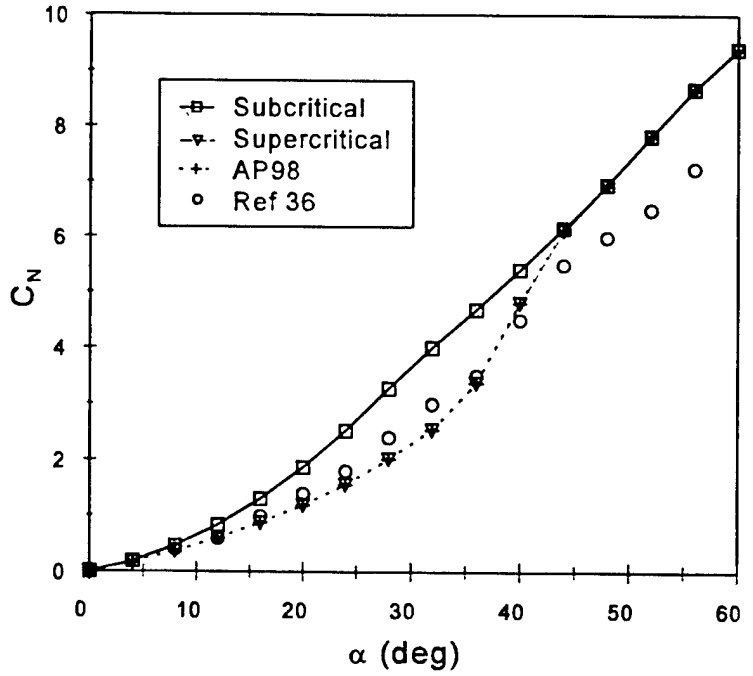

FIGURE 15A. SUBCRITICAL AND SUPERCRITICAL NORMAL FORCE COEFFICIENTS FOR A LOW MACH NUMBER FLOW (M_∞ = 0.6)

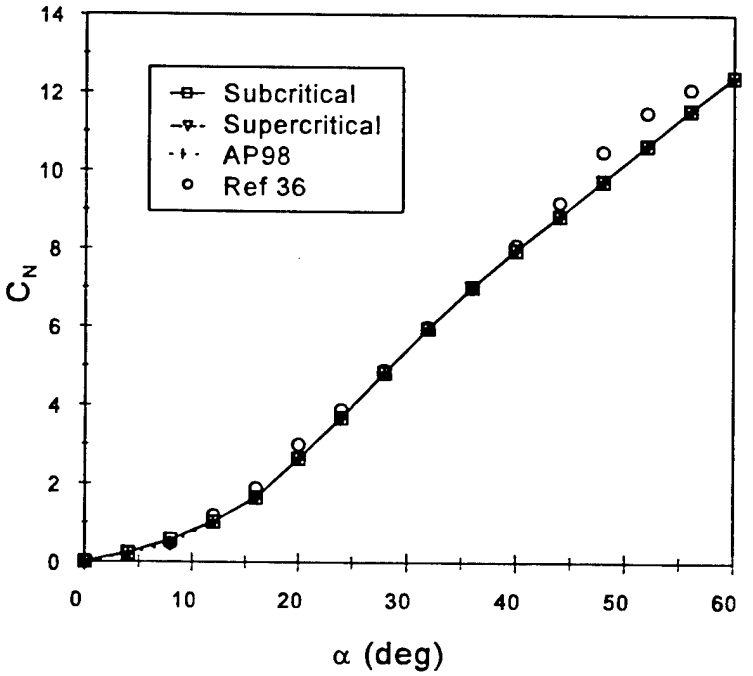

FIGURE 15B. SUBCRITICAL AND SUPERCRITICAL NORMAL FORCE COEFFICIENTS FOR A HIGH MACH NUMBER FLOW (M_∞ = 2.0)

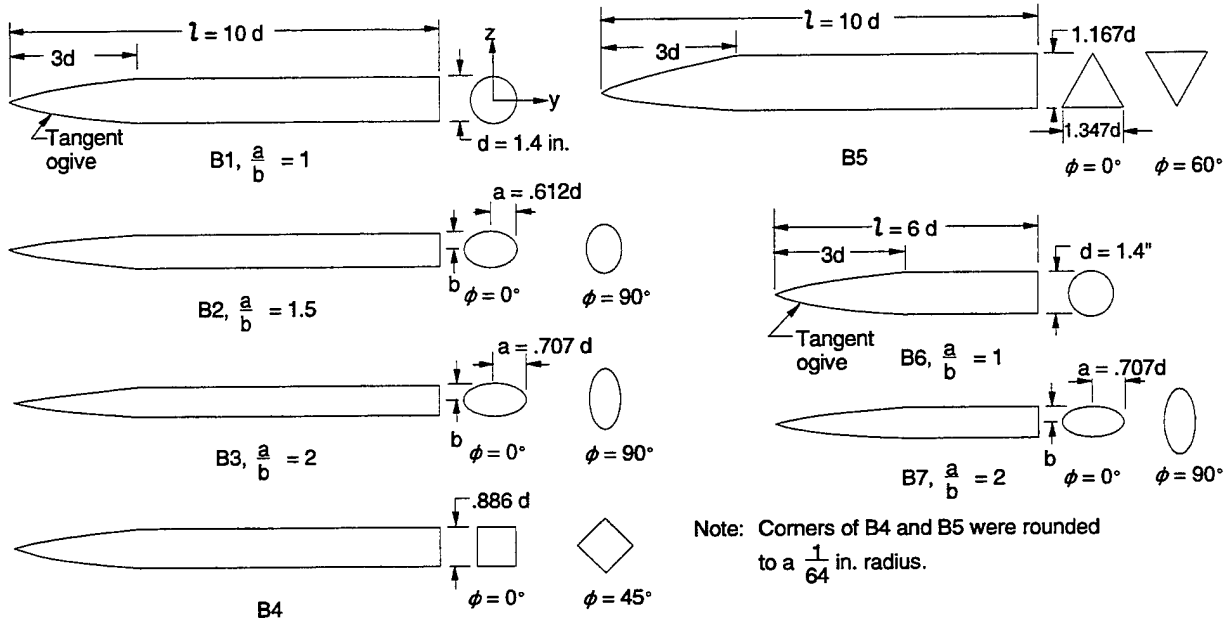

FIGURE 16. BODY ALONE CONFIGURATIONS[7] WITH ELLIPTICAL, SQUARE, DIAMOND, TRIANGULAR, AND INVERTED TRIANGULAR SHAPES

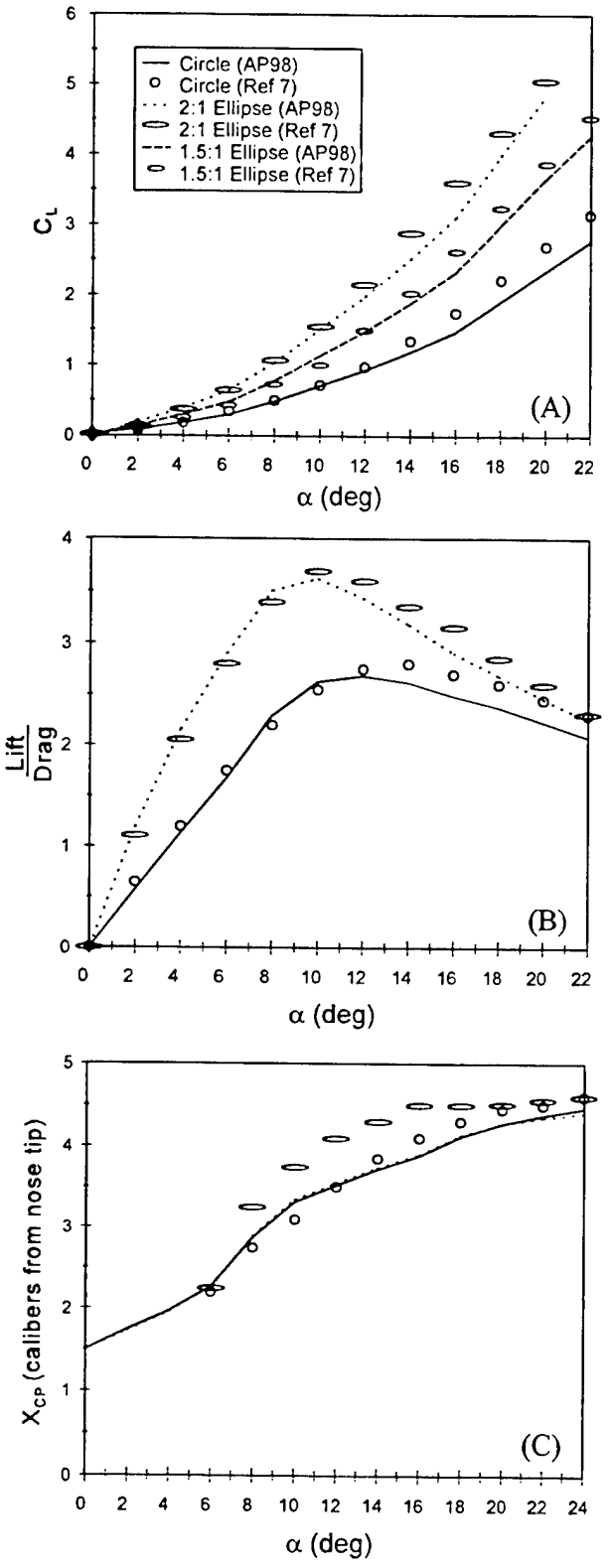

FIGURE 17. AERODYNAMIC DATA OF 2:1 AND 1.5:1 ELLIPSES OF FIGURE 16 COMPARED TO CIRCULAR BODY AT M = 1.98 (L/D = 10): (A) LIFT COEFFICIENT, (B) LIFT TO DRAG RATIO, (C) CENTER OF PRESSURE

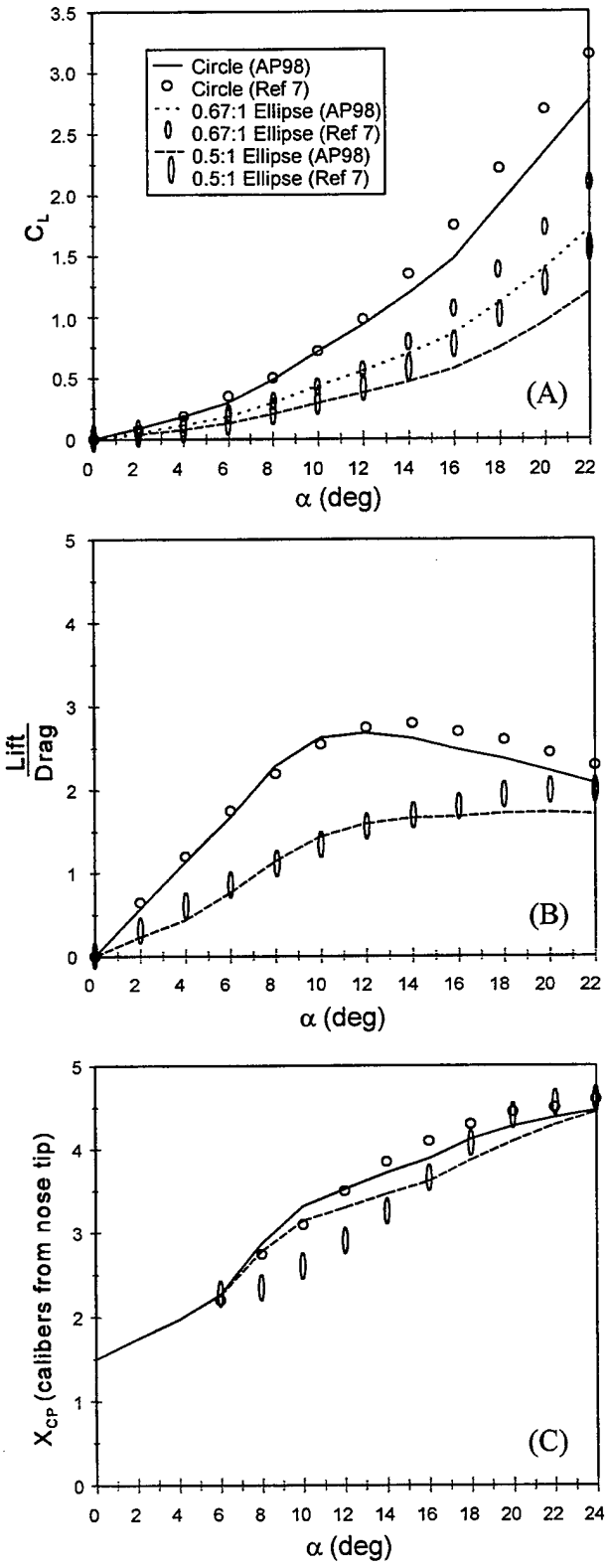

FIGURE 18. AERODYNAMIC DATA OF 0.67:1 AND 0.5:1 ELLIPSES OF FIGURE 16 COMPARED TO CIRCULAR BODY AT M = 1.98 (L/D = 10): (A) LIFT COEFFICIENT, (B) LIFT TO DRAG RATIO, (C) CENTER OF PRESSURE

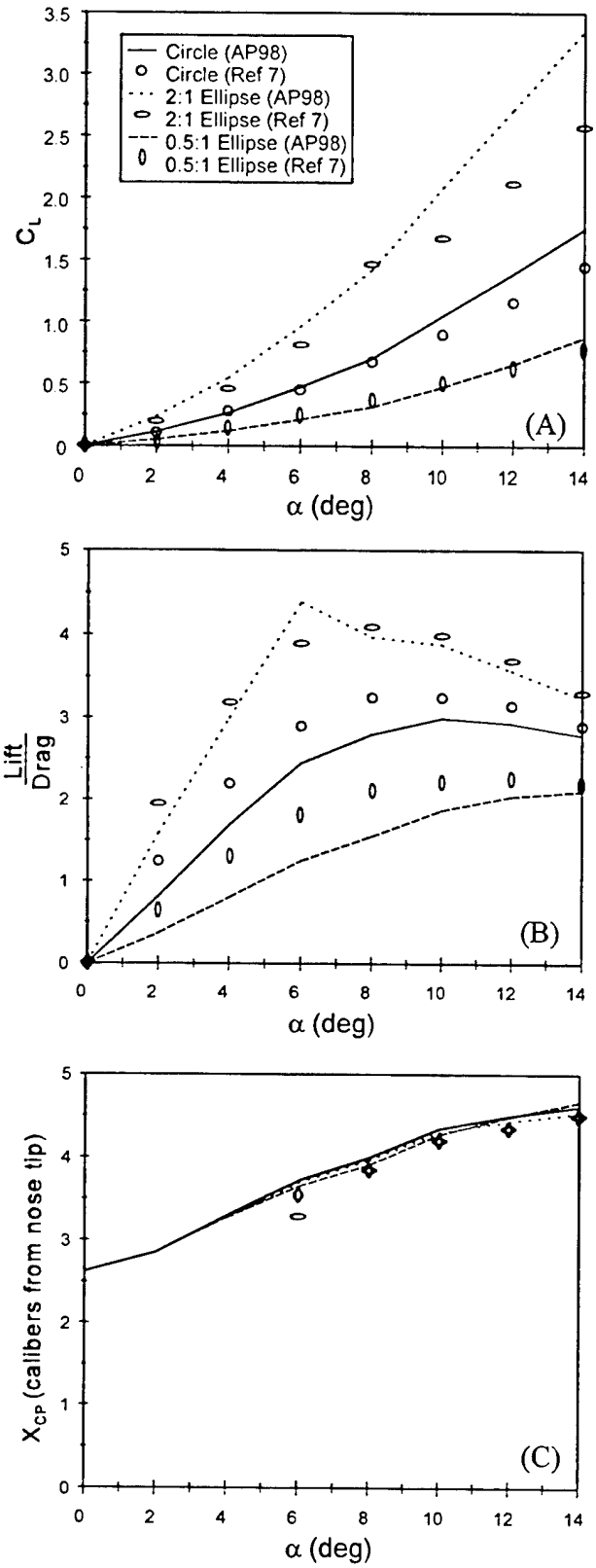

FIGURE 19. AERODYNAMIC DATA OF 2:1 AND 0.5:1 ELLIPSES OF FIGURE 16 COMPARED TO CIRCULAR BODY AT M = 3.88 (L/D = 10): (A) LIFT COEFFICIENT, (B) LIFT TO DRAG RATIO, (C) CENTER OF PRESSURE

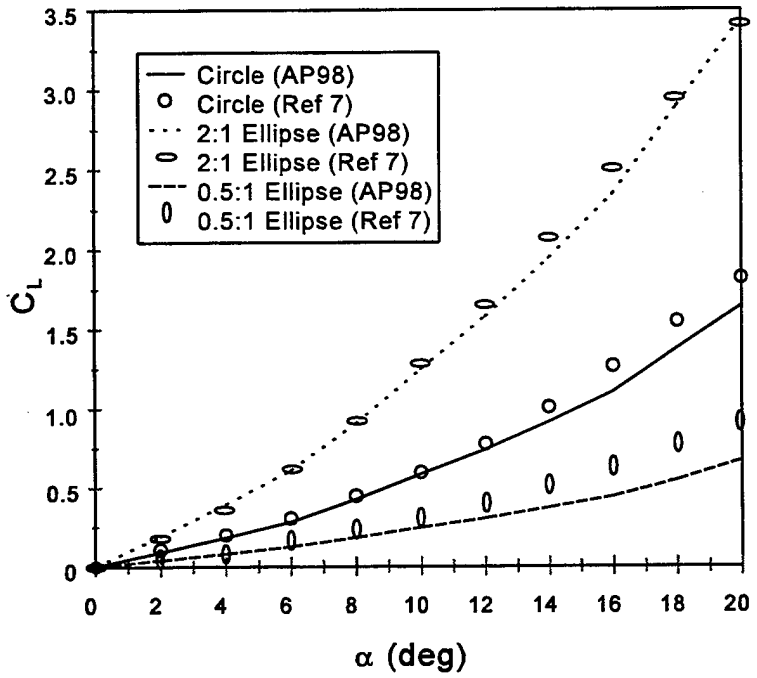

FIGURE 20. LIFT COEFFICIENTS OF 2:1 AND 0.5:1 ELLIPSES OF FIGURE 16 COMPARED TO CIRCULAR BODY AT M = 1.98 (L/D = 6)

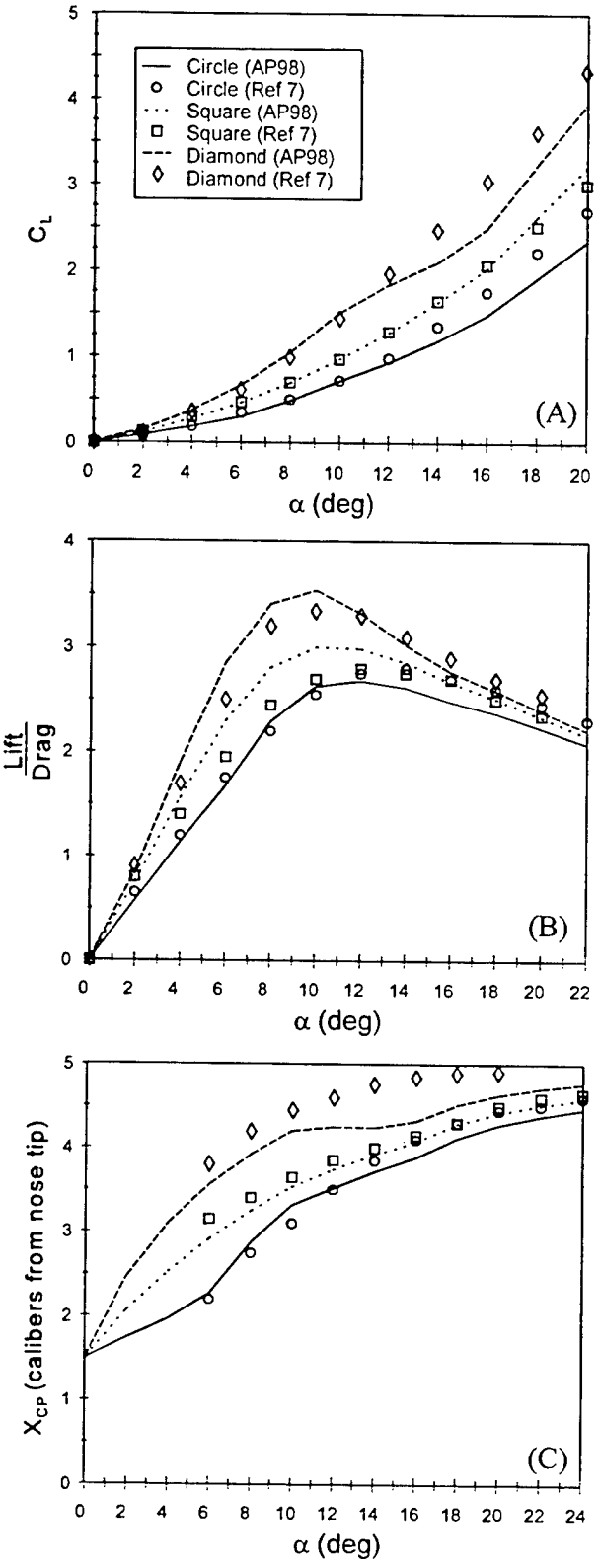

FIGURE 21. AERODYNAMIC DATA OF SQUARES (k = 0.0) AND DIAMONDS (k = 0.0) OF FIGURE 16 COMPARED TO CIRCULAR BODY AT M = 1.98 (L/D = 10): (A) LIFT COEFFICIENT, (B) LIFT TO DRAG RATIO, (C) CENTER OF PRESSURE

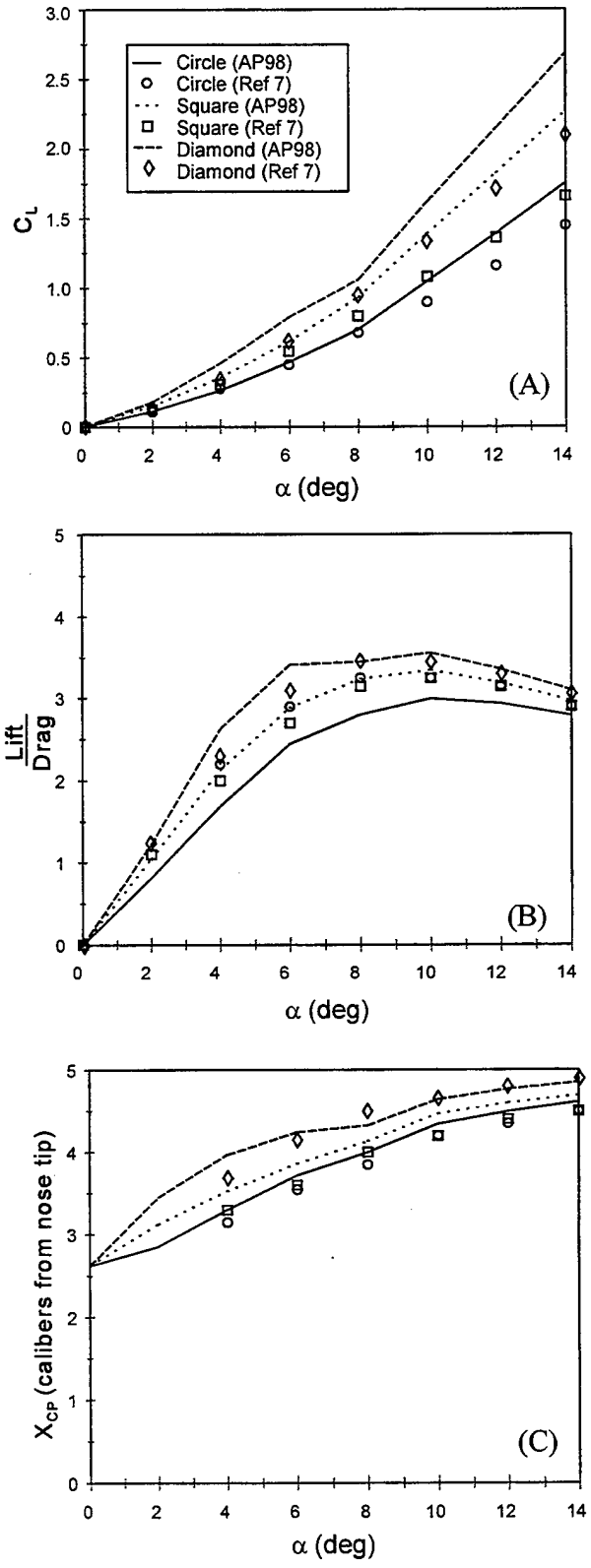

FIGURE 22. AERODYNAMIC DATA OF SQUARES (k = 0.0) AND DIAMONDS (k = 0.0) OF FIGURE 16 COMPARED TO CIRCULAR BODY AT M = 3.88 (L/D = 10): (A) LIFT COEFFICIENT, (B) LIFT TO DRAG RATIO, (C) CENTER OF PRESSURE

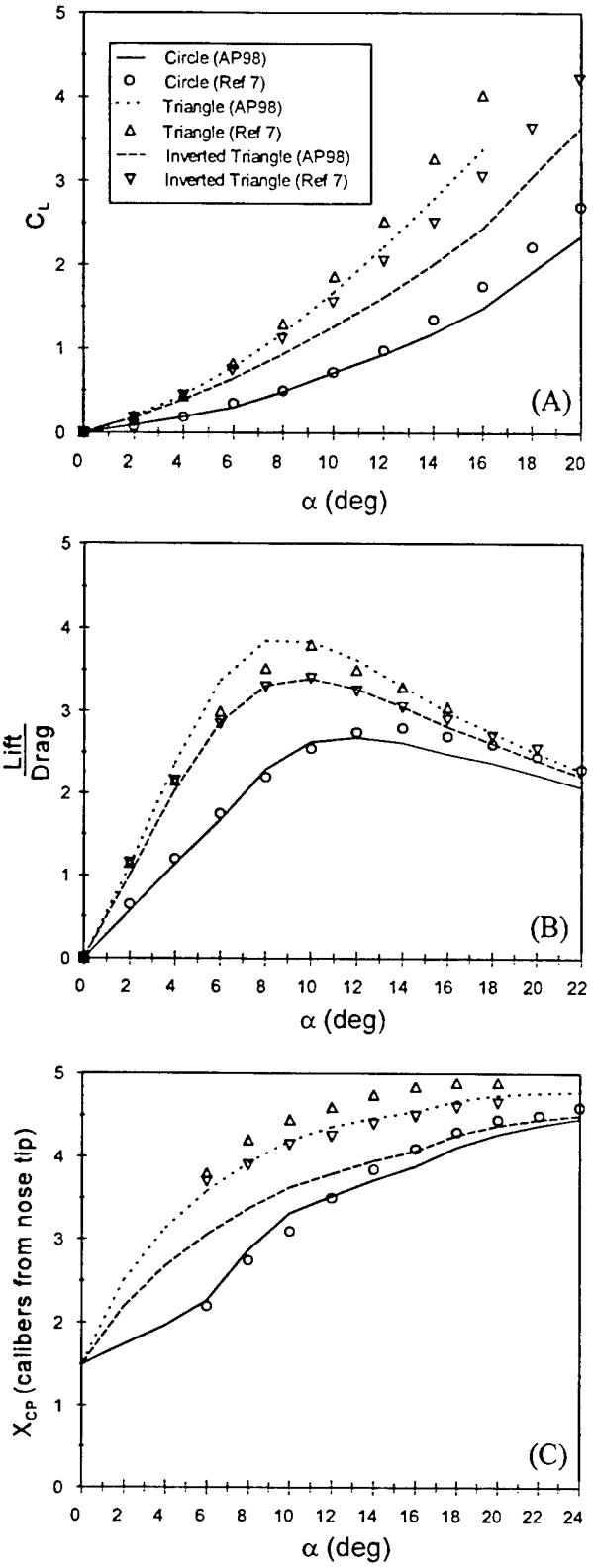

FIGURE 23. AERODYNAMIC DATA OF TRIANGLES (k = 0.0) AND INVERTED TRIANGLES (k = 0.0) OF FIGURE 16 COMPARED TO CIRCULAR BODY AT M = 1.98 (L/D = 10): (A) LIFT COEFFICIENT, (B) LIFT TO DRAG RATIO, (C) CENTER OF PRESSURE

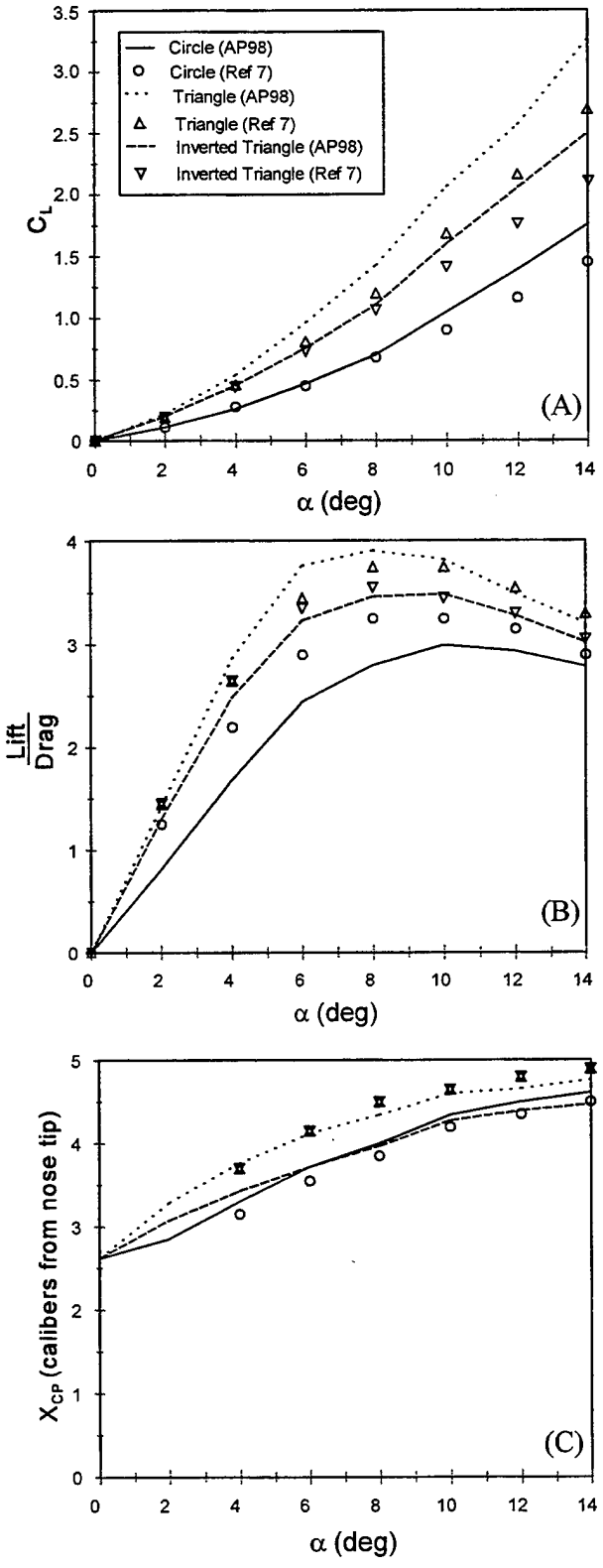

FIGURE 24. AERODYNAMIC DATA OF TRIANGLES (k = 0.0) AND INVERTED TRIANGLES (k = 0.0) OF FIGURE 16 COMPARED TO CIRCULAR BODY AT M = 3.88 (L/D = 10): (A) LIFT COEFFICIENT, (B) LIFT TO DRAG RATIO, (C) CENTER OF PRESSURE

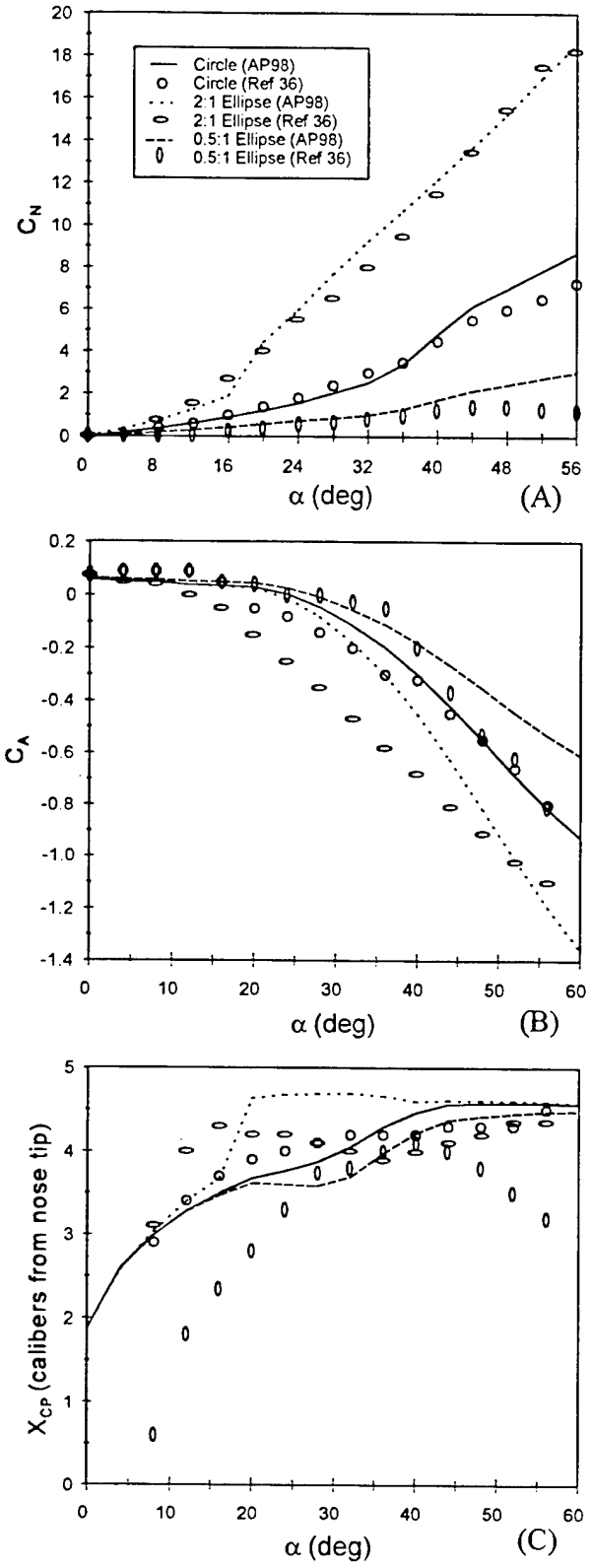

FIGURE 25. AERODYNAMIC DATA FOR 2:1 AND 0.5:1 ELLIPSES OF FIGURE 16 COMPARED TO CIRCULAR BODY AT M = 0.6: (A) NORMAL FORCE COEFFICIENT, (B) AXIAL FORCE COEFFICIENT, (C) CENTER OF PRESSURE

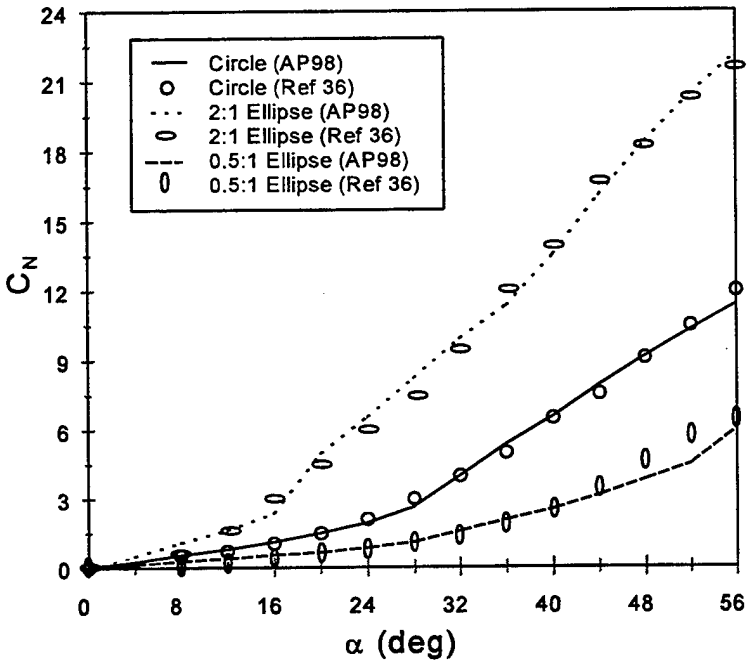

FIGURE 26. NORMAL FORCE COEFFICIENTS FOR 2:1 AND 0.5:1 ELLIPSES OF FIGURE 16 COMPARED TO CIRCULAR BODY AT M = 0.9

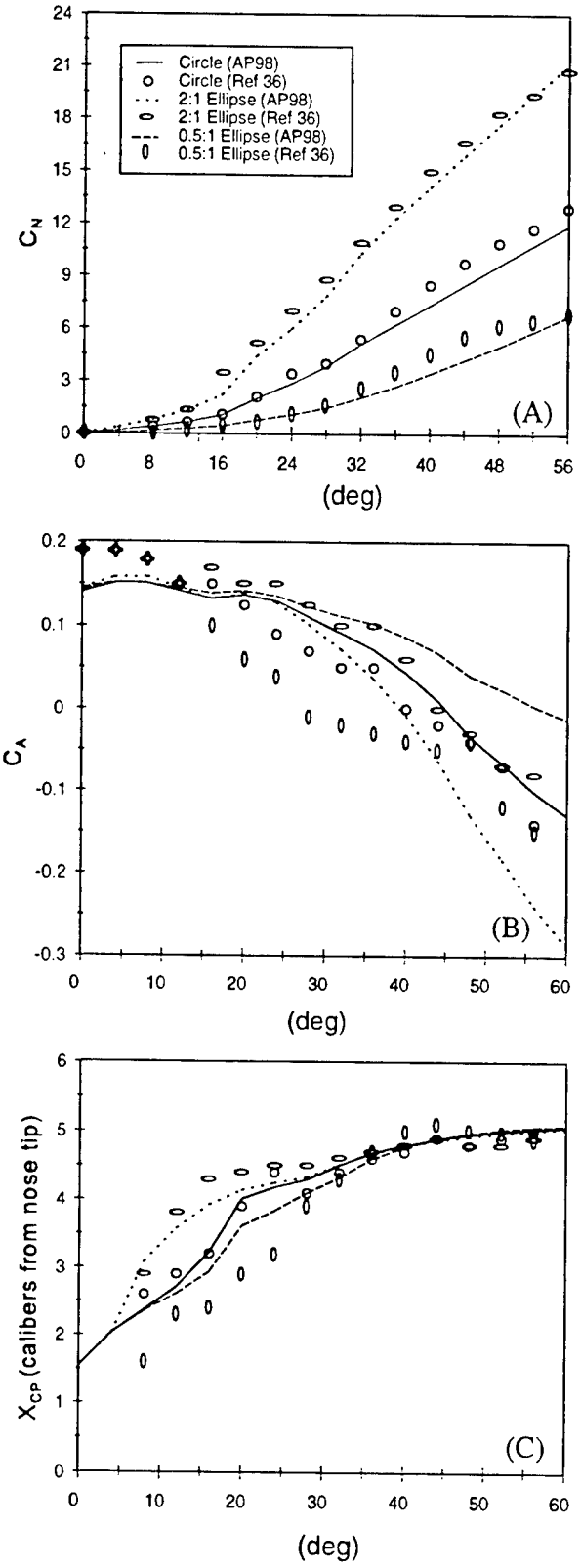

FIGURE 27. AERODYNAMIC DATA FOR 2:1 AND 0.5:1 ELLIPSES OF FIGURE 16 COMPARED TO CIRCULAR BODY AT M = 1.2: (A) NORMAL FORCE COEFFICIENT, (B) AXIAL FORCE COEFFICIENT, (C) CENTER OF PRESSURE

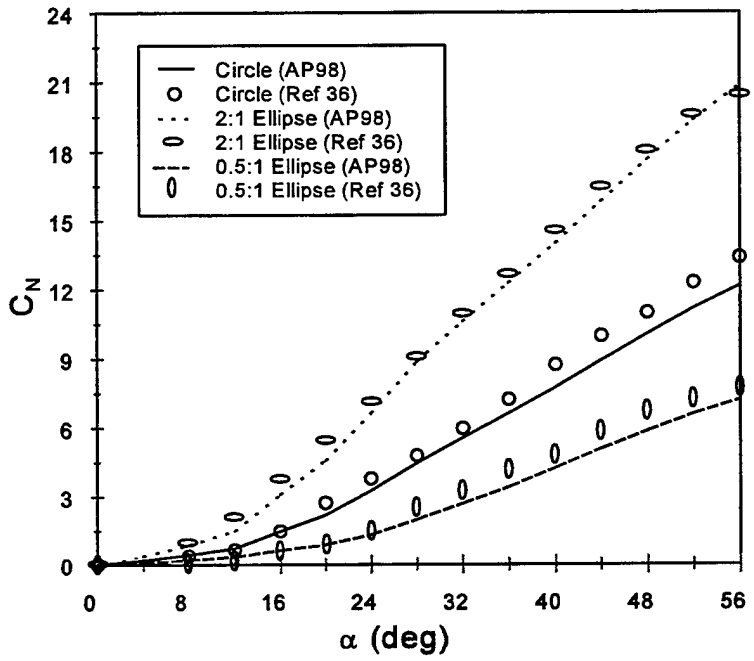

FIGURE 28. NORMAL FORCE COEFFICIENTS FOR 2:1 AND 0.5:1 ELLIPSES OF FIGURE 16 COMPARED TO CIRCULAR BODY AT M = 1.5

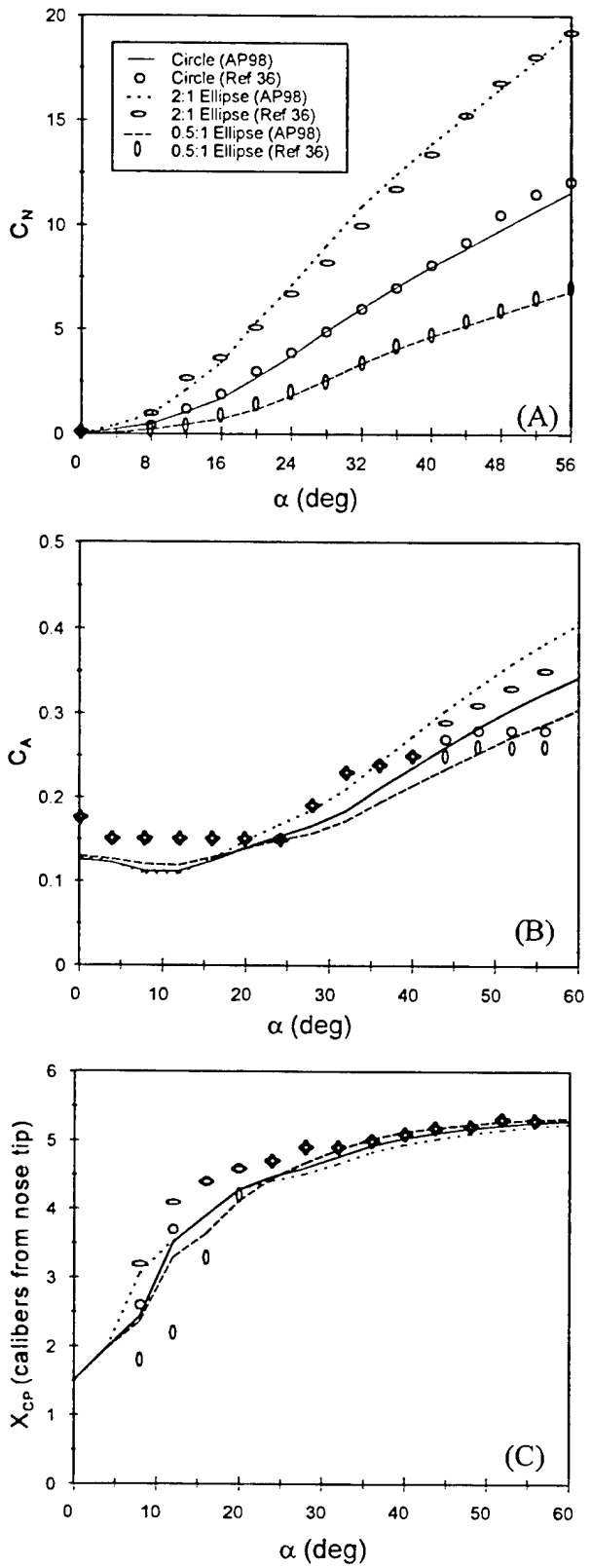

FIGURE 29. AERODYNAMIC DATA FOR 2:1 AND 0.5:1 ELLIPSES OF FIGURE 16 COMPARED TO CIRCULAR BODY AT M = 2.0: (A) NORMAL FORCE COEFFICIENT, (B) AXIAL FORCE COEFFICIENT, (C) CENTER OF PRESSURE

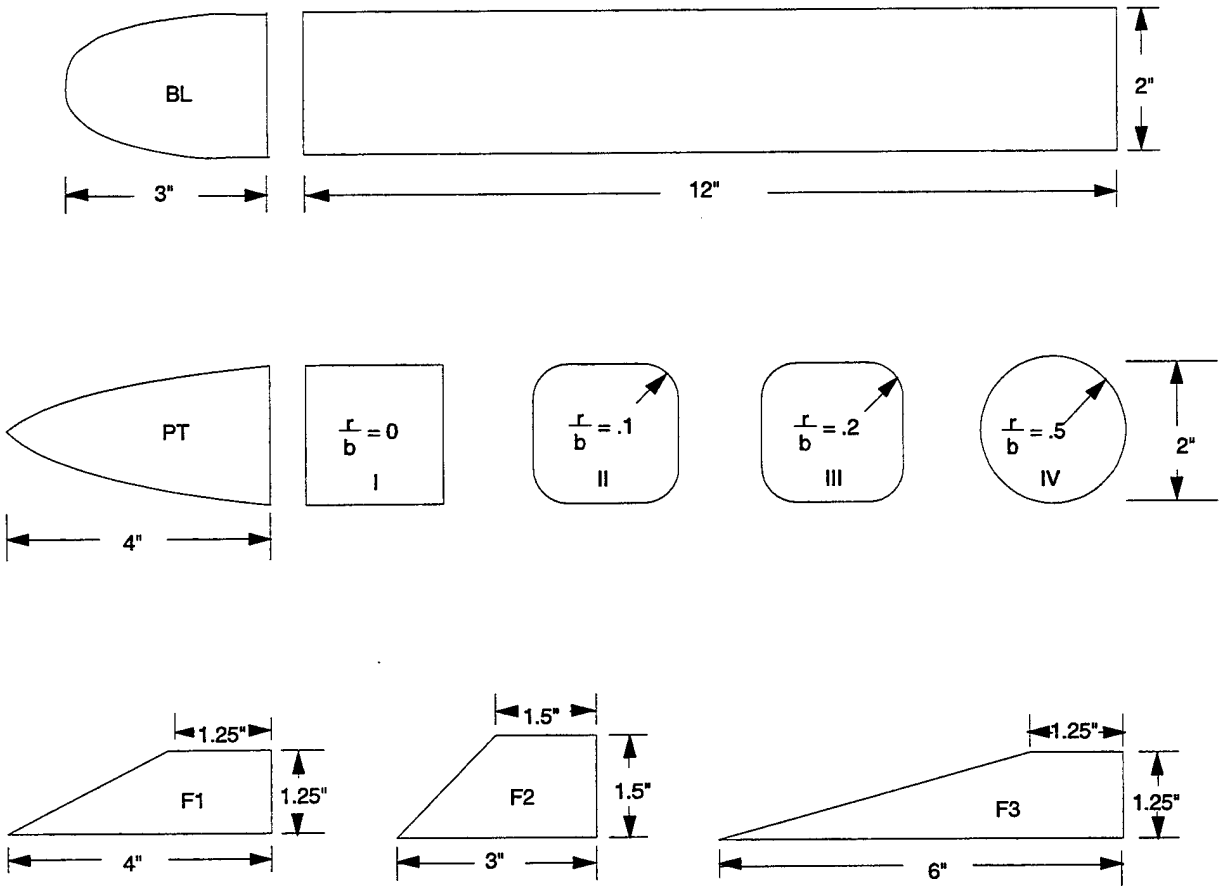

FIGURE 30. COMPONENTS OF BODY ALONE AND WING-BODY CONFIGURATIONS[29] WITH SQUARE CROSS SECTIONS OF VARYING CORNER RADII

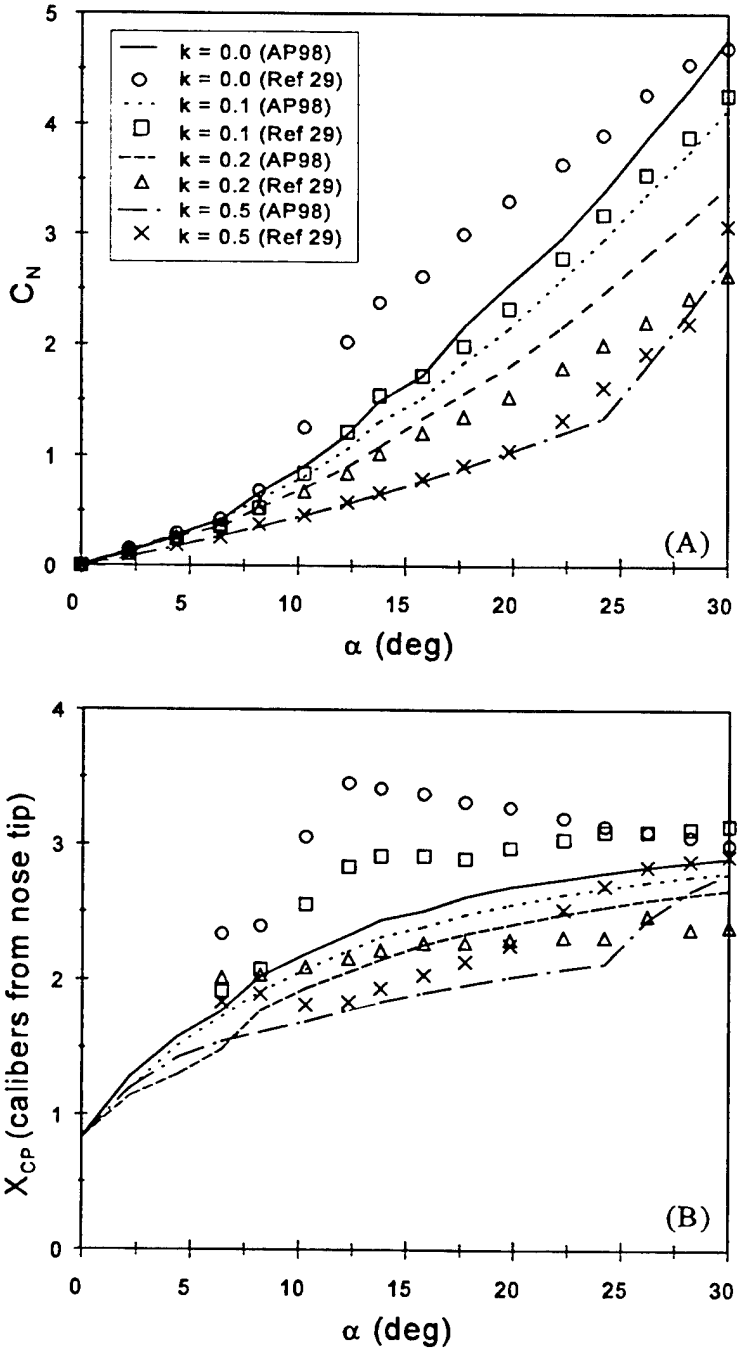

FIGURE 31. AERODYNAMIC DATA FOR SQUARE BODIES OF FIGURE 30 WITH DIFFERENT CORNER RADII AT M = 0.31: (A) NORMAL FORCE COEFFICIENT, (B) CENTER OF PRESSURE

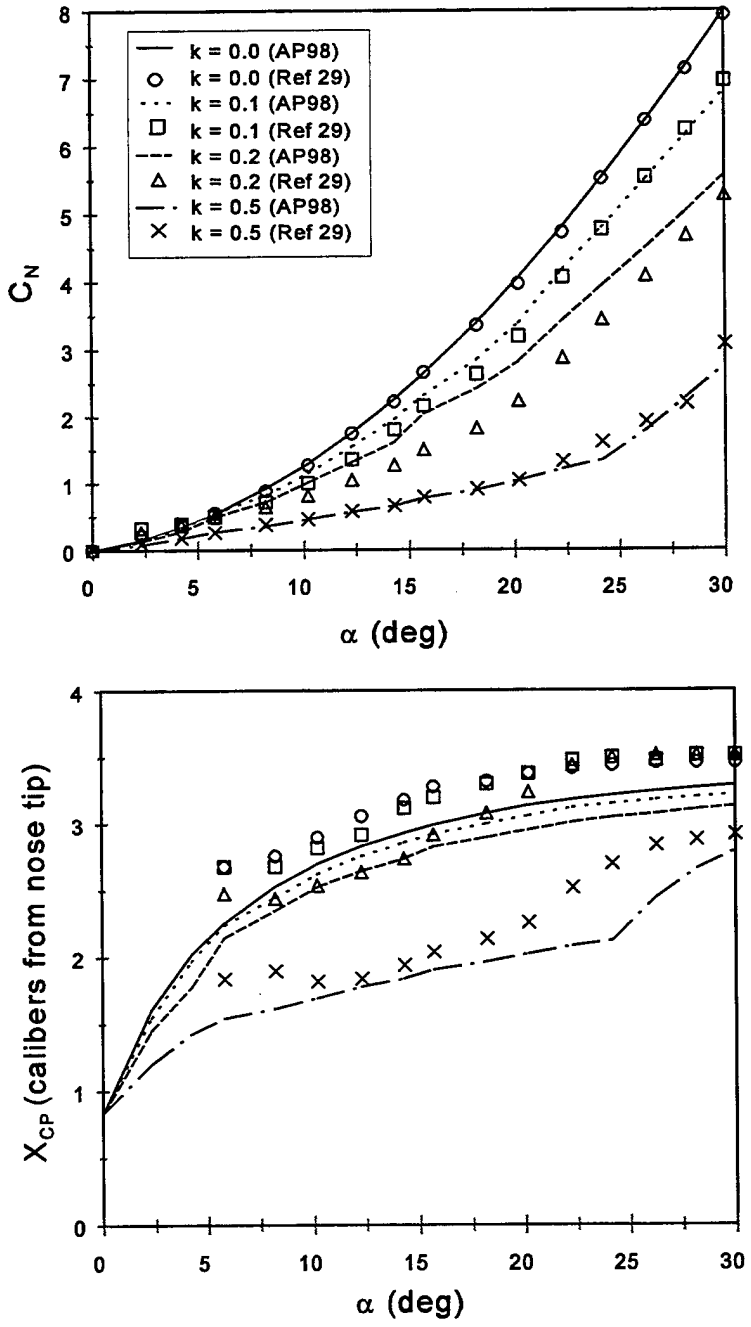

FIGURE 32. AERODYNAMIC DATA FOR DIAMOND BODIES OF FIGURE 30 WITH DIFFERENT CORNER RADII AT M = 0.31: (A) NORMAL FORCE COEFFICIENT, (B) CENTER OF PRESSURE

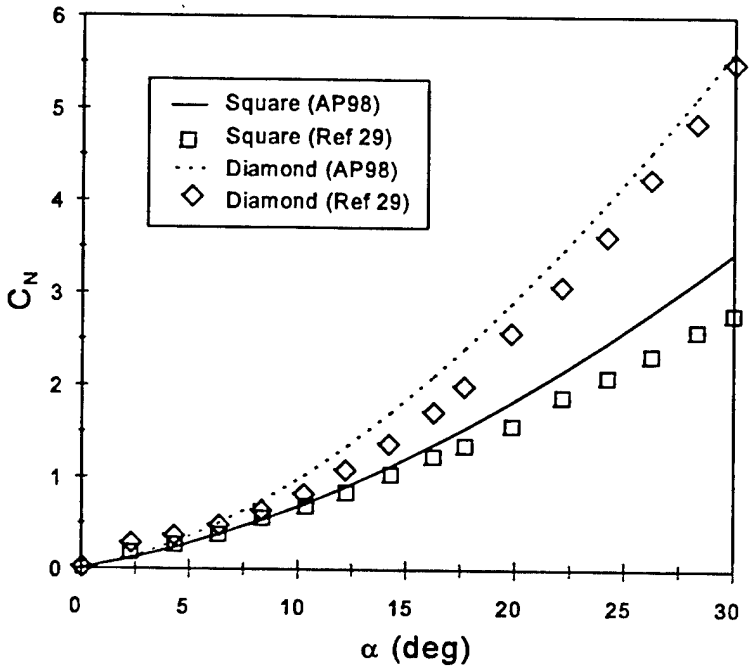

FIGURE 33. NORMAL FORCE COEFFICIENTS FOR SQUARE AND DIAMOND CROSS SECTION BODIES (k = 0.2) OF FIGURE 30 WITH SHARP NOSES AT M = 0.31

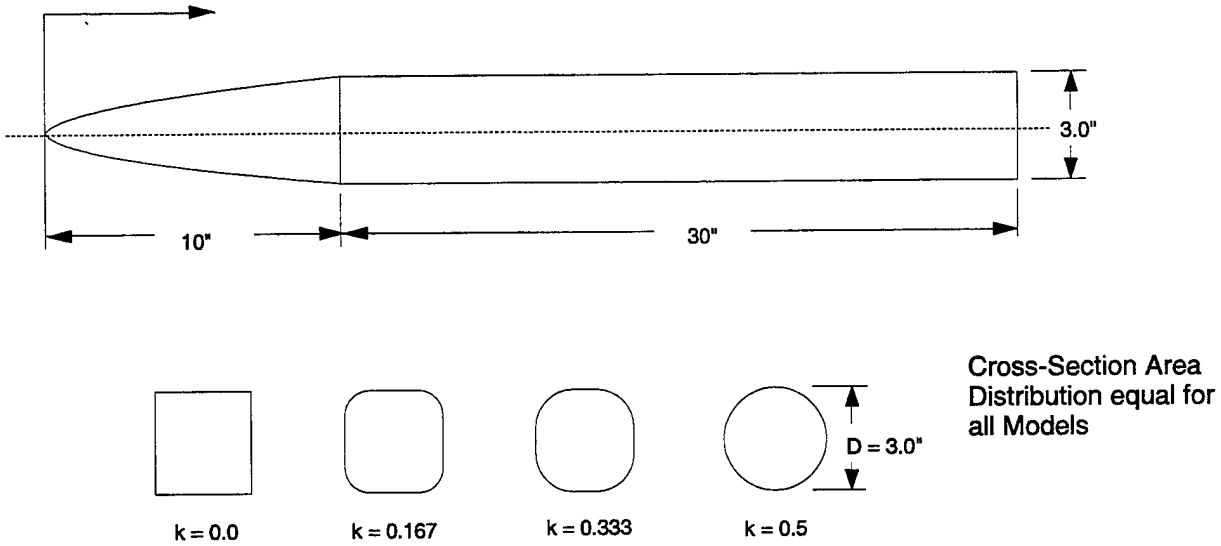

FIGURE 34. BODY ALONE CONFIGURATIONS HAVING SQUARE CROSS SECTIONAL SHAPES OF VARYING CORNER RADII

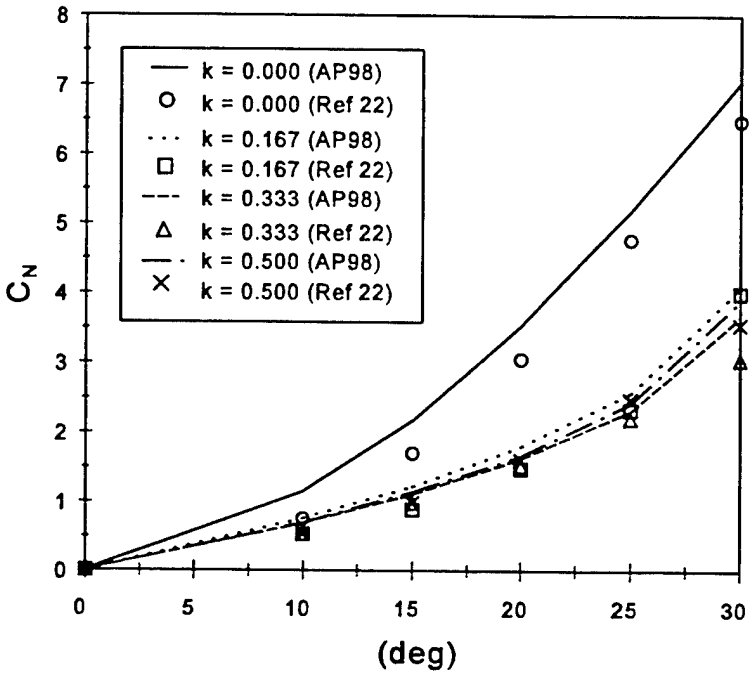

FIGURE 35. NORMAL FORCE COEFFICIENTS FOR SQUARES OF DIFFERENT CORNER RADII AT M = 0.9 (FROM FIGURE 34)

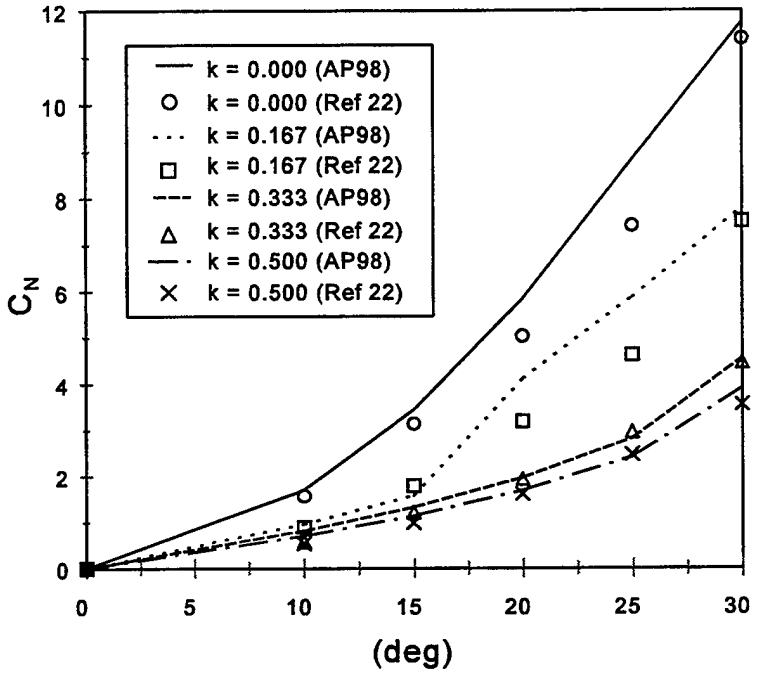

FIGURE 36. NORMAL FORCE COEFFICIENTS FOR DIAMONDS OF DIFFERENT CORNER RADII AT M = 0.9 (FROM FIGURE 34)

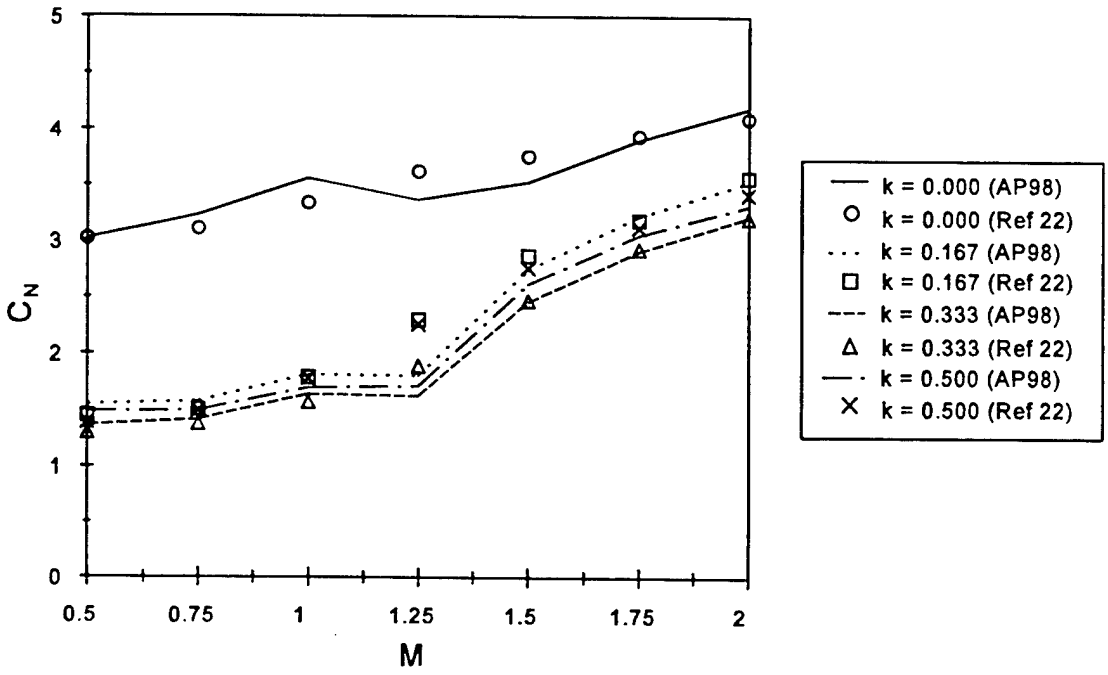

FIGURE 37. NORMAL FORCE COEFFICIENTS FOR SQUARES OF DIFFERENT CORNER RADII AT α = 20 DEG (FROM FIGURE 34)

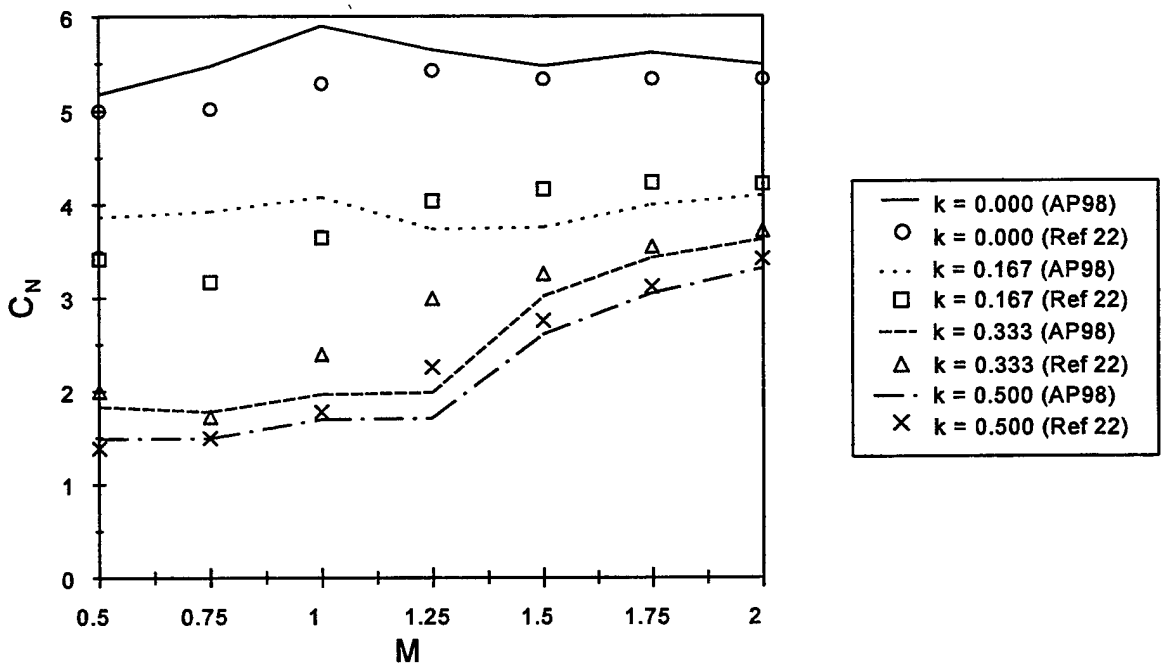

FIGURE 38. NORMAL FORCE COEFFICIENTS FOR DIAMONDS OF DIFFERENT CORNER RADII AT α = 20 DEG (FROM FIGURE 34)

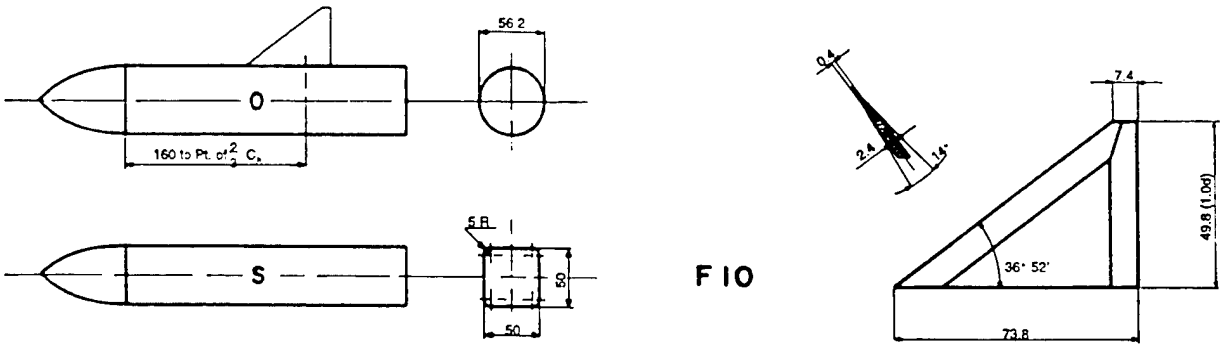

FIGURE 39. COMPONENTS OF BODY ALONE AND WING-BODY CONFIGURATIONS WITH CIRCULAR AND SQUARE CROSS SECTIONS

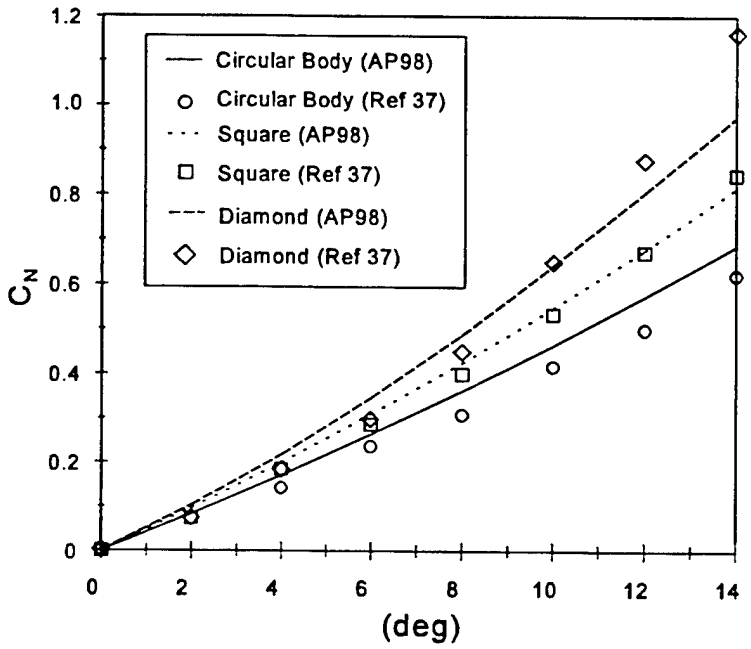

FIGURE 40. NORMAL FORCE COEFFICIENTS FOR SQUARES (k = 0.1) AND DIAMONDS (k = 0.1) OF FIGURE 39 COMPARED TO CIRCULAR BODY AT M = 0.75

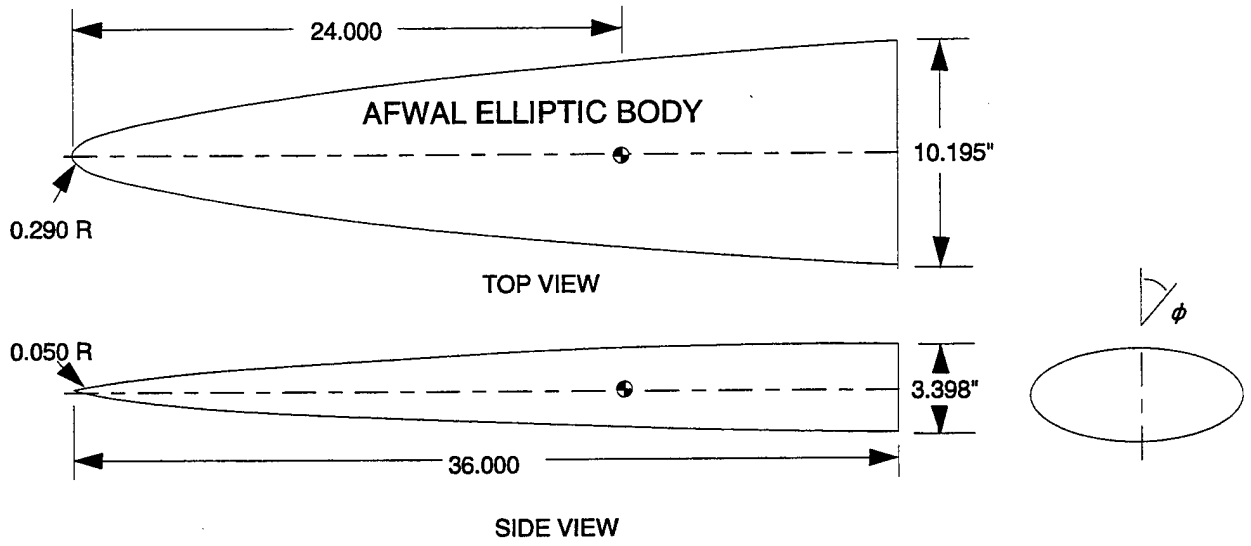

FIGURE 41. GEOMETRIC CONFIGURATION OF 3:1 ELLIPTICAL CROSS SECTION BODY

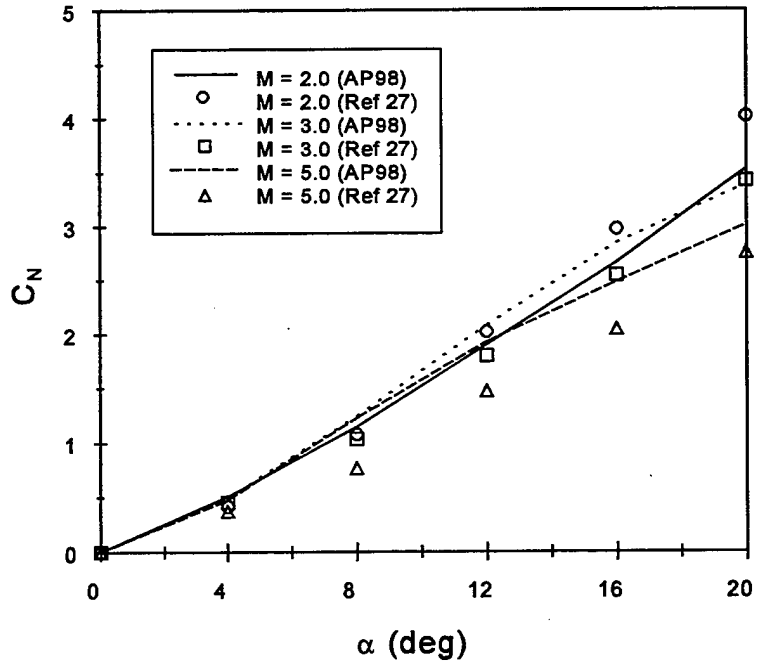

FIGURE 42. NORMAL FORCE COEFFICIENTS FOR AFWAL LIFTING BODY OF FIGURE 41

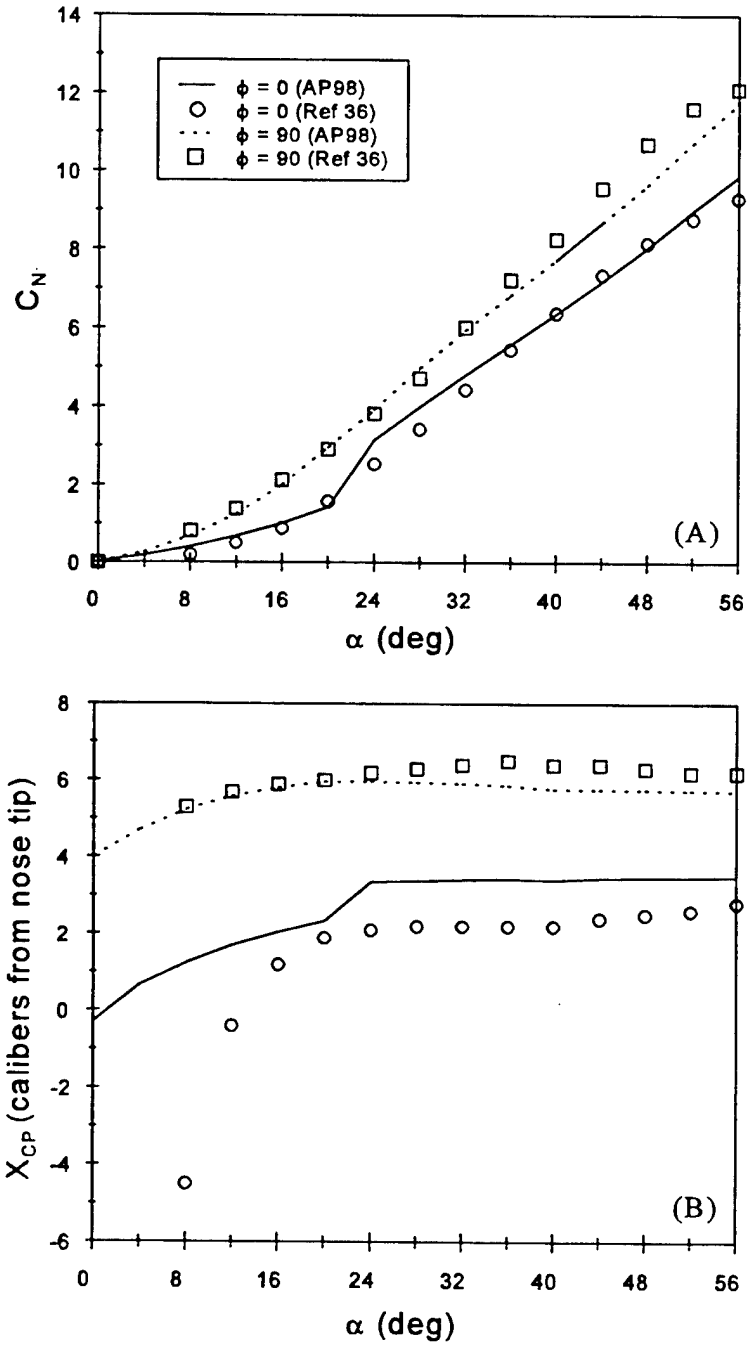

FIGURE 43. AERODYNAMIC DATA FOR BODY OF FIGURE 14 WITH VARIABLE ELLIPTICAL CROSS SECTION AT TWO ROLL POSITIONS AND M = 0.6: (A) NORMAL FORCE COEFFICIENT, (B) CENTER OF PRESSURE

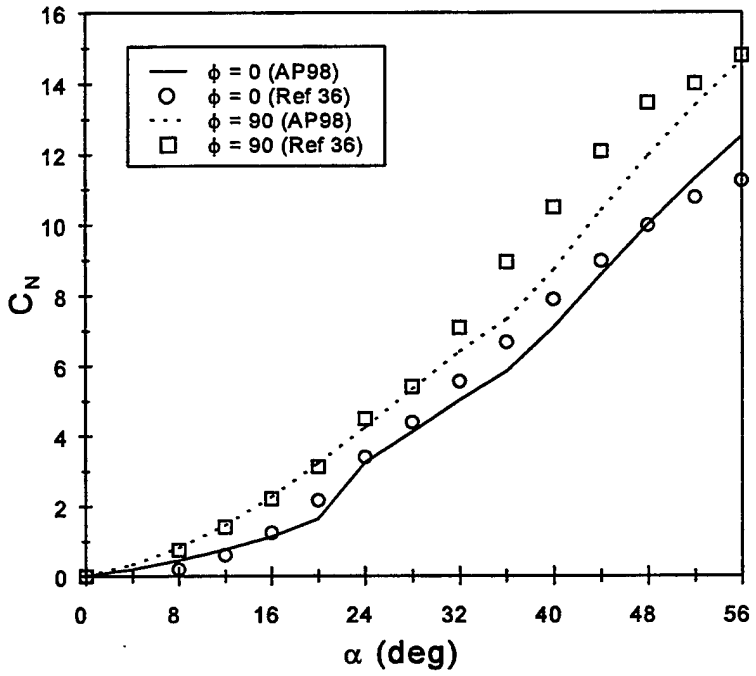

FIGURE 44. NORMAL FORCE COEFFICIENTS FOR BODY OF FIGURE 14 WITH VARIABLE ELLIPTICAL CROSS SECTION AT TWO ROLL POSITIONS AND M = 0.9

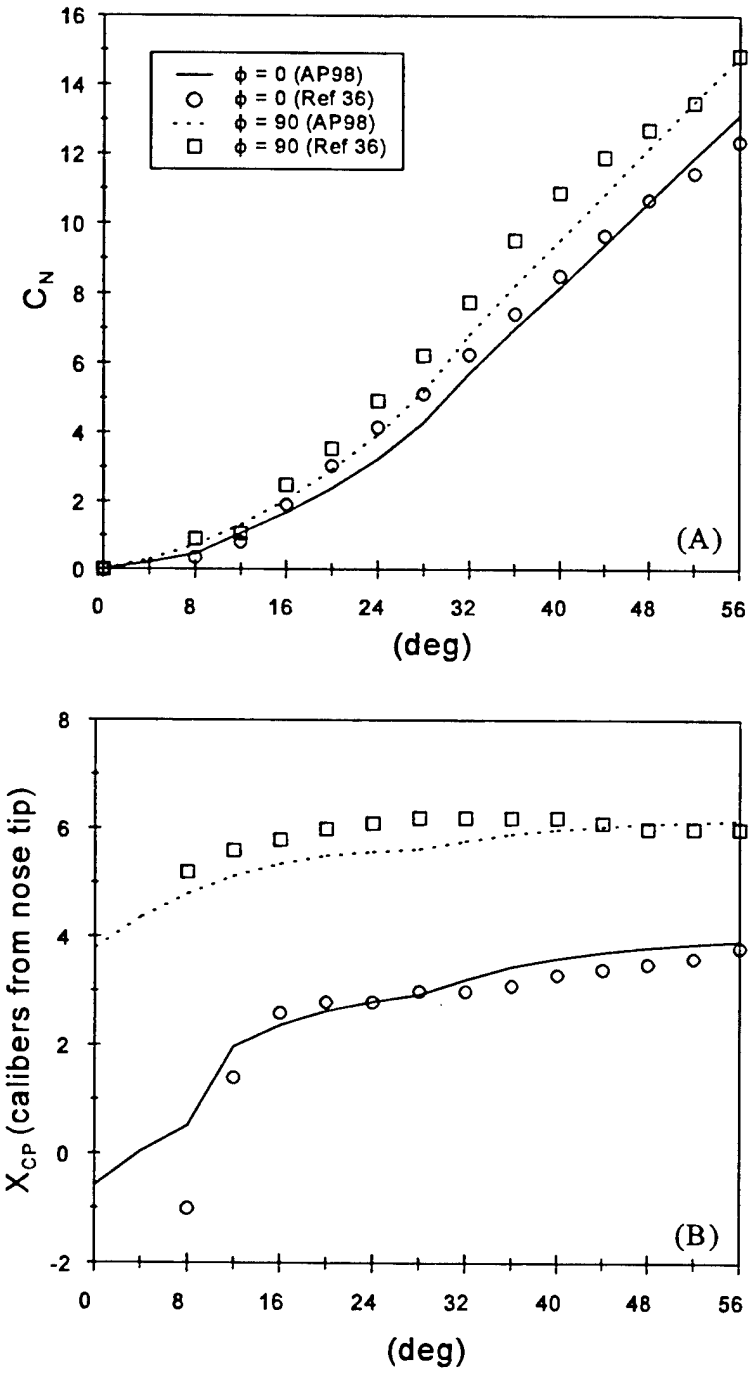

FIGURE 45. AERODYNAMIC DATA FOR BODY OF FIGURE 14 WITH VARIABLE ELLIPTICAL CROSS SECTION AT TWO ROLL POSITIONS AND M = 1.2: (A) NORMAL FORCE COEFFICIENT, (B) CENTER OF PRESSURE

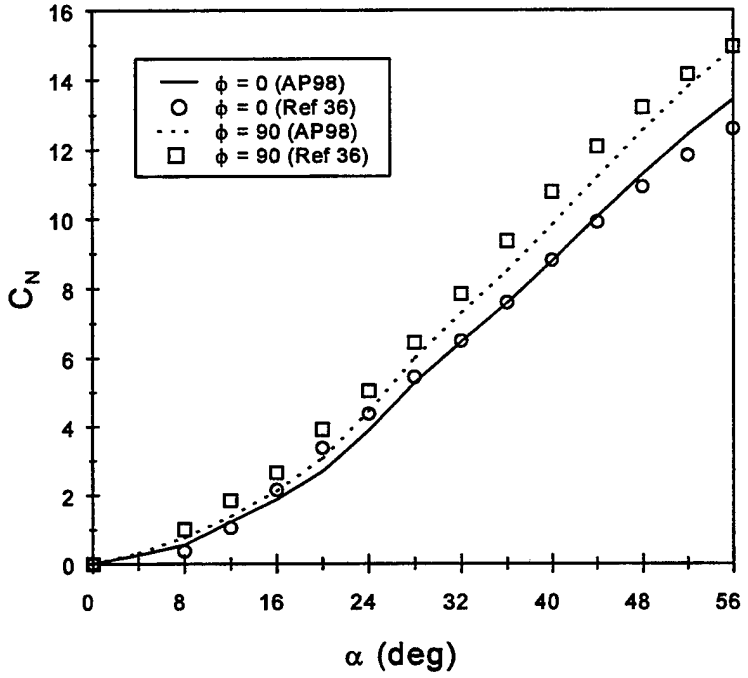

FIGURE 46. NORMAL FORCE COEFFICIENTS FOR BODY OF FIGURE 14 WITH VARIABLE ELLIPTICAL CROSS SECTION AT TWO ROLL POSITIONS AND M = 1.5

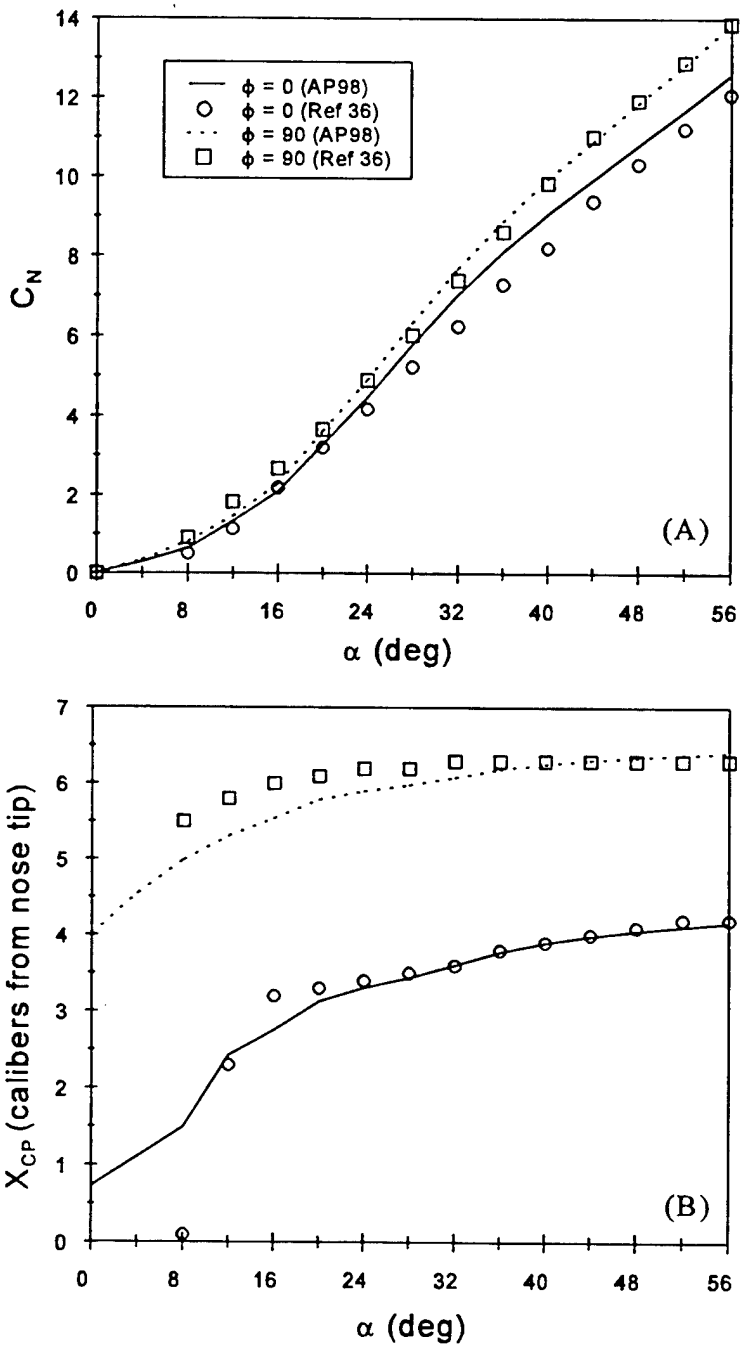

FIGURE 47. AERODYNAMIC DATA FOR BODY OF FIGURE 14 WITH VARIABLE ELLIPTICAL CROSS SECTION AT TWO ROLL POSITIONS AT M = 2.0: (A) NORMAL FORCE COEFFICIENT, (B) CENTER OF PRESSURE

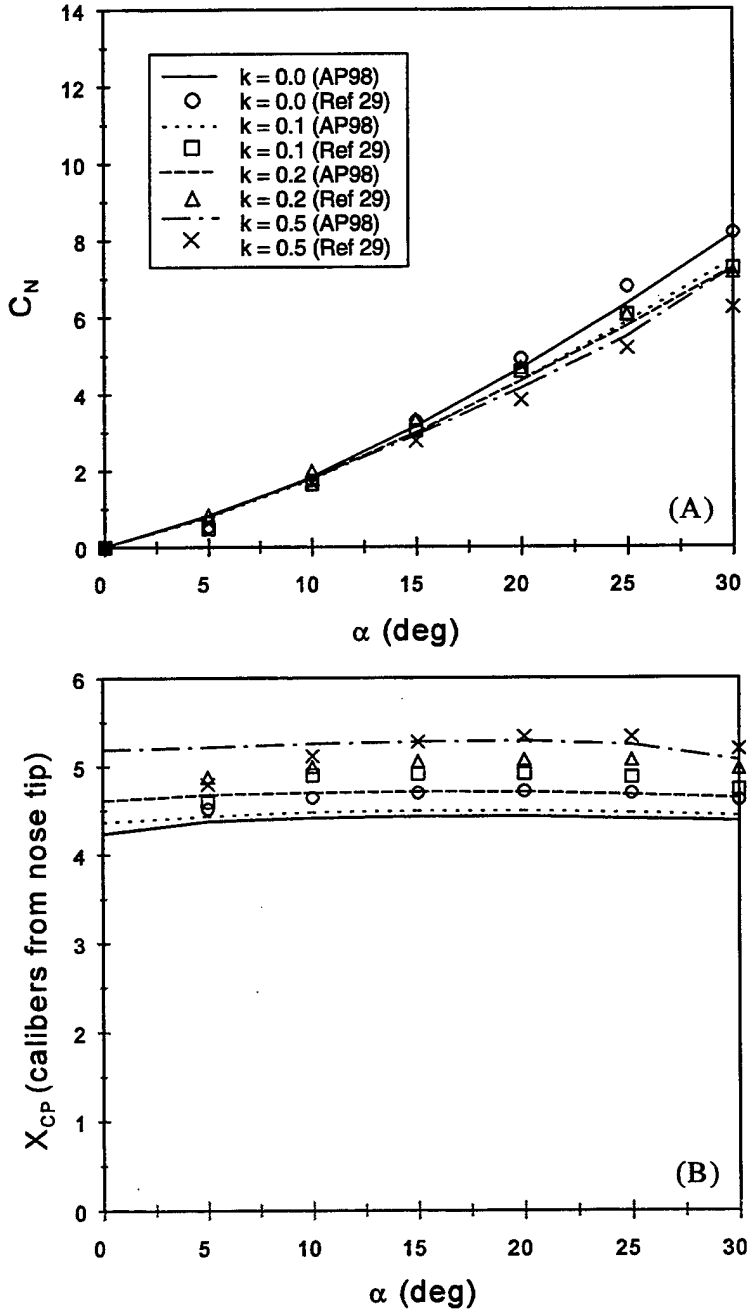

FIGURE 48. AERODYNAMIC DATA FOR WING-BODY CONFIGURATIONS OF FIGURE 30 WITH SQUARE BODIES OF VARIOUS CORNER RADII (FIN F1): (A) NORMAL FORCE COEFFICIENT, (B) CENTER OF PRESSURE

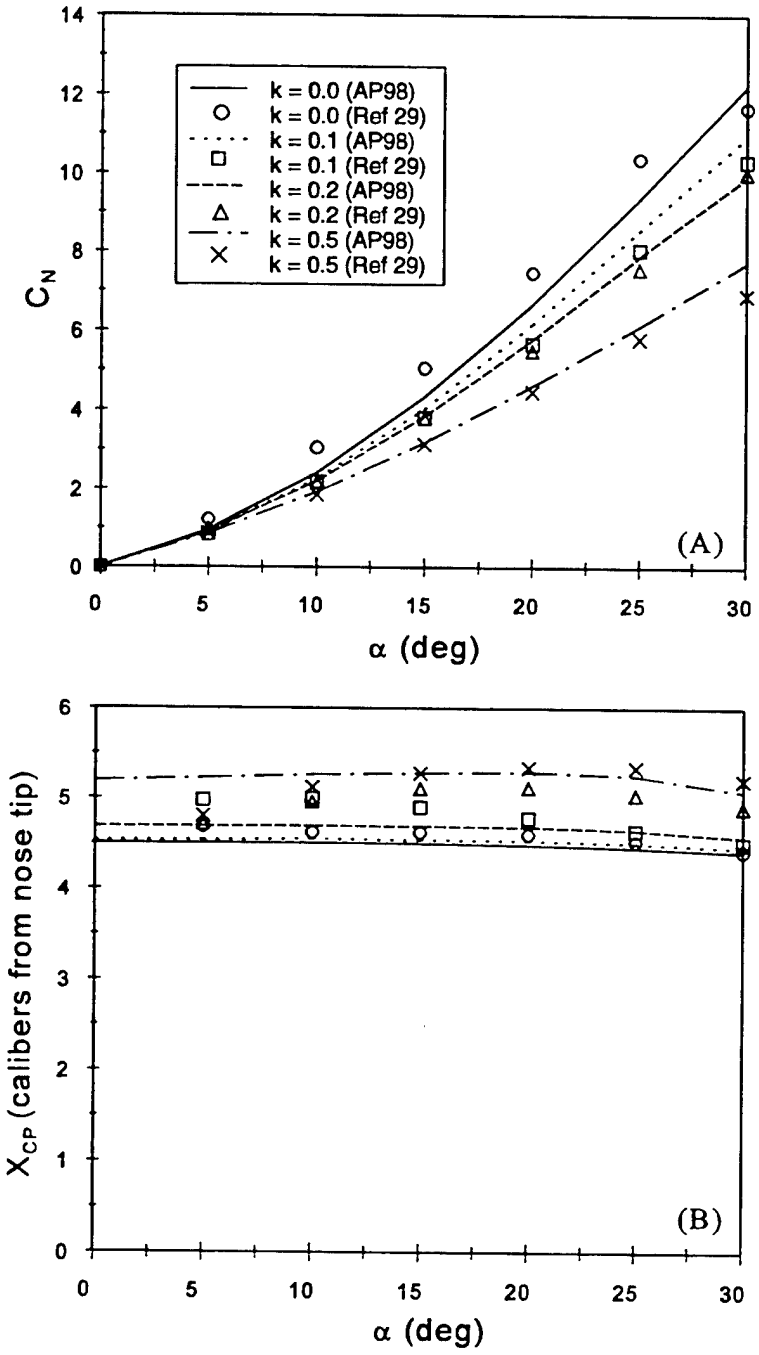

FIGURE 49. AERODYNAMIC DATA FOR WING-BODY CONFIGURATIONS OF FIGURE 30 WITH DIAMOND BODIES OF VARIOUS CORNER RADII (FIN F1): (A) NORMAL FORCE COEFFICIENT, (B) CENTER OF PRESSURE

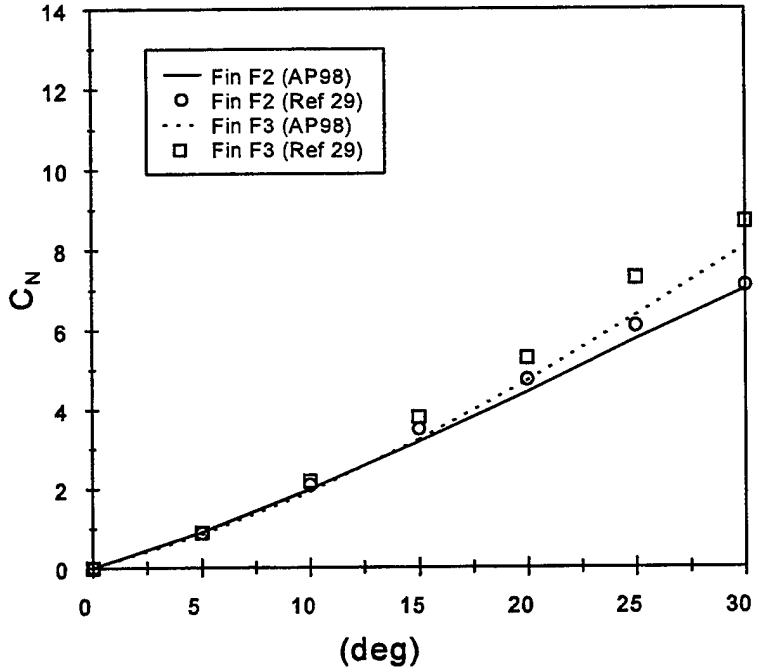

FIGURE 50. NORMAL FORCE COEFFICIENTS FOR THE SQUARE BODY OF FIGURE 30 OF k = 0.2 CORNER RADIUS WITH TWO DIFFERENT FIN CONFIGURATIONS

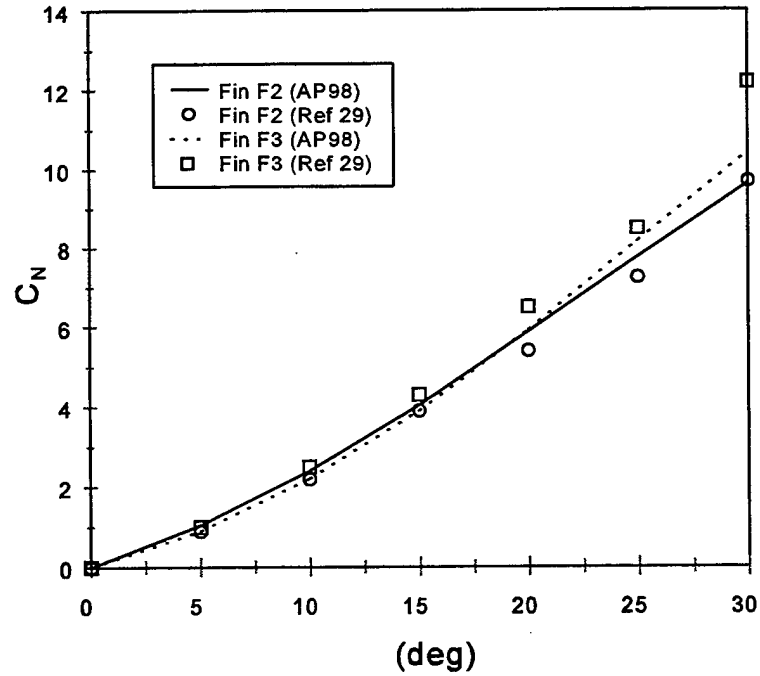

FIGURE 51. NORMAL FORCE COEFFICIENTS FOR THE DIAMOND BODY OF FIGURE 30 OF k = 0.2 CORNER RADIUS WITH TWO DIFFERENT FIN CONFIGURATIONS

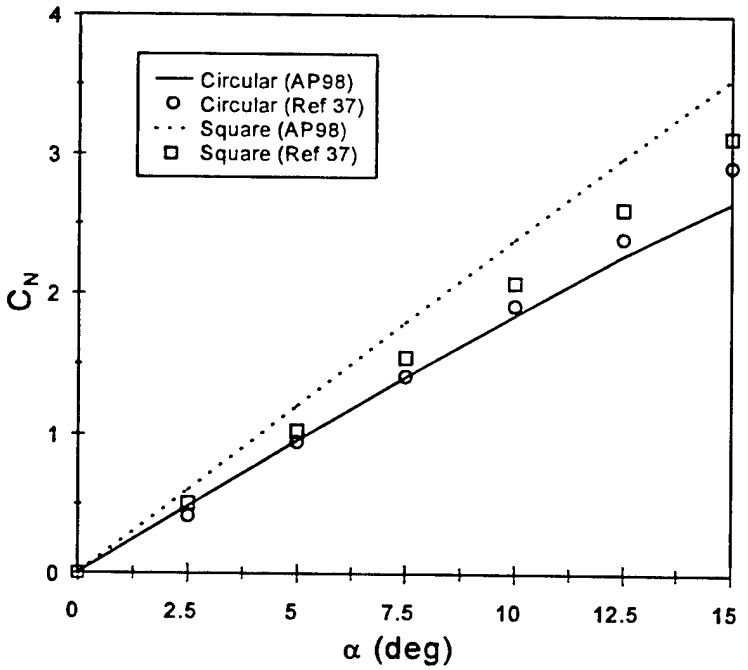

FIGURE 52. NORMAL FORCE COEFFICIENTS FOR CIRCULAR AND SQUARE BODIES OF FIGURE 39 WITH FINS AT $\Phi = 45$ DEG

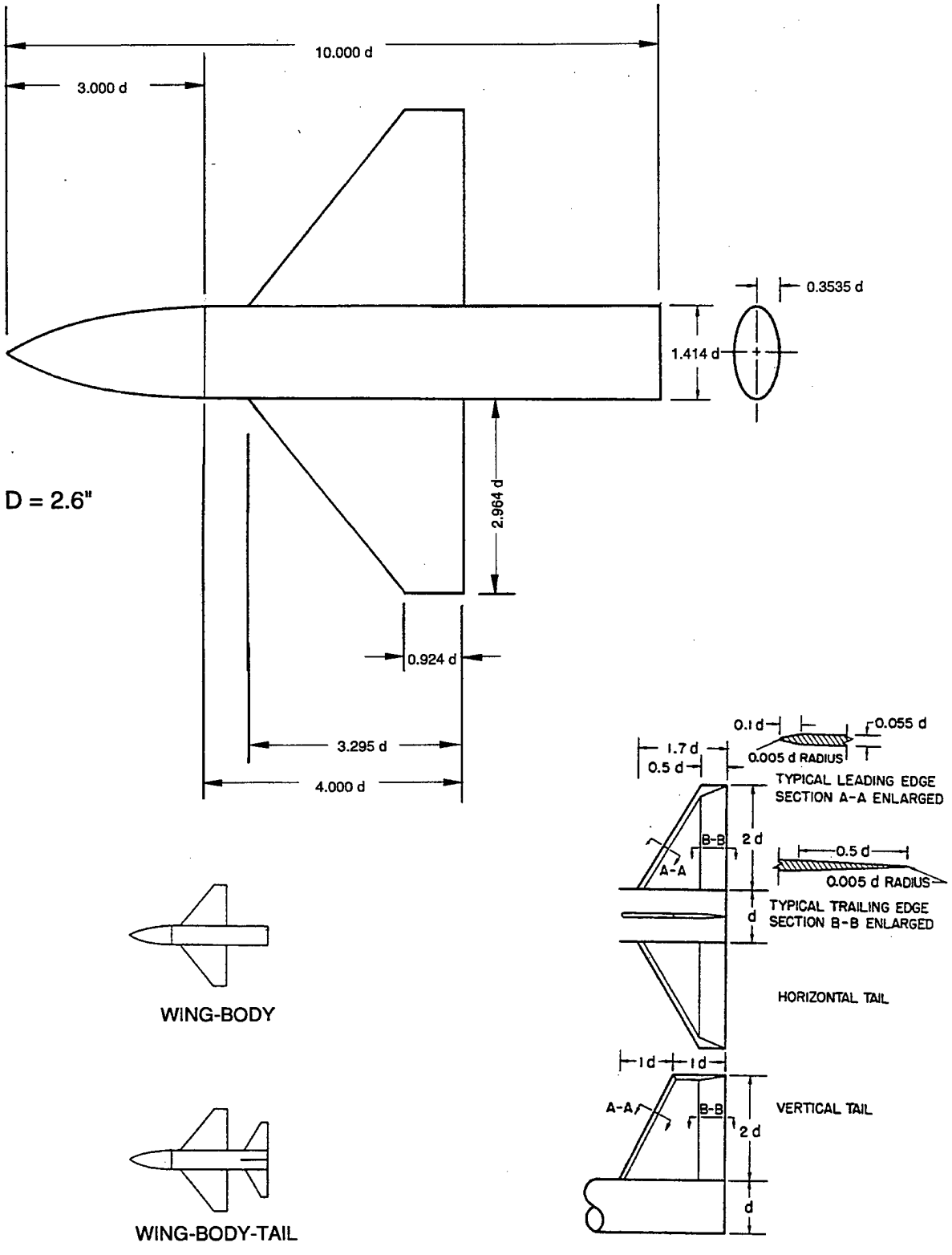

FIGURE 53. GEOMETRY OF THE WING-BODY AND WING-BODY-TAIL CONFIGURATIONS WITH 2:1 ELLIPTICAL BODIES

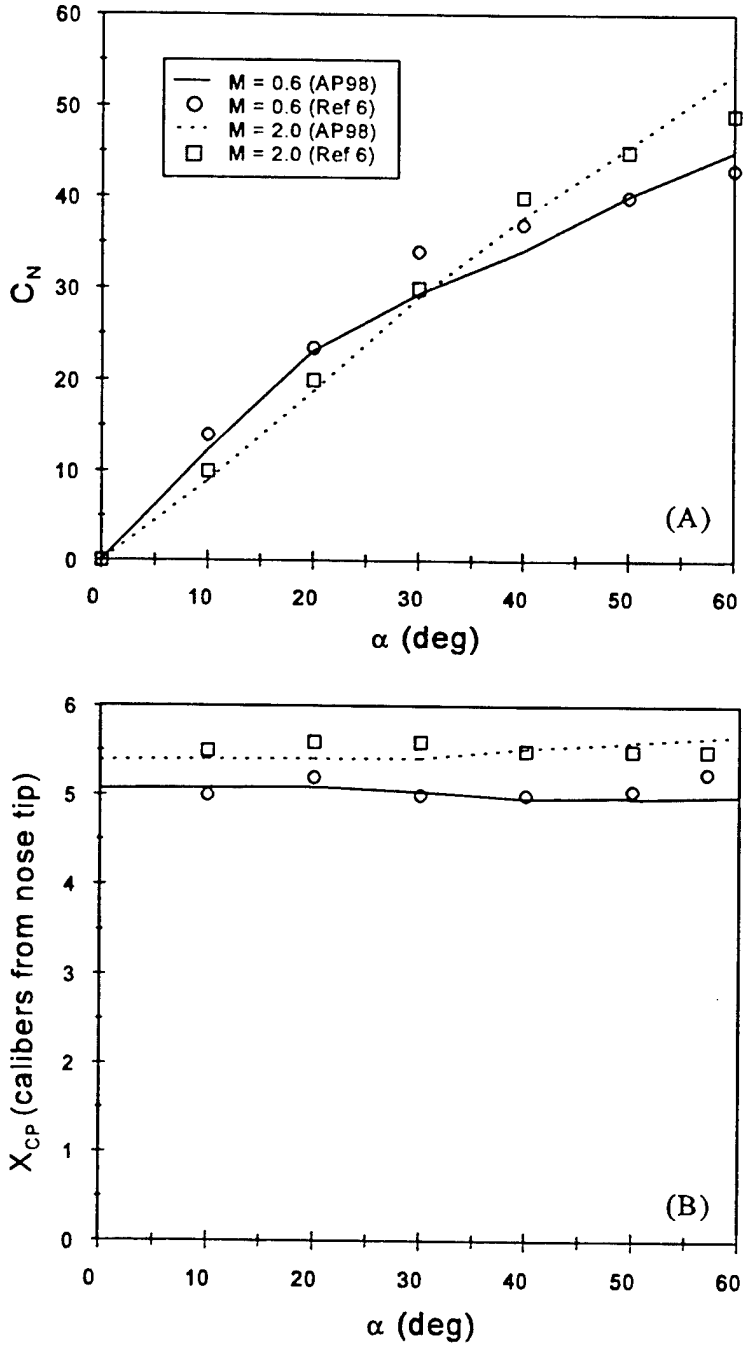

FIGURE 54. AERODYNAMIC DATA FOR THE WING-BODY CONFIGURATION OF FIGURE 53 WITH A 2:1 ELLIPTICAL CROSS SECTION BODY: (A) NORMAL FORCE COEFFICIENT, (B) CENTER OF PRESSURE

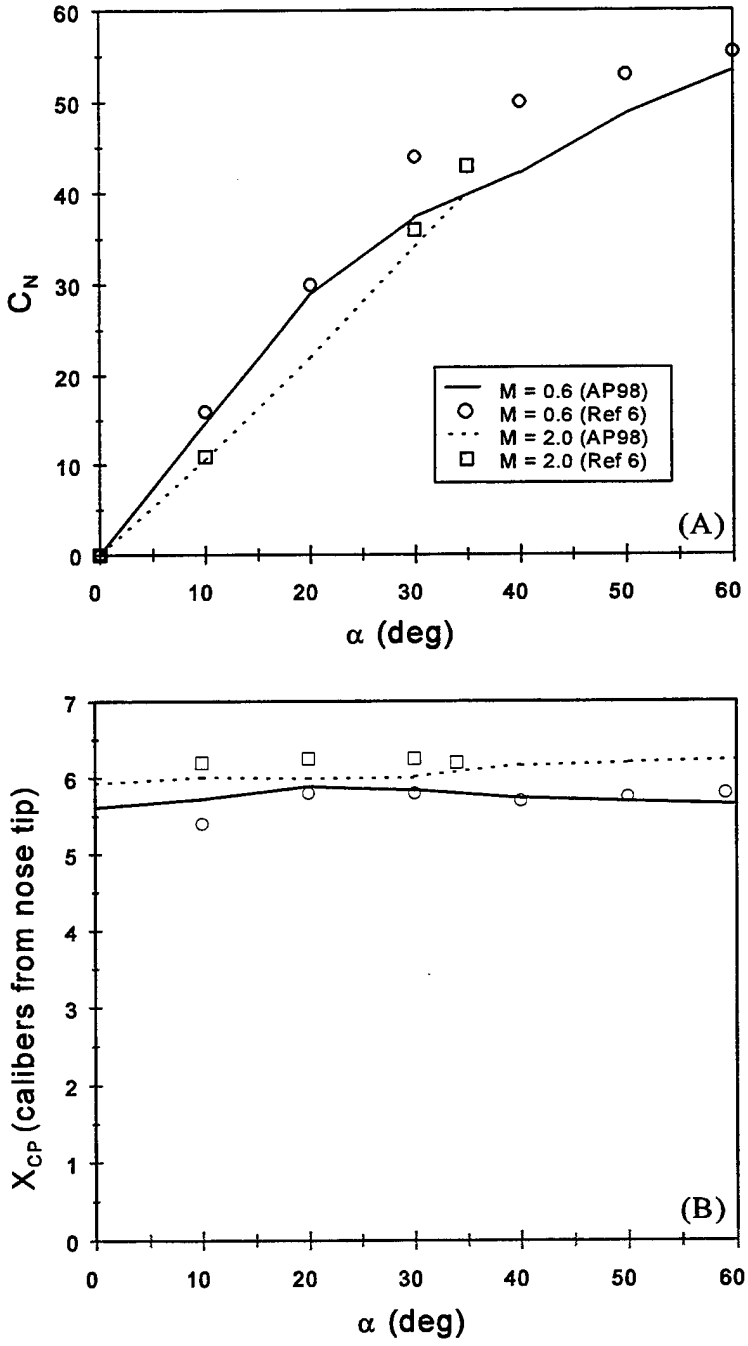

FIGURE 55. AERODYNAMIC DATA FOR THE WING-BODY-TAIL CONFIGURATION OF FIGURE 53 WITH A 2:1 ELLIPTICAL CROSS SECTION BODY: (A) NORMAL FORCE COEFFICIENT, (B) CENTER OF PRESSURE

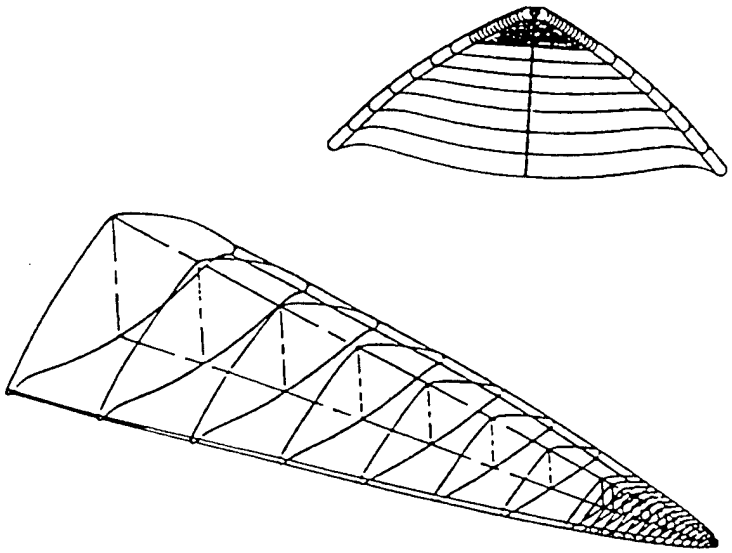

FIGURE 56. WIRE-FRAME GEOMETRY OF THE WAVERIDER (FROM REFERENCE 38)

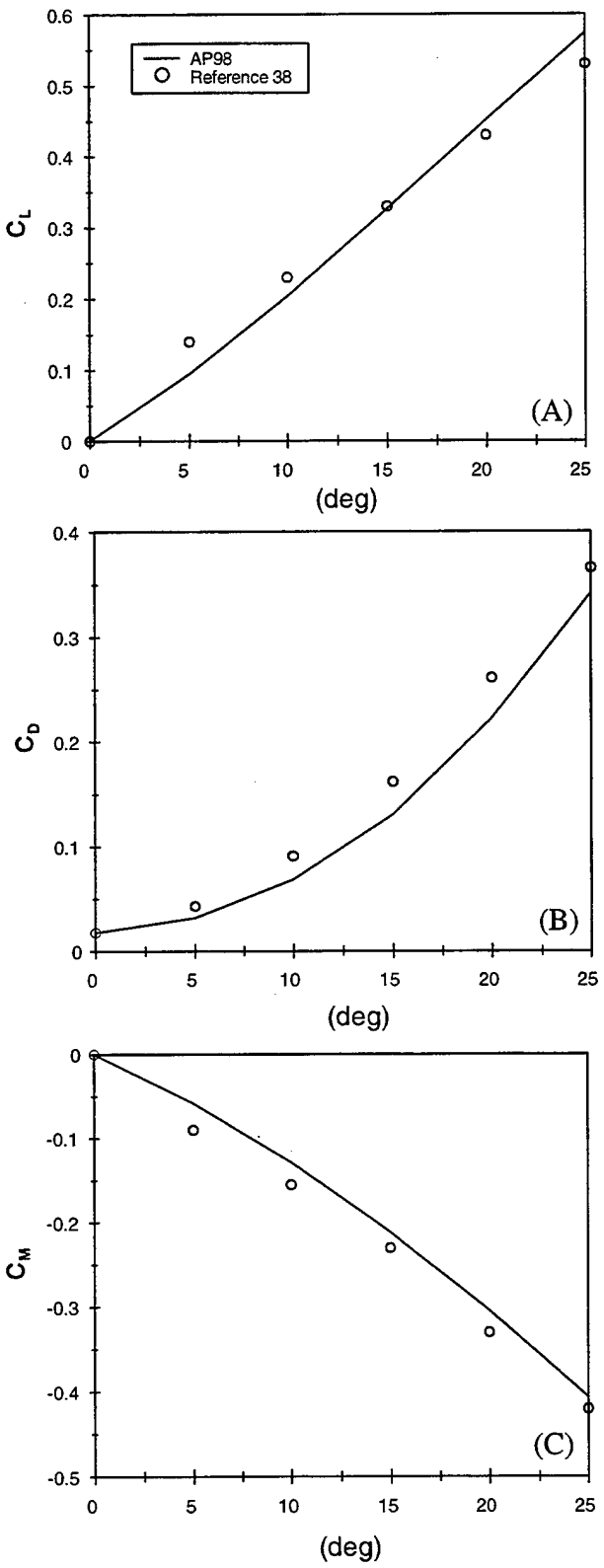

FIGURE 57. AERODYNAMIC DATA FOR THE MACH 14 WAVERIDER OF FIGURE 56:
(A) LIFT COEFFICIENT, (B) AXIAL FORCE COEFFICIENT,
(C) MOMENT COEFFICIENT

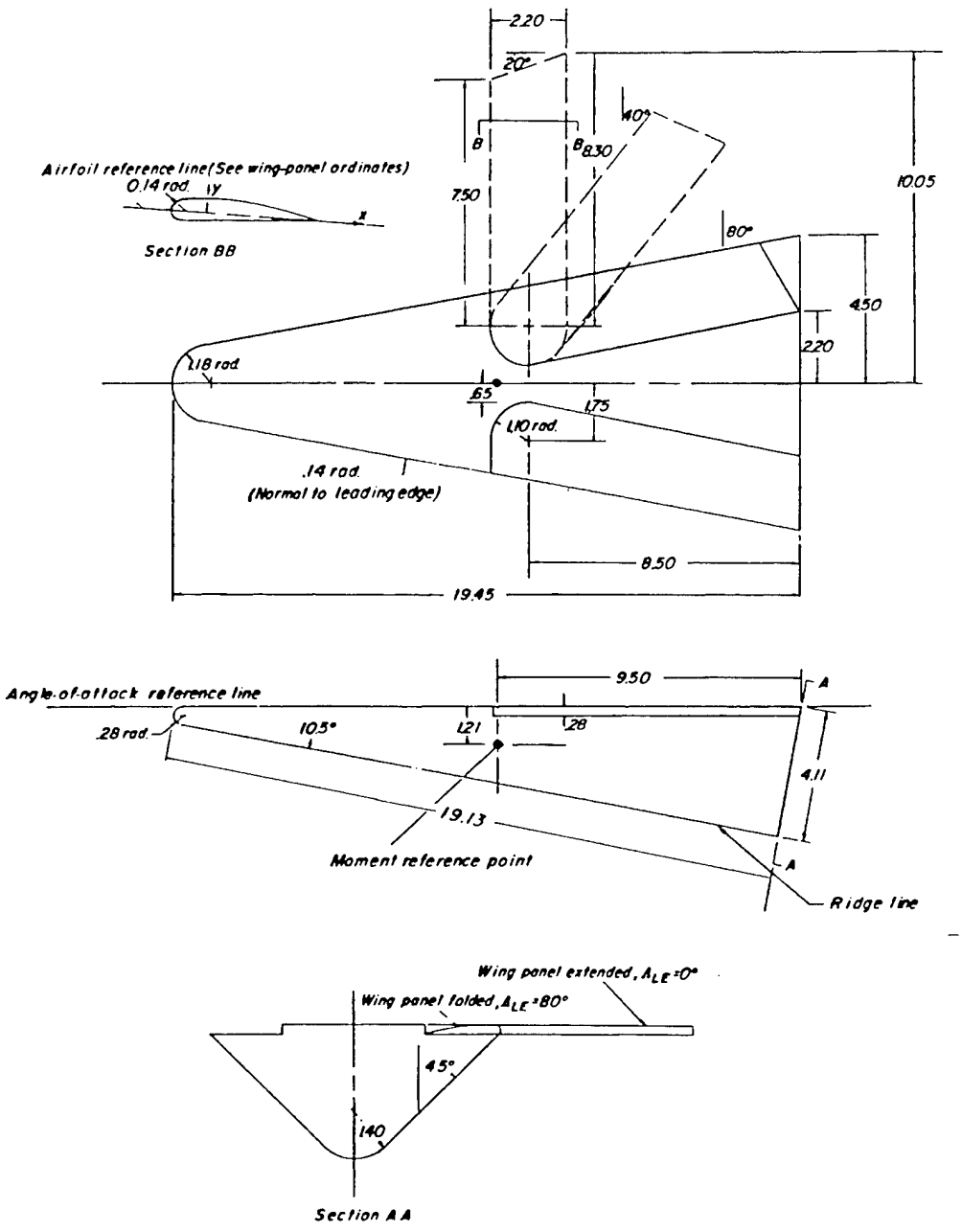

FIGURE 58. GEOMETRY OF THE VARIABLE WING SWEEP LIFTING BODY

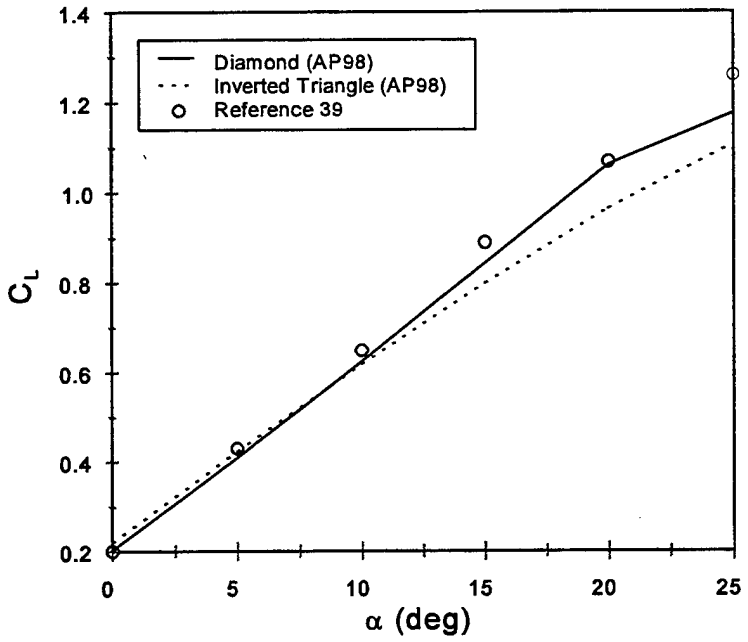

FIGURE 59. LIFT COEFFICIENTS FOR THE BODY-WING CONFIGURATION OF FIGURE 58 COMPUTED BY TWO METHODS AT M = 0.4

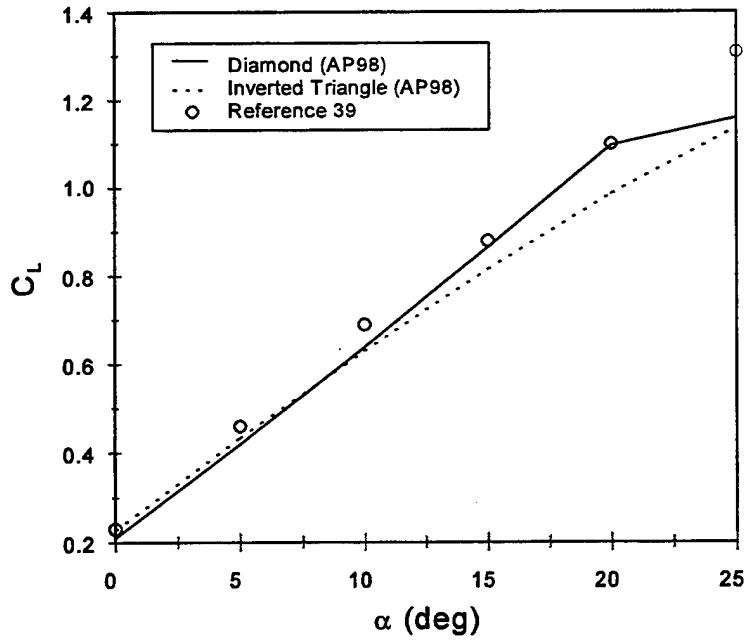

FIGURE 60. LIFT COEFFICIENTS FOR THE BODY-WING CONFIGURATION OF FIGURE 58 COMPUTED BY TWO METHODS AT M = 0.6

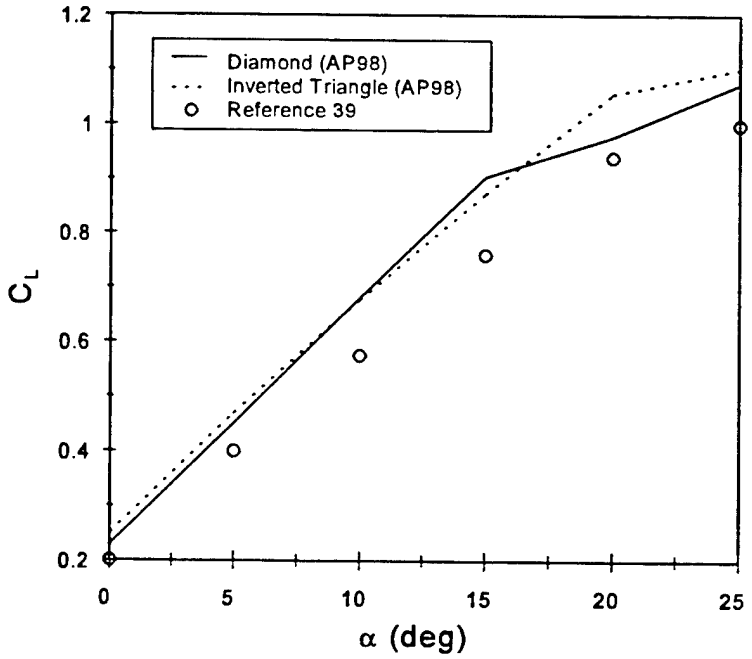

FIGURE 61. LIFT COEFFICIENTS FOR THE BODY-WING CONFIGURATION OF FIGURE 58 COMPUTED BY TWO METHODS AT M = 0.8

4.0 SUMMARY

An improved method has been developed to compute aerodynamics of noncircular cross section shapes. The improved method is based on the Jorgensen[6-10] approach of computing aerodynamics on a noncircular body using circular-body methods; on the Nelson[33] approach for noncircular wing-body interference corrections at low AOA; and on the method of References 13 and 32 for including nonlinearities in the wing-body interference aerodynamics. The new method extends these approaches in several significant ways so as to make the method more general and applicable to most configurations of noncircular cross section.

Specific additions to the current state-of-the-art (SOTA) include: derivation of the Newtonian approximation to the local normal force coefficient per unit length of a noncircular shape to the similar coefficient of a circular shape; derivation of an empirical correction to these Newtonian factors to account for the assumption of high Mach number in their derivation; derivation of an empirical estimate of critical crossflow Reynolds number as a function of the noncircular geometry shape; a method to treat wing-body interference factor corrections as a function of body geometry and freestream parameters; derivation of slender body theory scaling factors to allow aerodynamics to be computed and compared to wind tunnel data where the equivalent diameter or a diameter equal to the side of a square or triangle is used in the data gathering; and an approximate way of treating configurations that have variable, noncircular cross-section shapes.

The new method was applied to all the noncircular configurations found in the literature for which data was available. This included elliptical cross sectional shapes with a/b from 0.5 to 3.0, Mach numbers 0.6 to 3.88, and AOA as high as 58 deg, and some cases with wings; square and triangular cross sectional shapes with sharp and rounded edges, at mostly lower Mach numbers, but some data at Mach number as high as 4, AOA as high as 58 deg, and some cases with wings; a single configuration with a variable cross section shape at Mach numbers 0.6 to 2.0 and AOA to 60 deg; and to two configurations that were quite complex and did not fit within the exact requirements of the geometry options. Results in general for planar aerodynamics were very good. While it is too early to state the overall accuracy of the new nonaxisymmetric body aerodynamic prediction method, it appears the normal force is almost as good as the circular body predictions. To date, we have not found a circular body configuration where average accuracy on C_A, C_N exceed ±10 percent and X_{CP} exceeds ±4 percent of the body length. Here *average* means enough Mach numbers and AOAs to get a good statistical sample.

While the additions to the SOTA in computing approximate aerodynamics are significant, there still remains several challenges. The first and foremost is to compare the present predictions of static aerodynamics to more data. Since many data bases shown in the literature focus on normal force, additional data or CFD computations may be needed to validate and/or modify the axial force and center of pressure prediction techniques. Hopefully, the ballistics range tests at Eglin AFB will

partially address this problem for axial force and low AOA center of pressure prediction. Secondly, it is suspected that once more zero angle of attack axial force data is available, the assumption of the wave drag on the nonaxisymmetric body being equal to that of the axisymmetric body may need to be adjusted. Finally, it is suspected that the Newtonian correction factor for triangles and squares could be improved upon with more data.

5.0 REFERENCES

1. Gentry, A. E.; Smyth, D. N.; and Oliver, W. R., *The Mark IV Supersonic - Hypersonic Arbitrary Body Program*, AFFDL TR-73-159, Wright Patterson Air Force Base, Dayton, OH, 1973.

2. Sidwell, K. W.; Baruah, P. K.; and Bussoletti, J. E., *A Computer Program for Predicting Subsonic or Supersonic Linear Potential Flows About Arbitrary Configurations Using a Higher Order Panel Method*, Vol. II, NASA CR 3252, 1980.

3. Wardlaw, A. B. and Davis, S., *A Second-Order-Gudonov Method for Supersonic Tactical Missiles*, NSWC TR-86-506, NSWCDD, Dahlgren, VA, 1986.

4. Walters, R. W.; Slack, D. C.; Cimmella, P.; Applebaum, M. P.; and Frost, C., "A Users Guide for GASP," Virginia Polytechnic Institute and State University, Department of Aerospace and Ocean Engineering, Blacksburg, VA, Nov 1990.

5. Whitcomb, R. T., *A Study of the Zero-Lift Drag Rise Characteristics of Wing-Body Combinations Near the Speed of Sound*, NACA Report 1273, 1956.

6. Jorgensen, L. H., *Prediction of Static Aerodynamic Characteristics for Slender Bodies Alone and with Lifting Surfaces to Very High Angles of Attack*, NASA TR R-474, Sep 1977.

7. Jorgensen, L. H., *Inclined Bodies of Various Cross Sections at Supersonic Speeds*, NASA Memo 10-3-58A, 1958.

8. Jorgensen, L. H., *Prediction of Static Aerodynamic Characteristics for Space-Shuttle-Like and Other Bodies at Angles of Attack from 0 ° to 180 °*, NASA TN D-6996, 1973.

9. Jorgensen, L. H., "Estimation of Aerodynamics for Slender Bodies Alone and with Lifting Surfaces at α's from 0° to 90°," *AIAA Journal*, Vol. 11, No. 3, Mar 1973, pp. 409-412.

10. Jorgensen, L. H., *A Method for Estimating Static Aerodynamic Characteristics for Slender Bodies of Circular and Noncircular Cross Section Alone and with Lifting Surfaces at Angles of Attack from 0 ° to 90 °*, NASA TN D-7228, 1973.

11. Vukelich, S. R. and Jenkins, J. E., "Missile DATCOM: Aerodynamic Prediction on Conventional Missiles Using Component Build-up Techniques," AIAA paper no. 84-0388, 1984.

REFERENCES (Continued)

12. Hemsch, M. J. and Nielsen, J. N., "Equivalent Angle-of-Attack Method for Estimating Nonlinear Aerodynamics of Missile Fins," *Journal of Spacecraft and Rockets (JSR)*, Vol. 20, No. 4, Jul-Aug 1983.

13. Moore, F. G.; McInville, R. M.; and Hymer, T., *The 1995 Version of the NSWC Aeroprediction Code: Part I - Summary of New Theoretical Methodology*, NSWCDD/TR-94/379, Feb 1995.

14. Pitts, W. C.; Nielsen, J. N.; and Kaattari, G. E., *Lift and Center of Pressure of Wing-Body-Tail Combinations at Subsonic, Transonic, and Supersonic Speeds*, NACA TR 1307, 1957.

15. Moore, F. G. and Hymer, T. C., *An Improved Method for Predicting Axial Force at High Angle of Attack*, NSWCDD/TR-96/240, Feb 1997.

16. Vukelich, S. R.; Stoy, S. L.; Burns, K. A,; Castillo, J. A.; and Moore, M. E., *"Missile DATCOM" - Volume I - Final Report*, AFWAL-TR-86-3091, Dec 1988.

17. Jones, N. H. and Zollars, G. J., *Investigation of the Aerodynamics of Square Cross Section Missiles*, USAFA-TR-83-15, U.S. Air Force Academy, Colorado Springs, CO, Sep 1983.

18. Polhamus, E. C.; Geller, B. W.; and Greenwald, K. J., *Pressure and Force Characteristics of Noncircular Cylinders as Affected by Reynolds Number with a Method Included for Determining the Potential Flow About Arbitrary Shapes*, NASA TR R-46, 1959.

19. Lockwood, V. E., *Effects of Reynolds Number and Flow Incidence on the Force Characteristics of a Family of Flat-Front Cylinders*, NASA TN D-3932, May 1967.

20. Polhamus, E. C., *Effect of Flow Incidence and Reynolds Number on Low-Speed Aerodynamic Characteristics of Several Noncircular Cylinders with Applications to Directional Stability and Spinning*, NACA TN 4176, Jan 1958.

21. Daniel, D. C.; Yechout, T. R.; and Zollars, G. J., "Experimental Aerodynamic Characteristics of Missiles with Square Cross Sections," *JSR*, Vol. 19, Mar-Apr 1982, pp. 167-172.

22. Schneider, W., "Experimental Investigation of Bodies with Noncircular Cross Section in Compressible Flow," AGARD-CP-336, Symposium on Missile Aerodynamics, Trondheim, Norway, Sep 1982, pp. 19-1 to 19-15.

23. Sellers, M. E. and Siler, L. G., *Pressure and Static Force Test of Three Elliptic Missile Body Configurations at Mach Numbers 1.5 to 5.0*, AEDC-TSR-83-V44, 1983.

REFERENCES (Continued)

24. Shereda, D. E.; Amidon, P. F.; Dahlem, V., III; and Brown-Edwards, E., *Pressure Test of Three Elliptical Missile Body Configurations at Mach Numbers 1.5 to 5.0*, Wright-Patterson AFB, OH, AFWAL TM 84-236-FIMG, Dec 1984.

25. Lijewski, L. E.; Zollars, G. J.; Yechout, T. R.; and Haupt, B. F., "Experimental Flowfield Measurements of Missiles with Square Cross Sections," AIAA-82-0055, AIAA 20th Aerospace Sciences meeting, Orlando, FL, Jan 1982.

26. Stoy, S. L. and Vukelich, S. R., "Prediction of Aerodynamic Characteristics of Unconventional Missile Configurations using Component Buildup Techniques," AIAA-86-0489, AIAA 24th Aerospace Sciences meeting, Reno, NV, Jan 1986.

27. Amidon, P. F., "Supersonic Aerodynamic Characteristics of Elliptic Cross Section Bodies," AIAA 85-1607, AIAA 18th Fluid Dynamics and Plasmadynamics and Lasers Conference, Cincinnati, OH, Jul 1985.

28. Vukelich, S. R., "Aerodynamic Prediction of Elliptically-Shaped Missile Configurations Using Component Build-up Methodology," AIAA-85-0271, AIAA 23rd Aerospace Sciences meeting, Reno, NV, Jan 1985.

29. Zollars, G. J.; Yechout, T. R.; Daniel, D. C.; and Lijewski, L. E., *Experimental Aerodynamic Characteristics of Missiles with Square Cross Sections*, USAFA-TN-83-8, U.S. Air Force Academy, Colorado Springs, CO, May 1983.

30. Hoerner, S. F., Fluid Dynamic Drag, Copyright 1965, Published by Hoerner Fluid Dynamics, P. O. Box 342, Brick Town, NJ, pp. 16-15, 16-16.

31. Delany, N. K. and Sorensen, N. E., *Low Speed Drag of Cylinders of Various Shapes*, NACA TN 3038, Nov 1953.

32. Moore, F. G. and McInville, R., *Extension of the NSWCDD Aeroprediction Code to the Roll Position of 45 Degrees*, NSWCDD/TR-95/160, Dec 1995.

33. Nelson, H. F., "Wing-Body Interference Lift for Supersonic Missiles with Elliptical Cross-Section Fuselages," *JSR* Vol. 26, No. 5, Sep-Oct 1989, pp. 322-329.

34. Est, B. E. and Nelson, H. F., "Wing-Body Carryover and Fin Center of Pressure for Missiles with Noncircular Fuselage Cross Sections," AIAA 91-2856, Atmospheric Flight Mechanics Conference, New Orleans, LA, Aug 1991.

35. Sigal, A., "Methods of Analysis and Experiments for Missiles with Noncircular Fuselages," Chapter 5, pp. 171-217 of *Tactical Missile Aerodynamics*, Progress in Aeronautics and Astronautics Series, J. Nielsen, Editor, AIAA, Washington, DC, 1991.

REFERENCES (Continued)

36. Jorgenson, L. H. and Nelson, E. R., *Experimental Aerodynamic Characteristics for Bodies of Elliptic Cross Section at Angles of Attack from 0 ° to 58 ° and Mach Numbers from 0.6 to 2.0*, NASA TM X-3129, 1975.

37. Sigal, A. and Lapidot, E., "Aerodynamic Characteristics of Configurations Having Bodies with Square, Rectangular, and Circular Cross Sections," *Journal of Spacecraft and Rockets*, Vol. 26, No. 2, Mar-Apr 1989.

38. Gillum, M. J. and Lewis, M. J., "Analysis of Experimental Results on a Mach 14 Waverider with Blunt Leading Edges," AIAA 96-0812, 34th Aerospace Sciences Meeting & Exhibit, Reno, NV, Jan 1996.

39. Spencer, B., *Longitudinal Aerodynamic Characteristics at Mach Numbers from 0.40 to 1.10 of a Blunted Right-Triangular Pyramidal Lifting Reentry Configuration Employing Variable-Sweep Wing Panels*, NASA TN D-1518, 1963.

6.0 SYMBOLS AND DEFINITIONS

AOA	Angle of Attack
APC	Aeroprediction code
AP95	Aeroprediction 1995
AP98	Aeroprediction 1998
LT	Linear theory
NSWCDD	Naval Surface Warfare Center, Dahlgren Division
SBT	Slender body theory
A_C	Cross-sectional area of circular cylinder (ft^2)
A_{eq}	Cross-sectional area of circular cylinder equal to that of body with noncircular cross section
A_i	Apparent mass values from slender body theory (from Reference 16)
A_{ref}	Reference area (maximum cross-sectional area of body, if a body is present, or planform area of wing if wing alone) (ft^2)
a,b	Semimajor and semiminor axis, respectively, of ellipse
a′	Body shape parameter (see Reference 34)
A(x)	Body cross-sectional area as a function of position along body axis (ft^2)
AR	Wing or tail aspect ratio
Cir	Circumference of body (ft)
C_A	Axial force coefficient
$(C_A)_{\alpha=0}$	Axial force coefficient at zero degree angle of attack
C_{A_B}	Axial force coefficient component due to base pressure
C_{A_f}	Axial force coefficient component due to skin friction

C_{A_W}	Axial force component due to forebody and boattail or flare pressure
C_D	Drag coefficient
C_d, C_{d_C}	Local and total crossflow drag coefficients
$(C_{d_C})_1$, $(C_{d_C})_2$	Subcritical and supercritical value, respectively, of C_{d_C}
C_M	Pitching moment coefficient
C_{M_L}	Linear component of pitching moment coefficient
$C_{M_{NL}}$	Nonlinear component of pitching moment coefficient
$(C_n/C_{n_O})_{SB}$ $(C_n/C_{n_O})_N$	Ratio of the local normal force coefficient of a body with a noncircular cross section to that with a circular cross section calculated by slender body and Newtonian theory respectively
C_N	Total normal force coefficient
C_{N_B}	Normal force coefficient of the body
C_{N_L}	Linear component of the normal force coefficient
$C_{N_{NL}}$	Nonlinear component of the normal force coefficient
$(C_{N_\alpha})_W$, $(C_{N_\alpha})_T$	Normal force coefficient slope of wing and tail respectively
$C_{N_{T(W)}}$	Normal force coefficient on tail due to wing-shed vortices
C_P	Pressure coefficient
C_{P_B}	Base pressure coefficient
C_{P_i}	Local pressure coefficient at orifice i (Table 1)
C_{P_O}	Stagnation pressure coefficient
C_r	Root chord of lifting surface (ft)
d, d_B	Diameter of body and base diameter of body respectively
F	Ratio of wing-body interference factor of a noncircular cross-section configuration to that of a circular cross-section configuration

k	Parameter used to define corner radius for squares and triangles ($k = r_n/W_M$)
$k_{B(W)}$, $k_{B(T)}$	Ratio of additional body normal force coefficient due to the presence of a deflected wing or tail to that of the wing or tail alone at $\alpha = 0$ deg
$k_{W(B)}$, $k_{T(B)}$	Ratio of normal force contribution of a deflected wing or tail in the presence of a body to that of the wing or tail alone at $\alpha = 0$ deg
K	Ratio of lifting surface normal force coefficient in the presence of a body to that of the lifting surface alone at $\delta = 0$ deg
$K_{B(W)}$, $K_{B(T)}$	Ratio of additional body normal force coefficient in the presence of a wing or tail to that of the wing or tail alone at $\delta = 0$ deg
$[K_{B(W)}]_{MIN}$	Minimum value of $K_{B(W)}$
$K_{W(B)}$, $K_{T(B)}$	Ratio of wing or tail normal force coefficient in the presence of a body to that of the wing or tail alone at $\delta = 0$ deg
K_{WB}	$K_{W(B)} + K_{B(W)}$
ℓ_{ref}	Reference length which is body diameter
ℓ_1, ℓ_2, ℓ_3, ℓ_i	Individual segments of body length where body has variable noncircular cross section
M	Mach number
M_N	Mach number normal to body = $M \sin \alpha$
M_{N_C}	Normal Mach number where flow transitions from subcritical to supercritical conditions
M_{N_O}	Value of normal Mach number to body used in Newtonian correction factor calculation
M_∞	Freestream Mach number
NF	Newtonian correction factor
NF_0	Newtonian correction factor for crossflow Mach number of zero on squares and triangles
NF_1	Newtonian correction factor for an ellipse at $\alpha \geq 20$ deg

P, P_∞	Pressure and freestream pressure (lb/ft^2)
r	Local body radius (ft)
r_{eq}, d_{eq}	Radius and diameter, respectively, of a circular cross-section body which has same cross-sectional area as that of noncircular cross-section body
r_n	Corner radius of a rounded corner on square or triangle
R_N	Reynolds number
R_{N_C}	Reynolds number where flow transitions from subcritical to supercritical conditions
R_{N_D}	Reynolds number based on body diameter
$R_{N_{eff}}$	An effective Reynolds number above which the flow transitions from subcritical to supercritical conditions
s	Radius of body plus wing or tail semispan
SBTSF	Slender body theory scaling factor
V_∞	Freestream velocity
V_N	Velocity normal to body
V_{NW}	Velocity normal to wing
W	Length of one side of a triangle or square
W_m	Maximum diameter of a triangle or square as measured normal to the velocity vector
x	Distance along body axis (ft)
x_{CP}	Center of pressure measured about some reference location
x_m	Reference location about which center of pressure is measured
α	Angle of attack (rad or deg)
β	Angle between body axis and a tangent to the body surface

α_1, α_2, α_C α_D, α_M	Values of AOA upon which the nonlinear term of the wing-body and body-wing interference factors are based
γ	Ratio of specific heats
δ	Deflection angle of control surface (rad, deg)
η	Parameter used in viscous crossflow theory for nonlinear body normal force (in this context, it is the ratio of the normal force of a circular cylinder of given length-to-diameter ratio to that of a cylinder of infinite length)
ρ	Density (slugs/ft^3) of air
Φ	Roll position of missile ($\Phi = 0$ deg corresponds to fins in the plus (+) orientation) and the leeward plane. $\Phi = 45$ deg corresponds to fins rolled to the cross (×) orientation
λ	Taper ratio of fin = C_t/C_r
θ	Angle between the body axis and a normal to the body surface ($\theta = \pi/2 - \beta$)

APPENDIX A

DERIVATION OF $(C_n/C_{n_O})_N$ FOR SQUARE AND TRIANGULAR CROSS-SECTION BODIES

There are four configurations of interest. These four are shown in Figure A-1.

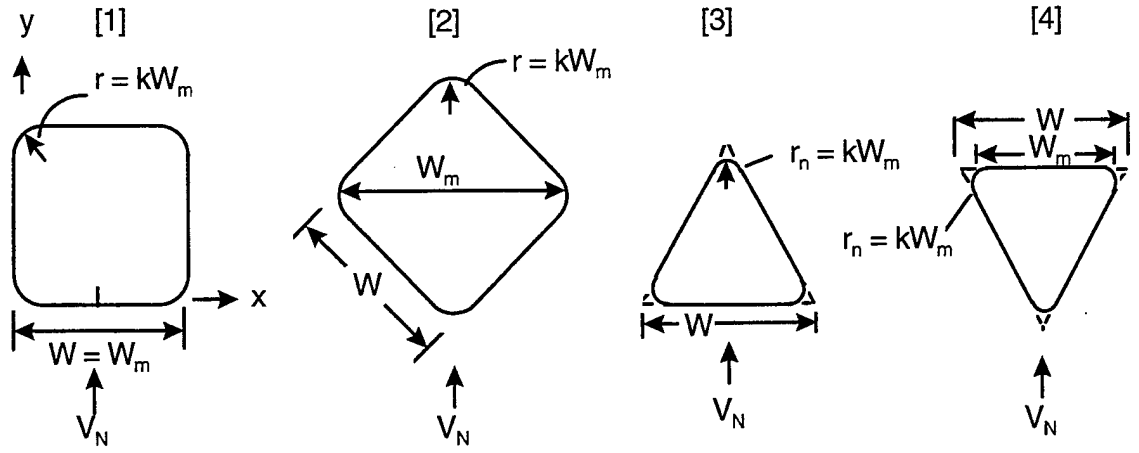

FIGURE A-1. ORIENTATIONS OF SQUARE AND TRIANGULAR CROSS SECTIONS FOR DERIVATION OF $(C_n/C_{n_o})_N$

To compute $(C_n/C_{n_o})_N$ requires a derivation of the crossflow drag coefficient for each of the four cases shown in Figure A-1 since

$$\left(\frac{C_n}{C_{n_o}}\right)_N = \left(\frac{C_d}{C_{d_c}}\right)_N \tag{A-1}$$

C_{d_c} of Equation (A-1) is the crossflow drag coefficient per unit length of a circular cylinder of the same cross-sectional area distribution as that of the noncircular cross section, whereas C_d is the crossflow drag coefficient of each of the shapes in Figure A-1 based on the maximum dimension normal to the velocity W_m. For the square at $\Phi = 0$ deg, $W_m = W$, whereas for all the other configurations W_m is a function of W and the amount of roundness of a corner, k. For flow over a circular cylinder, the Figure A-2 is useful in defining the geometrical variables and flow properties.

The drag per unit length is the force in the X direction, which is

$$\frac{D}{\ell} = 2r\int_0^{\pi/2}(P - P_\infty)\cos\theta\, d\theta \tag{A-2}$$

The drag can also be defined in terms of a drag coefficient as

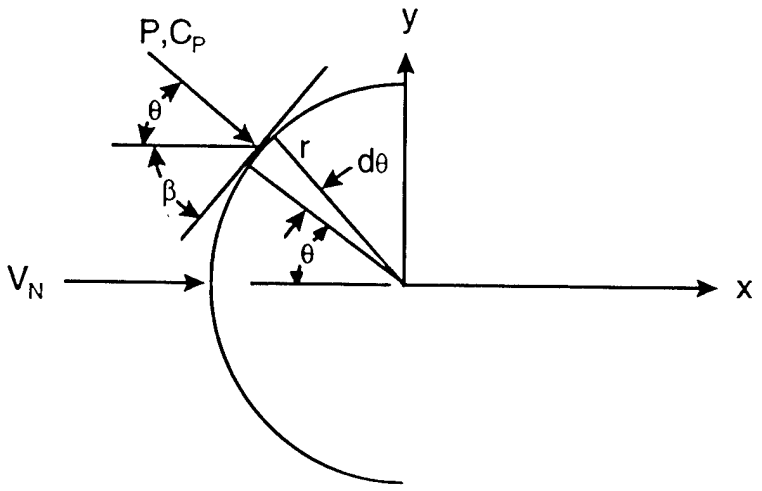

FIGURE A-2. DEFINITION OF FLOW VARIABLES USED IN DRAG INTEGRAL

$$\frac{D}{\ell} = C_D \, \tfrac{1}{2} \rho_\infty \, V_N^2 \, (2r) \tag{A-3}$$

Equating Equations (A-2) and (A-3) and solving for the drag coefficient per unit length, one obtains

$$C_{d_C} = \frac{C_D}{\ell} = \int_0^{\pi/2} \frac{P - P_\infty}{\tfrac{1}{2} \rho_\infty \, V_N^2} \cos \theta \, d\theta \tag{A-4}$$

Since

$$C_P = \frac{P - P_\infty}{\tfrac{1}{2} \, \rho_\infty \, V_N^2}$$

and by definition from modified Newtonian theory

$$C_P = C_{P_0} \sin^2 \beta$$

Equation (A-4) becomes

$$C_{d_C} = C_{P_O} \int_0^{\pi/2} \sin^2\beta \cos\theta \, d\theta \tag{A-5}$$

Since $\beta = \pi/2 - \theta$, Equation (A-5) becomes

$$C_{d_C} = C_{P_O} \int_0^{\pi/2} \cos^3\theta \, d\theta \tag{A-6}$$

Equation (A-6) becomes, upon integration,

$$C_{d_C} = \frac{2}{3} C_{P_O} \tag{A-7}$$

where C_{P_O} is the stagnation pressure coefficient defined by:

$$C_{P_O} = \frac{2}{\gamma M_\infty^2} \left\{ \left[\frac{(\gamma + 1) M_\infty^2}{2} \right]^{\frac{\gamma}{\gamma-1}} \left[\frac{\gamma + 1}{2\gamma M_\infty^2 - (\gamma - 1)} \right]^{\frac{1}{\gamma-1}} - 1 \right\} \tag{A-8}$$

Using this same process of the circular cylinder for configuration [1] of Figure A-1, the drag coefficient per unit length is

$$C_d = \frac{2}{W_m} \left[\int_0^{\frac{W_m - r}{2}} C_{P_O} \sin^2\delta \, dx + r \int_0^{\pi/2} C_{P_O} \cos^3\theta \, d\theta \right] \tag{A-9}$$

Note that $W_m = W$ for the square at $\Phi = 0$ deg roll. But δ in the first integral is $\pi/2$ since the surface is flat and normal to the velocity vector. Integration of Equation (A-9) yields:

$$C_d = \frac{2 C_{P_O}}{W_m} \left[\frac{W_m}{2} - \frac{r}{3} \right] \tag{A-10}$$

Defining $r = kW_m$, Equation (A-10) becomes

$$C_d = 2\, C_{P_o} \left[\frac{1}{2} - \frac{k}{3}\right] \tag{A-11}$$

Thus if k = 0, we have the square with no rounded corners and $C_d = C_{P_o}$, whereas if k = 0.5, we once again have a cylinder and C_d reduces to $C_{d_c} = (2/3)C_{P_o}$.

To obtain $(C_n/C_{n_o})_N$, it is necessary to find the diameter, d_{eq}, of the equivalent circular cross section. The area of the cross section in both sketches [1] and [2] of Figure A-1 is

$$A = W^2 \left[1 - k^2 (4 - \pi)\right] \tag{A-12}$$

The area of the circle is

$$A = \frac{\pi\, d_{eq}^2}{4} \tag{A-13}$$

Equating Equations (A-12) and (A-13) one obtains

$$d_{eq} = 2W \sqrt{\frac{1 - (4 - \pi)k^2}{\pi}} \tag{A-14}$$

Now referencing Equation (A-11) to d_{eq} versus W_m we have

$$C_d = 2C_{P_o} \left(\frac{1}{2} - \frac{k}{3}\right) \frac{W_m}{d_{eq}} \tag{A-15}$$

Then substituting Equations (A-14), (A-15), (A-7) into Equation (A-1) and simplifying, one obtains (where $W_m = W$ for the square at $\Phi = 0$ deg):

$$\left(\frac{C_n}{C_{n_o}}\right)_N = \frac{3}{2} \left(\frac{1}{2} - \frac{k}{3}\right) \sqrt{\frac{\pi}{1 - (4 - \pi)\, k^2}} \tag{A-16}$$

where $0 \le k \le 0.5$. At k = 0, the square cross section has no rounded corners and at k = 0.5, the square converts to a circle.

For the square oriented at 45 deg roll to the freestream (see sketch [2] of Figure A-1), the drag integral based on the Newtonian pressure coefficient is:

$$C_d = \frac{2C_{P_o}}{W_m}\left[r\int_0^{\pi/2}\cos^3\theta\, d\theta + \int_{\frac{r}{\sqrt{2}}}^{W_m/2-r+r/\sqrt{2}}\sin^2\delta\, dx\right] \tag{A-17}$$

W_m of Equation (A-17) is the maximum cross sectional width of the square normal to the flow. For no rounded corners, it is $\sqrt{2}$ W, whereas for a circle $W_m = W = 2r$. Integration and simplification of Equation (A-17), where $r = kW_m$, yields

$$C_d = 2C_{P_o}\left[\frac{1}{4} + \frac{k}{6}\right] \tag{A-18}$$

Notice that when $k = 0$, Equation (A-18) gives a C_d of half that of Equation (A-11). However, basing Equation (A-18) on the equivalent circular diameter given by Equation (A-14) yields

$$C_d = 2C_{P_o}\left[\frac{1}{4} + \frac{k}{6}\right]\frac{W_m}{d_{eq}} \tag{A-19}$$

Then, the value of the local normal force coefficient defined by Equation (A-1) becomes

$$(C_n/C_{n_o})_N = \frac{3}{2}\left[\frac{1}{4} + \frac{k}{6}\right]\sqrt{\frac{\pi}{1 - (4 - \pi)\,k^2}}\left(\frac{W_m}{W}\right) \tag{A-20}$$

Since W_m for the square at $\Phi = 45$ deg varies as,

$$W_m = W\left[\sqrt{2}\,(1 - 2k) + 2k\right] \tag{A-21}$$

Equation (A-20) can be written as:

$$(C_n/C_{n_o})_N = \frac{3}{2}\left[\frac{1}{4} + \frac{k}{6}\right]\sqrt{\frac{\pi}{1 - (4 - \pi)\,k^2}}\left[\sqrt{2}\,(1 - 2k) + 2k\right] \tag{A-22}$$

The value of $(C_n/C_{n_O})_N$ thus varies between 0.94 for no rounded corner to 1.0 for a circle according to Newtonian theory. It should also be pointed out that for a given value of r for case [1] and [2] of Figure A-1, the value of k will change since $k = r/W_m$ and W_m is different for the two cases.

The Newtonian drag coefficient of the third case in Figure A-1 is identical to that of the first case. Hence, Equation (A-11) applies to this case. However, the equivalent diameter is different due to the triangular shape. The cross sectional area of both the cases [3] and [4] of Figure A-1 is

$$A = W^2 \left\{ \left(\frac{\sqrt{3}}{4} \right) - \frac{k^2 (3\sqrt{3} - \pi)}{\left[1 + 2k (\sqrt{3} - 1)\right]^2} \right\} \tag{A-23}$$

Equating Equation (A-23) to Equation (A-13) and solving for d_{eq} we obtain

$$d_{eq} = \frac{2W}{\sqrt{\pi}} \left\{ \frac{\sqrt{3}}{4} - \frac{k^2 (3\sqrt{3} - \pi)}{\left[1 + 2k (\sqrt{3} - 1)\right]^2} \right\}^{1/2} \tag{A-24}$$

Since $W = W_m \left[1 + 2k (\sqrt{3} - 1)\right]$, Equation (A-24) can also be written as

$$d_{eq} = 2W_m \frac{\left[1 + 2k (\sqrt{3} - 1)\right]}{\sqrt{\pi}} \left\{ \frac{\sqrt{3}}{4} - \frac{k^2 (3\sqrt{3} - \pi)}{\left[1 + 2k (\sqrt{3} - 1)\right]^2} \right\}^{1/2} \tag{A-25}$$

Thus, the crossflow drag coefficient per unit length of configuration [3] of Figure A-1, based on the reference diameter d_{eq} is

$$C_d = 2C_{P_O} \left[\frac{1}{2} - \frac{k}{3} \right] \frac{W_m}{d_{eq}}$$

$$= C_{P_O} \left[\frac{1}{2} - \frac{k}{3} \right] \frac{\sqrt{\pi}}{1 + 2k (\sqrt{3} - 1)} \left\{ \frac{\sqrt{3}}{4} - \frac{k^2 (3\sqrt{3} - \pi)}{\left[1 + 2k (\sqrt{3} - 1)\right]^2} \right\}^{-1/2} \tag{A-26}$$

Finally, the local normal force coefficient ratio may be found by utilizing Equations (A-1), (A-7) and (A-26) to obtain:

$$(C_n/C_{n_o})_N = \frac{3}{2}\left[\frac{1}{2} - \frac{k}{3}\right] \frac{\sqrt{\pi}}{1 + 2k(\sqrt{3} - 1)} \left\{\frac{\sqrt{3}}{4} - \frac{k^2(3\sqrt{3} - \pi)}{\left[1 + 2k(\sqrt{3} - 1)\right]^2}\right\}^{-1/2} \quad \text{(A-27)}$$

Equation (A-27) varies between just over 2.0 at k = 0 to a value of 1.0 when k = 0.5.

The local crossflow drag coefficient integral for the fourth case of Figure A-1 is:

$$C_d = \frac{2C_{P_o}}{W_m}\left[r\int_0^{\frac{\pi}{2}} \cos^3\theta\, d\theta + \int_{\frac{r\sqrt{3}}{2}}^{\frac{W_m}{2} + \frac{r\sqrt{3}}{2} - r} \sin^2\delta\, dx\right] \quad \text{(A-28)}$$

For this configuration, δ is a constant value of 30 deg all along the flat side of the triangle that the flow touches. As a result, Equation (A-28) becomes upon integration:

$$C_d = \frac{2C_{P_o}}{W_m}\left[\frac{W_m}{8} + \frac{5r}{12}\right] \quad \text{(A-29)}$$

Since $r = kW_m$ and d_{eq} is defined by Equation (A-25), Equation (A-29) can be rewritten, when based on the equivalent diameter of a circular body as

$$C_d = C_{P_o}\left[\frac{1}{4} + \frac{5k}{6}\right] \frac{\sqrt{\pi}}{2[1 + 2k(\sqrt{3} - 1)} \left\{\frac{\sqrt{3}}{4} - \frac{k^2(3\sqrt{3} - \pi)}{\left[1 + 2k(\sqrt{3} - 1)\right]^2}\right\}^{-1/2} \quad \text{(A-30)}$$

The local Newtonian normal force coefficient ratio for case [4] of Figure A-1 then becomes

$$\left(\frac{C_n}{C_{n_o}}\right)_N = \frac{3}{4}\left[\frac{1}{4} + \frac{5k}{6}\right] \frac{\sqrt{\pi}}{1 + 2k(\sqrt{3} - 1)} \left\{\frac{\sqrt{3}}{4} - \frac{k^2(3\sqrt{3} - \pi)}{\left[1 + 2k(\sqrt{3} - 1)\right]^2}\right\}^{-1/2} \quad \text{(A-31)}$$

Equation (A-31) varies from a value of about 0.5 when k = 0 to a value of 1.0 when k = 0.5.

APPENDIX B

SCALING CONSIDERATIONS BASED ON SLENDER BODY THEORY (SBT)

In the normal course of calculating aerodynamics of a given configuration, understanding the effects of scale are important. For example, when one tests a model in the wind tunnel, generally that model is geometrically scaled in terms of its configuration shape so aerodynamics will be approximately the same. However, experience has taught us that boundary layer transition naturally occurs on a smooth wind tunnel model at a much higher value than on a rougher flight vehicle. This knowledge, along with tunnel test conditions, allows us to predict aerodynamics on a scaled wind tunnel model and indicate the approximate difference to a flight vehicle model. The major difference is generally a slightly different value of axial force coefficient.

The matter of scaling is quite important in development of the aerodynamic prediction code for nonaxisymmetric bodies. The reason is that we are trying to accomplish this task based on an equivalent axisymmetric body. Secondly, the scaling issue is important because in some of the literature, tests are conducted on noncircular cross section bodies with a constant dimension and compared to that on a circular cylinder with a diameter equal to that same dimension. Fin shape is generally the same for these cases. Other tests have been conducted on noncircular bodies where the body cross section area is held constant and equal to that of a circular body. Again fin shape is generally constant. The question arises as to whether one can use the same overall approach to calculate aerodynamics of these two cases and if so, are there scaling factors that need to be considered to compare one case to another.

To investigate first order effects of scale on linear normal force of bodies and wing-body combinations, slender body theory (SBT) is an excellent method to consider. References B-1 and B-2 were the primary materials used for this analysis. SBT basically assumes the configuration is fairly smooth and slender with no discontinuities along the body surface. This type of contour will then minimize the perturbation in the freestream due to the presence of the body. It allows the equations of motion to be linearized as a result. Generally, the flow is assumed to be isentropic due to only weak shock waves being created by this slender, smooth body. While these assumptions seem rather strong, some good qualitative insight in terms of aerodynamic trends can be obtained, although the magnitudes of the numbers can be in substantial error. SBT is quite useful for the purpose of investigating the issues addressed here concerning scaling.

The normal force of a given wing-body configuration is given by

$$N = N_B + N_{W(B)} + N_{B(W)} \tag{B-1}$$

where N_B is the normal force of the body alone, $N_{W(B)}$ is the normal force on the wing in presence of the body and $N_{B(W)}$ is the additional normal force on the body caused by the presence of the wing. Figure B-1 is a sketch of a typical wing body showing the important configuration dimensions.

SBT defines the body alone lift as simply that due to the nose with no contribution from the afterbody. This value is

$$N_B = 2\alpha Q \pi r_b^2 \tag{B-2}$$

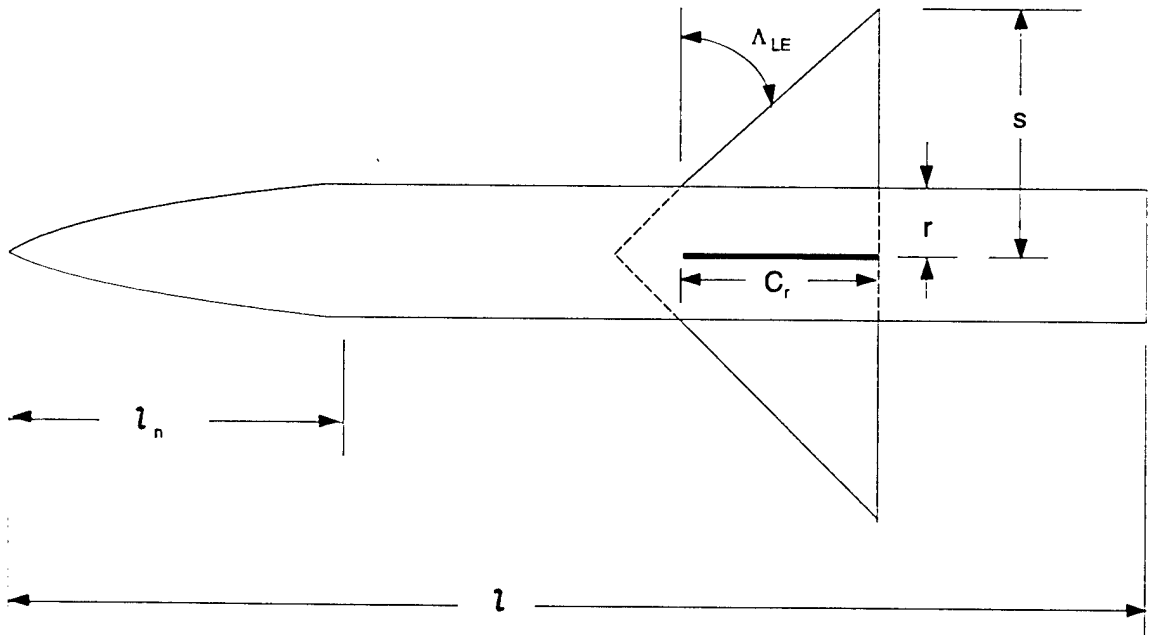

FIGURE B-1. CIRCULAR WING-BODY GEOMETRICAL PARAMETERS

Here r_b is the radius of the base of the configuration. SBT also assumes the wings extend to the mid body. The normal force of the last two terms is

$$N_{W(B)} + N_{B(W)} = [K_{W(B)} + K_{B(W)}] N_W \tag{B-3}$$

also

$$K_{W(B)} + K_{B(W)} = \left(1 + \frac{r}{s}\right)^2 \tag{B-4}$$

and

$$N_W = 2\pi\alpha Q(s - r)^2 \tag{B-5}$$

Substituting (B-2), (B-3), (B-4), (B-5) into Equation (B-1) and dividing through by QS_{ref} to put Equation (B-1) in the form of a coefficient, one obtains:

$$C_N = \frac{2\alpha\pi}{S_{ref}} \underbrace{\{r^2}_{\text{body term}} + \underbrace{s^2 [1 - 2(r/s)^2 + (r/s)^4]\}}_{\text{wing-body term}} \tag{B-6}$$

If one combines the two terms in Equation (B-6), one obtains the usual expression given in References B-1 and B-2 for total configuration normal force coefficient as

$$C_N = \frac{2\pi\alpha s^2}{S_{ref}} \left[1 - (r/s)^2 + (r/s)^4\right] \tag{B-7}$$

using body cross section area as S_{ref}. Equation (B-7) can be further written as

$$C_N = 2\alpha \left[\left(\frac{s}{r}\right)^2 + (r/s)^2 - 1\right] \tag{B-8}$$

Equation (B-8) gives us some very simple and important information concerning scaling. It basically says that if you take two different wing-body configurations which both obey the slenderness requirements, the normal force coefficient of the two configurations will be the same at any Mach number for a given angle of attack if r/s of the two configurations are equal.

The question we now need to address is if one can use the information given by Equation (B-6) to help one answer some of the scaling issues associated with creating an axisymmetric body to calculate aerodynamics of a noncircular cross section body. To address this question, several examples will be considered. The first example is illustrated in Figure B-2. This figure maintains a body circular diameter that is equal to one side of the square. Thus, r/s for the two cases is the same. Referring back to Equation (B-6) where the body and wing-body contributions have been separated, the implication of this analogy is that the wing-body term will remain constant for the two cases in Figure B-2 since r/s is the same. However, the body cross sectional area of the

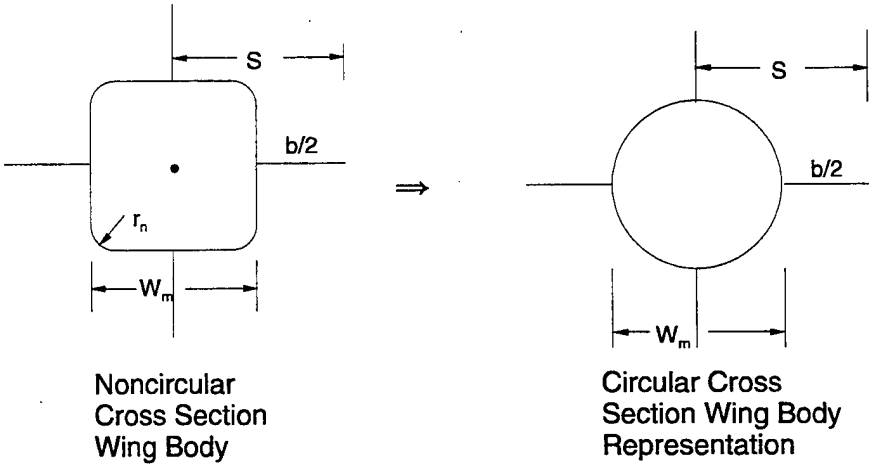

FIGURE B-2. EXAMPLE OF A CIRCULAR WING BODY REPRESENTATION OF A NONCIRCULAR CONFIGURATION WHERE BODY DIAMETER IS MAXIMUM DIMENSION OF NONCIRCULAR SHAPE

noncircular case is different from the circular case. Thus, the first term of Equation (B-6) must be multiplied by this ratio. In other words, the aerodynamics of the noncircular cross section of Figure B-2 can be estimated using the circular cross section case of Figure B-2 and Equation (B-6) as

$$C_N = \frac{2\alpha\pi}{A_C}\left\{\left(\frac{A_{NC}}{A_C}\right) r^2 + s^2\left[1 - 2(r/s)^2 + (r/s)^4\right]\right\} \qquad \text{(B-9)}$$

Using this information for the aeroprediction code, this says we should multiply the body term by (A_{NC}/A_C) if we represented it by an equivalent circular body of diameter W. This applies also to comparing predictions to wind tunnel data which were taken in this manner. Note that Figure 13 of the main text is already based on a configuration of diameter equal to that of one side of a square or triangle. Hence, this figure can be used directly without any scaling factors for the case shown in Figure B-2.

A second example of estimating aerodynamics of a noncircular body by a circular body is illustrated in Figure B-3. Here the circular body diameter is equal to the equivalent diameter of a circular cylinder of the same cross sectional area of the noncircular shape. For this case, the body contribution of Equation (B-6) has a factor of one since the cross sectional area of the circular and noncircular shapes are the same. However, the r/s values of these two cases are different. This means that the wing-body contribution of Equation (B-6) for the squares or triangles must be multiplied by the factor

$$\frac{\left(\frac{s}{r}\right)^2_{eq}\left[1 - 2\left(\frac{r}{s}\right)^2_{eq} + \left(\frac{r}{s}\right)^4_{eq}\right]}{\left(\frac{s}{r}\right)^2_{1}\left[1 - 2\left(\frac{r}{s}\right)^2_{1} + \left(\frac{r}{s}\right)^4_{1}\right]} \qquad \text{(B-10)}$$

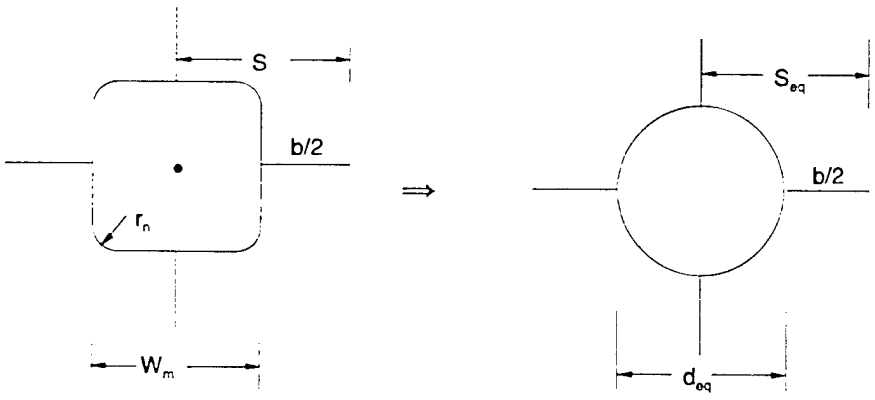

FIGURE B-3. EXAMPLE OF A CIRCULAR WING BODY REPRESENTATION OF A NONCIRCULAR CONFIGURATION WHERE BODY DIAMETER IS EQUIVALENT DIAMETER

Note here that $(r/s)_1$ is relative to the noncircular body where the fins are located. This factor from Equation (B-10) must be used in conjunction with Figure 13 of the main text, which was based on wind tunnel data taken on a configuration of side W and normalized by the circular cylinder value of 2.0. On the other hand, for the elliptical $K_{W(B)}$ values of Figure 10A, the factor from Equation (B-10) is not needed. This is because Figure 10A was derived based on a body of diameter d_{eq}. Note that the values of $K_{W(B)}$ in Figure 10A are much higher than those in Figure 13. This is partially due to the fact that the aerodynamics of an ellipse were based on d_{eq}, and $K_{W(B)}$ of Figure 13 was derived on that basis.

The above analysis has shown that even if aerodynamics are estimated based on some reference diameter, they can be compared to wind tunnel data based on a different diameter by using the SBT scaling factors (SBTSF) of Equation (B-9) for the body or Equation (B-10) for the wing-body.

As an example application of the Equation (B-10) scaling factors, consider the configuration of Figure B-4. Appendix A gives the equations for $d_{eq}(=2r_{eq})$ and $W_m(=2r_1)$ for the triangle as a function of W and the corner rounding parameter k. For simplicity, let's assume the corner is sharp so k = 0 and W_m = W. For this case, d_{eq} = 0.743W. Also, for simplicity, assume W = b. Then, applying Equation (B-10) to Figure B-4 (since here we are keeping the area of the circle the same as the area of the triangle), one obtains for the SBTSF

$$\text{SBTSF} = \frac{\left(\dfrac{0.377W + W/2}{0.743W}\right)^2}{\left(\dfrac{W/2 + W/2}{W}\right)^2} \frac{\left[1 - 2\left(\dfrac{0.377W}{0.377W + W/2}\right)^2 + \left(\dfrac{0.377W}{0.377W + W/2}\right)^4\right]}{\left[1 - 2\left(\dfrac{W/2}{W/2 + W/2}\right)^2 + \left(\dfrac{W/2}{W/2 + W/2}\right)^4\right]}$$

$$= \frac{1.39}{1} \frac{[1 - 0.37 + 0.034]}{[1 - 0.5 + 0.0625]} = 1.64$$

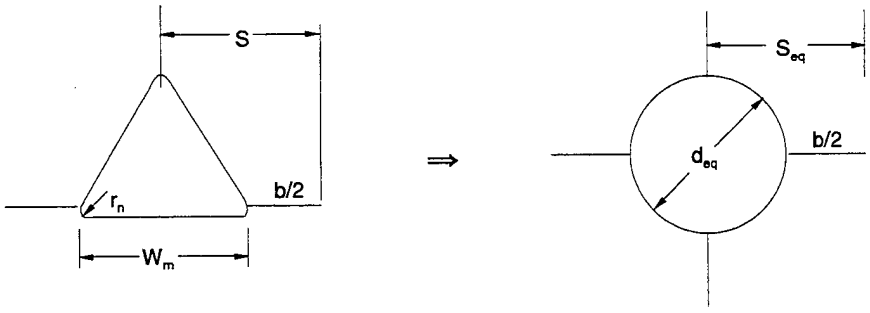

FIGURE B-4. EXAMPLE APPLICATION FOR SBTSF OF EQUATION B-10

Now referring to Figure 13, the value of $[K_{W(B)}]_{NC}/[K_{W(B)}]_C$ at k = 0 for the triangle shape is about 0.75. Multiplying this value by 1.64, one obtains $[K_{W(B)}]_{NC}/[K_{W(B)}]_C = 1.23$. This says that when we take a configuration such as the triangular shape of Figure B-4, represent it by a circular shape of diameter d_{eq}, keep the fins constant, the value of the circular $K_{W(B)}$ must be increased by 23 percent. Notice that had we represented the triangular shape by a circular shape of diameter W, the wing-body SBTSF is one, since r/s of these two shapes is the same. However, the body term must be multiplied by $\left(\frac{0.743W}{W}\right)^2$ or 0.522. Also, $K_{W(B)}$ of Figure 13 is applied directly. Also, the value of Equation (B-10) is a function of b/2, k, configuration shape as well as $(r/s)_1$ and $(r/s)_{eq}$. A single case was chosen where values of these parameters were selected for illustration purposes.

To summarize, if we define $(SBTSF)_1$ and $(SBTSF)_2$ as that associated with the body and wing-body normal force components respectively, then one can write

$$C_N = C_{N_B}(SBTSF)_1 + \left[C_{N_{W(B)}} + C_{N_{B(W)}}\right](SBTSF)_2 \tag{B-11}$$

If the aerodynamics are based on $\frac{\pi W^2}{4}$ as a reference area and wind tunnel data was taken that way, then

$$\begin{aligned}(SBTSF)_1 &= \left(\frac{d_{eq}}{W}\right)^2 \\ (SBTSF)_2 &= 1\end{aligned} \tag{B-12}$$

On the other hand, if the aerodynamics are based on $\frac{\pi d_{eq}^2}{4}$ as a reference area and wind tunnel data was taken that way, then

$$\begin{aligned}(SBTSF)_1 &= 1 \\ (SBTSF)_2 &= \frac{\left(\frac{s}{r}\right)_{eq}^2\left[1 - 2\left(\frac{r}{s}\right)_{eq}^2 + \left(\frac{r}{s}\right)_{eq}^4\right]}{\left(\frac{s}{r}\right)_1^2\left[1 - 2\left(\frac{r}{s}\right)_1^2 + \left(\frac{r}{s}\right)_1^4\right]}\end{aligned} \tag{B-13}$$

Finally, if the aerodynamics are based on $\frac{\pi d_{eq}^2}{4}$ and we wish to compare these aerodynamics to those that are based on a reference area of $\frac{\pi W^2}{4}$ (where wind tunnel data was also taken based on $\frac{\pi W^2}{4}$), then

$$(SBTSF)_1 = \left(\frac{d_{eq}}{W}\right)^2$$

$$(SBTSF)_2 = \frac{\left(\frac{s}{r}\right)^2_{eq}\left[1 - 2\left(\frac{r}{s}\right)^2_{eq} + \left(\frac{r}{s}\right)^4_{eq}\right]}{\left(\frac{s}{r}\right)^2_{1}\left[1 - 2\left(\frac{r}{s}\right)^2_{1} = \left(\frac{r}{s}\right)^4_{1}\right]} \qquad \text{(B-14)}$$

Equations (B-13) and (B-14) are needed for square and trianglar cross section shapes because $K_{W(B)}$ (Figure 13) was derived on the basis of a body with diameter W. Equations (B-13) and (B-14) are not needed for elliptical shapes because $K_{W(B)}$ (Figure 10A) was derived on the basis of a body with diameter d_{eq}. If one were interested in deriving aerodynamics of an ellipse based on $\frac{\pi W^2}{4}$ versus $\frac{\pi d_{eq}^2}{4}$, then new SBTSFs would be needed for this case in analogy to those for square and triangular shapes.

REFERENCES

B-1. Ashley, H. and Landahl, M., *Aerodynamics of Wings and Bodies*, Addison-Wesley Publishing Company, Inc., Reading, MA, Copyright 1965.

B-2. Nielsen, J. N., *Missile Aerodynamics*, NEAR Inc., Mountain View, CA, 1988.

DISTRIBUTION

DOD ACTIVITIES (CONUS)

		Copies
ATTN	CODE 35 (ZIMET)	1
	CODE 351 (SIEGEL)	1
	CODE 351 (CHU)	1
	CODE 332FD (LEKOUDIS)	1

CHIEF OF NAVAL RESEARCH
BALLSTON CENTRE TOWER ONE
800 NORTH QUINCY ST
ARLINGTON VA 22217-5660

ATTN	CODE 474T6OD (LOFTUS)	1
	CODE 4732HOD (SMITH)	1
	CODE 4732HOD (LAMBERT)	1
	CODE 473COOD (PORTER)	1
	CODE 47311OD (HOUSH)	1
	CODE 47311OD (GLEASON)	1
	CODE 47311OD (VAN DYKEN)	1
	CODE 4722EOD (JETER)	1
	TECHNICAL LIBRARY	1

COMMANDER
NAVAL AIR WARFARE CENTER
WEAPONS DIVISION
1 ADMINISTRATION CIRCLE
CHINA LAKE CA 93555-6001

ATTN	TECHNICAL LIBRARY	1
	G RUDACILLE PMS 38012 7	1

COMMANDER
NAVAL SEA SYSTEMS COMMAND
2531 JEFFERSON DAVIS HWY
ARLINGTON VA 22242-5160

ATTN	AIR 53012D (JOHNSON)	1
	RM 904 JP 2	
	TECHNICAL LIBRARY	1

COMMANDER
NAVAL AIR SYSTEMS COMMAND
HEADQUARTERS
1421 JEFFERSON DAVIS HWY
ARLINGTON VA 22243-5120

ATTN	C KLEIN	1
	TECHNICAL LIBRARY	1

COMMANDER
NAVAL AIR WARFARE CENTER
WEAPONS DIVISION
521 9TH ST
POINT MUGU CA 93042-5001

ATTN	T C TAI	1
	M J MALIA	1
	TECHNICAL LIBRARY	1

COMMANDER
NAVAL SHIP RESEARCH AND
DEVELOPMENT CENTER
WASHINGTON DC 20034

ATTN	R M HOWARD	1
	TECHNICAL LIBRARY	1

SUPERINTENDENT
NAVAL POSTGRADUATE SCHOOL
1 UNIVERSITY CIRCLE
MONTEREY CA 93943-5001

ATTN	S GREENHALGH	1
	C REITZ	1
	TECHNICAL LIBRARY	1

COMMANDING OFFICER
NAVAL AIR WARFARE CENTER
AIRCRAFT DIVISION WARMINSTER
BOX 5152
WARMINSTER PA 18974-0591

ATTN	HEAD WEAPONS DEPT	1
	HEAD SCIENCE DEPT	1

SUPERINTENDENT
UNITED STATES NAVAL ACADEMY
121 BLAKE RD
ANNAPOLIS MD 21402-5000

ATTN	TECHNICAL LIBRARY	1

OFFICER IN CHARGE
NAVAL INTELLIGENCE SUPPORT CENTER
4301 SUITLAND ROAD
ALEXANDRIA VA 22217

DISTRIBUTION (Continued)

	Copies
ATTN DIAG DT 4T (PAUL MURAD) DIRECTOR DEFENSE INTELLIGENCE AGENCY WASHINGTON DC 20301	2
ATTN BRENT WAGGONER CODE 4072 BLDG 2540 NAVAL WEAPONS SUPPORT CENTER CRANE IN 47522-5000	1
ATTN CODE 5252P (KRAUSE) TECHNICAL LIBRARY COMMANDER INDIAN HEAD DIVISION NAVAL SURFACE WARFARE CENTER 101 STRAUSS AVE INDIAN HEAD MD 20640-5035	1 1
ATTN TECHNICAL LIBRARY COMMANDING GENERAL MARINE CORPS COMBAT DEVELOPMENT COMMAND 2048 SOUTH ST QUANTICO VA 22134-5129	1
ATTN E SEARS L E LIJEWSKI C COTTRELL TECHNICAL LIBRARY AFATL (ADLRA) (DLGC) EGLIN AFB FL 32542-5000	1 1 1 1 1
ATTN TECHNICAL LIBRARY USAF ACADEMY COLORADO SPRINGS CO 80912	1
ATTN TECHNICAL LIBRARY ADVANCED RESEARCH PROJECTS AGENCY DEPARTMENT OF DEFENSE WASHINGTON DC 20305	1
ATTN B BLAKE (BLD 146) J JENKINS (BLD 146) TECHNICAL LIBRARY COMMANDING OFFICER AFSC 2210 8TH STREET WRIGHT PATTERSON AFB OH 45433	1 1 1
ATTN EDWARD JENKINS NAIC TANW HQ NAIC TANW 4115 HEBBLE CREEK ROAD SUITE 28 WPAFB OH 45433-5623	1
ATTN J USSELTON W B BAKER JR TECHNICAL LIBRARY ARNOLD ENGINEERING DEVELOPMENT CENTER USAF TULLAHOMA TN 37389	1 1 1
ATTN H HUDGINS G FRIEDMAN TECHNICAL LIBRARY COMMANDING GENERAL ARRADCOM PICATINNY ARSENAL DOVER NJ 07801	1 1 1
ATTN C H MURPHY R PUHALLA JR W STUREK C NIETUBICZ A MIKHAIL P PLOSTINS TECHNICAL LIBRARY COMMANDING GENERAL BALLISTIC RESEARCH LABORATORY ABERDEEN PROVING GROUND ABERDEEN MD 21005-5066	1 1 1 1 1 1 1

DISTRIBUTION (Continued)

	Copies
ATTN CODE TNC (BLACKLEDGE)	1
RICH MATLOCK	1
DIRECTOR	
INTERCEPTOR TECHNOLOGY	
BALLISTIC MISSILE DEFENSE OFFICE	
THE PENTAGON	
WASHINGTON DC 20350	
ATTN SFAE SD ASP	1
SFAE SD HED	1
DEPUTY COMMANDER	
US ARMY STRATEGIC DEFENSE COMMAND	
P O BOX 1500	
HUNTSVILLE AL 35807-3801	
ATTN D WASHINGTON	1
W WALKER	1
R KRETZSCHMAR	1
D FERGUSON JR	1
COMMAND GENERAL	
US ARMY MISSILE COMMAND	
AMSMI RD SS AT	
REDSTONE ARSENAL AL 35898-5252	
DEFENSE TECHNICAL INFORMATION CENTER	
8725 JOHN J KINGMAN ROAD	
SUITE 0944	
FORT BELVOIR VA 22060-6218	2
DIRECTOR	
DEFENSE PRINTING SERVICE	
BLDG 176 WASHINGTON NAVY YARD	
901 M ST E	
WASHINGTON DC 20374-5087	1
ATTN CODE A76	
TECHNICAL LIBRARY	1
COMMANDING OFFICER	
COASTAL SYSTEMS STATION	
DAHLGREN DIVISION	
NAVAL SURFACE WARFARE CENTER	
6703 W HIGHWAY 98	
PANAMA CITY FL 32407-7001	

	Copies
ATTN DR P WEINACHT	1
AERODYNAMICS BRANCH	
PROPULSION AND FLIGHT DIV WTD	
AMSRL WT PB	
US ARMY RESEARCH LAB ABERDEEN	
PROVING GROUND MD 21005-5066	
ATTN GREGG ABATE	1
US AIR FORCE	
WRIGHT LABORATORY	
WL MNAA	
101 W EGLIN BLVD STE 219	
EGLIN AFB FL 32542	
ATTN JOHN GRAU	1
US ARMY ARDEC	
COMMANDER US ARMY ARDEC	
AMSTA AR AET A BLDG 3342	
PICATINNY ARSENAL NJ 07806-5000	
ATTN FRANK MACDONALD	1
NAWC CHINA LAKE	
COMMANDER	
CODE 473 20D	
NAVAIRWARCENNSDNDIV	
CHINA LAKE CA 93555	
ATTN MARK LAMBERT	1
NAWC	
CODE 4732HOD	
CHINA LAKE CA 93555	
ATTN MICHAEL MUSACHIO	1
DIRECTOR	
OFFICE OF NAVAL INTELLIGENCE	
4251 SUITLAND ROAD (ONI 2321)	
WASHINGTON DC 20395	
ATTN DR ALAN NICHOLSON MSC 5B	1
DEFENSE INTELLIGENCE AGENCY	
MISSILE AND SPACE INTELLIGENCE CTR	
REDSTONE ARSENAL AL 35898-5500	
ATTN EDWARD HERBERT	1
US ARMY MISSILE COMMAND	
AMSMI RD MG GA	
BLDG 5400 ROOM 250	
REDSTONE ARSENAL AL 35898	

DISTRIBUTION (Continued)

	Copies
ATTN PAUL KOLODZIEJ NASA AMES RESEARCH CENTER MS 234 1 MOFFETT FIELD CA 94035	1
ATTN LCDR T HARTLINE USNR R NR ONI 2109 NAVAL RESERVE UNIT 112 CRESTVIEW CIRCLE MADISON AL 35758	1
ATTN CODE 4732HOD DAVID HALL PROPULSION PERFORMANCE OFFICE NAVAL AIR WARFARE CTR WEAPONS DIV 1 ADMINISTRATIVE CIR CHINA LAKE CA 93555-6001	1
NON-DOD ACTIVITIES (CONUS)	
ATTN NEIL WALKER NICHOLS RESEARCH CORPORATION MS 912 P O BOX 400002 4040 S MEMORIAL PKWY HUNTSVILLE AL 35815-1502	1
THE CNA CORPORATION P O BOX 16268 ALEXANDRIA VA 22302-0268	1
ATTN GIFT AND EXCHANGE DIVISION LIBRARY OF CONGRESS WASHINGTON DC 20540	4
GIDEP OPERATIONS OFFICE CORONA CA 91720	1
ATTN TECHNICAL LIBRARY NASA AMES RESEARCH CENTER MOFFETT CA 94035-1099	1
ATTN C SCOTT D CURRY NASA JOHNSON SPACE CENTER HOUSTON TX 77058	1 1
ATTN TECHNICAL LIBRARY NASA WASHINGTON DC 20546	1
ATTN W C SAWYER B HENDERSON D MILLER J ALLEN F WILCOX TECHNICAL LIBRARY NASA LANGLEY RESEARCH CENTER HAMPTON VA 23365	1 1 1 1 1 2
ATTN D G MILLER (L 219) TECHNICAL LIBRARY LAWRENCE LIVERMORE NATIONAL LABORATORY EARTH SCIENCES DIVISION UNIVERSITY OF CALIFORNIA P O BOX 808 LIVERMORE CA 94551	1 1
ATTN W RUTLEDGE (1635) R LAFARGE R EISLER TECHNICAL LIBRARY SANDIA NATIONAL LABORATORY P O BOX 5800 ALBUQUERQUE NM 87185-5800	1 1 1 1
ATTN WALT GUTIERREZ SANDIA NATIONAL LABORATORIES MAIL STOP 0825 P O BOX 5800 ALBUQUERQUE NM 87185-0825	1
ATTN ASSISTANT DEFENSE COOPERATION ATTACHE EMBASSY OF SPAIN WASHINGTON DC 20016	1
DE/AVT DEFENSE EQUIPMENT STAFF BRITISH EMBASSY 3100 MASSACHUSETTS AVE NW WASHINGTON DC 20008-3688	1
ATTN ASO LO IS ISRAEL AIR FORCE LIAISON OFFICER 700 ROBBINS AVE PHILADELPHIA PA 19111	1

DISTRIBUTION (Continued)

	Copies
ATTN GERMAN MILITARY REP US OA GMR TRAFFIC AND TRANSPORTATION DIVISION 10 SERVICES ROAD DULLES INTERNATIONAL AP WASHINGTON DC 20041	1
ATTN PROF F R DEJARNETTE NORTH CAROLINA STATE UNIVERSITY DEPT OF MECHANICAL AND AEROSPACE ENGINEERING BOX 7921 RALEIGH NC 27695	1
ATTN PROF J A SCHETZ VIRGINIA POLYTECHNIC AND STATE UNIVERSITY DEPT OF AEROSPACE ENGINEERING BLACKSBURG VA 24060	1
ATTN J M WU C BALASUBRAMAYAN TECHNICAL LIBRARY THE UNIVERSITY OF TENNESSEE SPACE INSTITUTE TULLAHOMA TN 37388	1 1 1
ATTN R NELSON TECHNICAL LIBRARY UNIVERSITY OF NOTRE DAME DEPT OF AEROSPACE AND MECHANICAL ENGINEERING BOX 537 NOTRE DAME IN 46556	1 1
ATTN PROF F NELSON DEPT OF MECH AND AERO ENG UNIVERSITY OF MISSOURI ROLLA ROLLA MO 65401	1
ATTN DR DONALD SPRING AEROSPACE ENGINEERING DEPT AUBURN UNIVERSITY AL 36849-5338	1
ATTN ROBERT ENGLAR GEORGIA TECH RESEARCH INSTITUTE AEROSPACE SCIENCE AND TECHNOLOGY LAB ATLANTA GA 30332	1
ATTN E LUCERO L TISSERAND D FROSTBUTTER L PERINI TECHNICAL LIBRARY APPLIED PHYSICS LABORATORY JOHNS HOPKINS UNIVERSITY JOHNS HOPKINS ROAD LAUREL MD 20723-6099	1 1 1 1 1
ATTN B BROOKS R STANCIL R ELKINS LORAL VOUGHT SYSTEMS P O BOX 650003 M S EM 55 DALLAS TX 75265-0003	1 1 1
ATTN PROF J D ANDERSON DEPT OF AEROSPACE ENGINEERING UNIVERSITY OF MARYLAND COLLEGE PARK MD 20742	1
ATTN R CAVAGE ADVANCED SYSTEMS DESIGN DEPT 113 407 (GB14) ROCKWELL NORTH AMERICAN AIRCRAFT OPERATIONS P O BOX 3644 SEAL BEACH CA 90740-7644	1
ATTN TECHNICAL LIBRARY HUGHES MISSILE SYSTEMS COMPANY P O BOX 11337 BLDG 802 MS A1 OLD NOGALES HWY TUCSON AZ 83734-1337	1

DISTRIBUTION (Continued)

	Copies
ATTN M DILLENIUS NIELSEN ENGINEERING AND RESEARCH INC 526 CLYDE AVE MOUNTAIN VIEW CA 95043	1
ATTN J XERIKOS N CAMPBELL TECHNICAL LIBRARY MCDONNEL DOUGLAS ASTRONAUTICS CO (WEST) 5301 BOLSA AVE HUNTINGTON BEACH CA 92647	1 1 1
ATTN J WILLIAMS S VUKELICH J FIVEL R GERBSCH (CODE 1111041) TECHNICAL LIBRARY MCDONNELL DOUGLAS ASTRONAUTICS CO (EAST) BOX 516 ST LOUIS MO 63166-0516	1 1 1 1 1
ATTN TECHNICAL LIBRARY UNITED TECHNOLOGIES NORDEN SYSTEMS NORWALK CT 06856	1
ATTN T LUNDY D ANDREWS TECHNICAL LIBRARY LOCKHEED MISSILES AND SPACE CO INC P O BOX 1103 HUNTSVILLE AL 35807	1 1 1
ATTN W CHRISTENSON D WARNER ALLIANT TECHSYSTEMS INC 600 SECOND ST NE HOPKINS MN 55343	1 1
ATTN TECHNICAL LIBRARY B SALEMI J BOUDREAU RAYTHEON COMPANY MISSILE SYSTEMS DIVISION P O BOX 1201 TEWKSBURY MA 01876-0901	1 1 1
ATTN LLOYD PRATT AEROJET TACTICAL SYSTEMS CO P O BOX 13400 SACRAMENTO CA 95813	1
ATTN JOSEPH ANDRZEJEWSKI MEVATEC CORP 1525 PERIMETER PARKWAY SUITE 500 HUNTSVILLE AL 35806	1
ATTN DR G S SCHMIDT LORAL DEFENSE SYSTEMS 1210 MASSILLON ROAD AKRON OH 44315-0001	1
ATTN W NORDGREN 721 GOULD INC OSD 18901 EUCLID AVE CLEVELAND OH 44117	1
ATTN TECH LIBRARY AEROJET ELECTRONIC SYSTEMS P O BOX 296 III AZUSA CA 91702	1
ATTN P REDING G CHRUSCIEL TECHNICAL LIBRARY LOCKHEED MISSILES AND SPACE CO INC P O BOX 3504 SUNNYVALE CA 94088	1 1 1
ATTN K C LEE AEROTHERM CORP 580 CLYDE AVE MOUNTAIN VIEW CA 94043	1

DISTRIBUTION (Continued)

	Copies
ATTN TECH LIBRARY FMC NAVAL SYSTEMS DIV 4800 E RIVER ROAD MINNEAPOLIS MN 55421-1402	1
ATTN DORIA GLADSTONE BATTELLE MEMORIAL INSTITUTE COLUMBUS DIVISION 505 KING AVE COLUMBUS OH 43201-2693	1
ATTN JAMES SORENSON VINCENT ALLEN ORBITAL SCIENCES 3380 SOUTH PRICE ROAD CHANDLER AZ 85248	1 1
ATTN J FORKOIS KAMAN SCIENCES CORP 1500 GARDEN OF THE GODS ROAD P O BOX 7463 COLORADO SPRINGS CO 80933	1
ATTN RON EFROMSON MIT LINCOLN LABORATORY 244 WOOD STREET LEXINGTON MA 02173-0073	1
ATTN D J GIESE MAIL STOP 4C 61 BOEING DEFENSE AND SPACE GROUP P O BOX 3999 SEATTLE WA 98124-2499	1
ATTN BRIAN WALKUP HERCULES AEROSPACE PRODUCT CO ALLEGHANY BALLISTIC LAB ROCKET CENTER WV 26726	1
ATTN DR T LIN TRW ELECTRONICS AND DEFENSE SECTOR BLDG 527/RM 706 P O BOX 1310 SAN BERNADINO CA 92402	1
ATTN G VINCENT SPARTA INC 4901 CORPORATE DR HUNTSVILLE AL 35805	1
ATTN D P FORSMO TECHNICAL LIBRARY RAYTHEON COMPANY MISSILE SYSTEMS DIVISION HARTWELL RD BEDFORD MA 01730-2498	1 1
ATTN M S MILLER BRIAN EST DYNETICS INC P O DRAWER B HUNTSVILLE AL 35814-5050	1 1
ATTN H A MCELROY GENERAL DEFENSE CORP P O BOX 127 RED LION PA 17356	1
ATTN R SEPLAK BRUNSWICK CORP DEFENSE DIVISION 3333 HARBOR BLVD COSTA MESA CA 92628-2009	1
ATTN CAROL BUTLER OTI INTERNATIONAL 60 2ND ST SUITE 301 P O BOX 37 SHALIMAR FL 32579	1
ATTN ENGINEERING LIBRARY ARMAMENT SYSTEMS DEPT GENERAL ELECTRIC CO BURLINGTON VT 05401	1
ATTN TECHNICAL LIBRARY OAYNE AERONAUTICAL 2701 HARBOR DRIVE SAN DIEGO CA 92138	1

DISTRIBUTION (Continued)

	Copies
ATTN WILLIAM FACINELLI ALLIED SIGNAL P O BOX 22200 MS 1207 3B TEMPE AZ 85285	1
ATTN DR T P SHIVANANDA TRW BMD P O BOX 1310 SAN BERNADINO CA 92402-1313	1
ATTN T R PEPITONE AEROSPACE TECHNOLOGY INC P O BOX 1809 DAHLGREN VA 22448	1
ATTN ERIC MOORE MAIL STOP MER 24 1281 LOCKHEED SANDERS P O BOX 868 NASHUA NH 03061	1
ATTN DR BRIAN LANDRUM RI BLDG E33 PROPULSION RESEARCH CENTER UNIVERSITY OF ALABAMA HUNTSVILLE AL 35899	1
ATTN BRUCE NORTON MAIL STOP BL 1 RAYTHEON 100 VANCE TANK RD BRISTOL TN 37620	1
ATTN JIM ROBERTSON RESEARCH SOUTH INC 555 SPARKMAN DRIVE SUITE 818 HUNTSVILLE AL 35816-3423	1
ATTN BOB WHYTE ARROW TECH ASSOCIATES INC 1233 SHELBURNE ROAD D8 SO BURLINGTON VT 05403	1
ATTN JUAN AMENABAR SAIC 4001 NORTH FAIRFAX DRIVE STE 800 ARLINGTON VA 22209	1
ATTN TECHNICAL LIBRARY TELEDYNE RYAN AERONAUTICAL 2701 HARBOR DRIVE SAN DIEGO CA 92138	1
ATTN DR KIRIT PATEL SVERDRUP TECHNOLOGY INC TEAS GROUP BLDG 260 P O BOX 1935 EGLIN AFB FL 32542	1
ATTN FRANK LANGHAM MICRO CRAFT TECHNOLOGY 740 4TH ST MS 6001 ARNOLD AFB TN 37389	1
ATTN LAURA AYERS DELTA RESEARCH INC 315 WYNN DRIVE SUITE 1 HUNTSVILLE AL 35805	1
ATTN BRIAN BENNETT MCDONNELL DOUGLAS MC 064 2905 P O BOX 516 ST LOUIS MO 63166-0516	1
ATTN THOMAS FARISS LOCKHEED SANDERS P O BOX 868 MER24 1206 NASHUA NH 03061-0868	1
ATTN COREY FROST LOCKHEED MISSILES & SPACE CO INC P O BOX 070017 6767 OLD MADISON PIKE SUITE 220 HUNTSVILLE AL 35807	1

DISTRIBUTION (Continued)

	Copies
ATTN JEFFREY HUTH KAMAN SCIENCES CORPORATION 2560 HUNTINGTON AVE ALEXANDRIA VA 22303	1
ATTN WILLIAM JOLLY KAMAN SCIENCES 600 BLVD SOUTH SUITE 208 HUNTSVILLE AL 35802	1
ATTN STEPHEN MALLETTE KBM ENTERPRISES 15980 CHANEY THOMPSON RD HUNTSVILLE AL 35803	1
ATTN DONALD MOORE NICHOLS RESEARCH CORPORATION 4040 SOUTH MEMORIAL PARKWAY P O BOX 400002 MS 920C HUNTSVILLE AL 35815-1502	1
ATTN JAY NARAIN LOCKHEED MISSILES & SPACE CO P O BOX 3504 DEPT 81 10 BLDG 157 5E FAE 1 SUNNYVALE CA 94088-3504	1
ATTN DAVID RESSLER TRW BALLISTIC MISSILES DIV MS 953 2420 P O BOX 1310 SAN BERNARDINO CA 92402	1
ATTN MARK SWENSON ALLIANT TECHSYSTEMS MN11 262B 600 SECOND STREET NE HOPKINS MN 55343	1
ATTN JOHN SUN NORTHROP GRUMMAN CORPORATION 750 LYNNMERE DRIVE THOUSAND OAKS CA 91360	1
ATTN HARRY AULTMAN COLEMAN RESEARCH CORP 6820 MOQUIN DRIVE HUNTSVILLE AL 35806	1
ATTN SCOTT ALLEN ALLEN AERO RESEARCH 431 E SUNNY HILLS RD FULLERTON CA 92635	1
ATTN DARRYL HALL SAIC 997 OLD EAGLE SCHOOL RD SUITE 215 WAYNE PA 19087-1803	1
ATTN PETER ALEXANDER MCDONNELL DOUGLAS AEROSPACE 689 DISCOVERY DRIVE MS 11A1 HUNTSVILLE AL 35806	1
ATTN SAMUEL HICKS III TEXAS INSTRUMENTS 6600 CHASE OAKS BLVD MS 8490 PLANO TX 75086	1
ATTN BARRY LINDBLOM ALLIANT DEFENSE ELECTRONICS SYSTEMS INC P O BOX 4648 CLEARWATER FL 34618	1
ATTN DR SHIN CHEN THE AEROSPACE CORP M4 967 P O BOX 92957 LOS ANGELES CA 90009	1
ATTN ROBERT ACEBAL SAIC 1225 JOHNSON FERRY RD SUITE 100 MARIETTA GA 30068	1

DISTRIBUTION (Continued)

	Copies
ATTN EUGENE HART SYSTEM PLANNING CORP 1000 WILSON BLVD ARLINGTON VA 22209	1
ATTN ELAINE POLHEMUS ROCKWELL AUTONETICS & MISSILE SYSTEMS DIVISION D611 DL23 1800 SATELLITE BLVD DULUTH GA 30136	1
ATTN MICHAEL GLENN TASC 1992 LEWIS TURNER BLVD FT WALTON BEACH FL 32547	1
ATTN ROBERT ROGER ADAPTIVE RESEARCH 4960 CORPORATE DRIVE SUITE 100 A HUNTSVILLE AL 35805-6229	1
ATTN STEVEN MARTIN SYSTEMS ENGINEERING GROUP INC 9841 BROKEN LAND PARKWAY SUITE 214 COLUMBIA MD 21046-1120	1
ATTN C W GIBKE LOCKHEED MARTIN VOUGHT SYSTEMS MS SP 72 P O BOX 650003 DALLAS TX 75265-0003	1
ATTN CHRIS HUGHES EDO GOVERNMENT SYSTEMS DIV 14 04 111TH ST COLLEGE POINT NY 11356	1
ATTN DANIEL LESIEUTRE NIELSEN ENGINEERING & RES INC 526 CLYDE AVENUE MOUNTAIN VIEW CA 94043-2212	1
ATTN CARL HILL FRANCIS PRIOLO STANDARD MISSILE COMPANY LLC 1505 FARM CREDIT DRIVE SUITE 600 MCLEAN VA 22102	1 1
ATTN THOMAS LOPEZ COLEMAN RESEARCH CORP 990 EXPLORER BLVD HUNTSVILLE AL 35806	1
ATTN JENNIE FOX LOCKHEED MARTIN VOUGHT SYSTEMS P O BOX 650003 MS EM 55 DALLAS TX 75265-0003	1
ATTN JOHN BURKHALTER AUBURN UNIVERSITY 211 AEROSPACE ENGR BLDG AUBURN UNIVERSITY AL 36849	1
ATTN DR MAX PLATZER NAVAL POSTGRADUATE SCHOOL DEPT OF AERONAUTICS & ASTRONAUTICS CODE AA PL MONTEREY CA 93943	1
ATTN MIKE DANGELO MIT LINCOLN LABORATORY 1745 JEFFERSON DAVIS HWY 1100 ARLINGTON VA 22202	1
ATTN RICHARD HAMMER JOHNS HOPKINS APPLIED PHYSICS LAB JOHNS HOPKINS ROAD LAUREL MD 20723-6099	1

DISTRIBUTION (Continued)

NON-DOD ACTIVITIES (EX-CONUS)

	Copies
ATTN LOUIS CHAN INSTITUTE FOR AEROSPACE RESEARCH NATIONAL RESEARCH COUNSIL MONTREAL RD OTTAWA ONTARIO CANADA K1A0R6	1
ATTN H B ASLUND SAAB MILITARY AIRCRAFT 581 88 LINKOEPING SWEDEN	1
ATTN A BOOTH BRITISH AEROSPACE DEFENCE LTD MILITARY AIRCRAFT DIVISION WARTON AERODROME WARTON PRESTON LANCASHIRE PR4 1AX UNITED KINGDOM	1
ATTN R CAYZAC GIAT INDUSTRIES 7 ROUTE DE GUERCY 18023 BOURGES CEDEX FRANCE	1
ATTN MAJ F DE COCK ECOLE ROYALE MILITAIRE 30 AV DE LA RENAISSANCE 1040 BRUXELLES BELGIUM	1
ATTN J EKEROOT BOFORS MISSILES 691 80 KARLSKOGA SWEDEN	1
ATTN CH FRANSSON NATIONAL DEFENCE RESEARCH ESTABLISHMENT DEPT OF WEAPON SYSTEMS EFFECTS AND PROTECTION KARLAVAGEN 106B 172 90 SUNDBYBERG SWEDEN	1
ATTN M HARPER BOURNE DEFENCE RESEARCH AGENCY Q134 BUILDING RAE FARNBOROUGH HAMPSHIRE QU14 6TD UNITED KINGDOM	1
ATTN A H HASSELROT FFA P O BOX 11021 161 11 BROMMA SWEDEN	1
ATTN B JONSSON DEFENCE MATERIAL ADMINISTRATION MISSILE TECHNOLOGY DIVISION 115 88 STOCKHOLM SWEDEN	1
ATTN P LEZEAUD DASSAULT AVIATION 78 QUAI MARCEL DASSAULT 92214 SAINT CLOUD FRANCE	1
ATTN J LINDHOUT N L R ANTHONY FOKKERWEG 2 1059 CM AMSTERDAM THE NETHERLANDS	1
ATTN A MICKELLIDES GEC MARCONI DEFENCE SYSTEMS LTD THE GROVE WARREN LANE STANMORE MIDDLESEX UNITED KINGDOM	1
ATTN K MOELLER BODENSEEWERK GERAETETECHNIK GMBH POSTFACH 10 11 55 88641 UBERLINGEN GERMANY	1

DISTRIBUTION (Continued)

	Copies
ATTN G MOSS ROYAL MILITARY COLLEGE AEROMECHANICAL SYSTEMS GROUP SHRIVENHAM SWINDON WILTS SN6 8LA UNITED KINGDOM	1
ATTN RIBADEAU DUMAS MATRA DEFENSE 37 AV LOUIS BREGUET BP 1 78146 VELIZY VILLACOUBLAY CEDEX FRANCE	1
ATTN R ROGERS DEFENCE RESEARCH AGENCY BLDG 37 TUNNEL SITE CLAPHAM BEDS MK 41 6AE UNITED KINGDOM	1
ATTN S SMITH DEFENCE RESEARCH AGENCY Q134 BUILDING RAE FARNBOROUGH HAMPSHIRE QU14 6TD UNITED KINGDOM	1
ATTN J SOWA SAAB MISSILES AB 581 88 LINKOPING SWEDEN	1
ATTN D SPARROW HUNTING ENGINEERING LTD REDDINGS WOOD AMPTHILL BEDFORDSHIRE MK452HD UNITED KINGDOM	1
ATTN P STUDER DEFENCE TECHNOLOGY AND PROCUREMENT AGENCY SYSTEMS ANALYSIS AND INFORMATION SYSTEMS DIVISION PAPIERMUEHLESTRASSE 25 3003 BERNE SWITZERLAND	1
ATTN DR R G LACAU AEROSPATIALE MISSILE DEPT E/ECN CENTRE DES GATINES 91370 VERRIERE LE BUISSON FRANCE	1
ATTN J M CHARBONNIER VON KARMAN INSTITUTE 72 CHAUSSEE DE WATERLOO 1640 RHODE SAINT GENESE BELGIUM	1
ATTN P CHAMPIGNY DIRECTION DE L AERONAUTIQUE ONERA 29 AV DE LA DIVISION LECLERC 92320 CHATILLON SOUS BAGNEUX CEDEX FRANCE	1
ATTN DR P HENNIG DEUTSCHE AEROSPACE (DASA) VAS 414 ABWEHR AND SCHUTZ POSTFACH 801149 8000 MUENCHEN 80 GERMANY	1
ATTN H G KNOCHE DR GREGORIOU MESSERSCHMIDT BOLKOW BLOHM GMBH UNTERNEHMENSBEREICH APPARATAE MUNCHEN 80 POSTFACH 801149 BAYERN GERMANY	1 1
ATTN DR S J YOON AGENCY FOR DEFENSE DEVELOPMENT AERODYNAMICS DIVISION (4-3-1) P O BOX 35-4 YUSEONG TAEJON KOREA	1
INTERNAL	
B	1
B05 (STATON)	1
B44	1
B44 (HSIEH)	1

DISTRIBUTION (Continued)

	Copies	Copies
B51 (ARMISTEAD)	1	
B60 (TECHNICAL LIBRARY)	3	
C	1	
D	1	
D4	1	
G	1	
G02	1	
G04	5	
G20	1	
G205	1	
G23	1	
G23 (BIBEL)	1	
G23 (CHADWICK)	1	
G23 (COOK)	1	
G23 (GRAFF)	1	
G23 (HANGER)	1	
G23 (HARDY)	1	
G23 (HYMER)	5	
G23 (OHLMEYER)	1	
G23 (ROWLES)	1	
G23 (WEISEL)	1	
G30	1	
G305	1	
G32 (DAY)	1	
G33 (MELTON)	1	
G33 (RINALDI)	1	
G40	1	
G50	1	
G50 (SOLOMON)	1	
G60	1	
G70	1	
G72	1	
G72 (ALEXOPOULOS)	1	
G72 (CHEPREN)	1	
G72 (JONES)	1	
G72 (ROBINSON)	1	
G72 (MCINVILLE)	5	
K	1	
K40	1	
K44 (ICHNIOWSKI)	1	
N	1	
T	1	